



Master's Thesis in Condensed Matter Physics

Preparation and Characterisation of Thin SrCoO_x Films

Patrick Schöffmann

April 2017

written at the
Jülich Centre for Neutron Science
at the Heinz Maier-Leibnitz Zentrum

Dr. habil. J. Wuttke
Dr. S. Pütter

First examiner (supervisor): PD Dr. habil. J. Wuttke
Second examiner: Prof. Dr. F. Klappenberger
Direct supervisor: Dr. S. Pütter

written at:
Jülich Centre for Neutron Science
at the Heinz Maier-Leibnitz Zentrum
Forschungszentrum Jülich GmbH



Table of contents

1	Introduction	5
2	Theory	7
2.1	Crystal structures and properties of different materials	7
2.1.1	SrCoO _x	7
2.1.2	SrTiO ₃	8
2.1.3	MgO	9
2.1.4	Oxides of Co and Sr	10
2.2	Scattering theory	10
2.2.1	General scattering theory	10
2.2.2	Reflectometry	12
2.2.3	Diffraction	15
2.2.4	Rutherford backscattering spectroscopy (RBS)	16
3	Methods and instrumentation	19
3.1	Molecular beam epitaxy set up (MBE)	19
3.2	Auger electron spectroscopy (AES)	20
3.3	Rutherford backscattering spectroscopy (RBS)	20
3.4	Atomic force microscopy (AFM)	21
3.5	Low energy electron diffraction (LEED)	22
3.6	Reflection high-energy electron diffraction (RHEED)	23
3.7	X-ray reflectometry (XRR)	24
3.8	X-ray diffraction (XRD)	25
4	Overview of the sample preparation	27
4.1	Substrate treatment	27
4.2	Setting of Sr and Co deposition rate	28
4.3	Oxygen plasma	29
4.4	Deposition	29
5	Sample Analysis	35
5.1	Stoichiometry	35
5.1.1	Auger electron spectroscopy (AES)	35
5.1.2	Rutherford backscattering spectroscopy (RBS)	36
5.2	X-ray reflectometry (XRR)	41
5.3	Atomic force microscopy (AFM)	42
5.4	Crystallinity	55
5.4.1	Low energy electron diffraction (LEED)	55
5.4.2	Reflection high-energy electron diffraction (RHEED)	61

5.4.3 X-Ray diffraction (XRD)	65
6 Discussion	71
7 Outlook	75
8 Summary	77
Acknowledgements	79
Bibliography	83
List of Figures	86
List of Tables	87
List of Publications	89

Chapter 1

Introduction

Transition metal oxides are an extremely interesting class of materials, exhibiting a wide range of properties, from ferromagnetism to antiferromagnetism, from insulating to conducting, superconductivity [1], multiferroicity [2], and many more.

One special system is strontium cobaltite (SrCoO_x). In its fully oxidized state SrCoO_3 it is a ferromagnetic, conducting perovskite. If, however, the oxygen content is changed slightly to $\text{SrCoO}_{2.5}$, the oxygen vacancies form channels, changing the crystalline structure to a brownmillerite, and the magnetic and conductive properties reverse to an antiferromagnetic insulator. These two crystal structures can be topotactically transformed into one another without destroying the crystallinity [3]. This property makes SrCoO_x suitable for a large variety of applications, e.g. as a cathode material and catalyst for redox reactions in fuel cells [4–6] or magnetic switches via epitaxial strain [7, 8].

To take advantage of the unique possibilities of SrCoO_x , particularly in the field of thin film devices, it is imperative to be able to grow $\text{Sr}_1\text{Co}_1\text{O}_x$ in the correct stoichiometry.

The aim of this thesis is to find the correct deposition conditions for the growth of stoichiometric SrCoO_x thin film samples via molecular beam epitaxy (MBE), like substrate temperature, cooling speed, pressure, oxygen power, and especially the Sr and Co deposition rates. Because the samples are prepared via MBE, which does not use a target with an already defined stoichiometry like sputter deposition or pulsed laser deposition, but rather the evaporation of elemental material, the stoichiometry of the samples depends on several factors. The individual growth rates for Sr and Co do not only depend on the amount of evaporated material, but also on the sticking coefficient of the material on the substrate. As the sticking coefficient is also temperature dependent, there is a large parameter space that needs to be investigated.

Therefore, samples with varying Co/Sr deposition rate ratios at different deposition temperatures were produced. The stoichiometry was analysed by Rutherford backscattering spectroscopy (RBS). The crystallinity of the samples was studied by low energy electron diffraction (LEED), reflection high energy electron diffraction (RHEED) and X-ray diffraction (XRD). To investigate the surface topography,

atomic force microscopy (AFM) was performed. X-ray reflectometry (XRR) was used to determine the global surface roughness and film thickness.

The structure of this thesis is as follows:

In chapter 2 the theoretical background for the crystalline structures and the different scattering methods used for the characterisation of the samples is provided. In chapter 3 the experimental methods and instrumentation, including the MBE system and the analysis methods used in this thesis are discussed. The sample preparation and the deposition conditions are described in chapter 4. In chapter 5 the samples properties, including stoichiometry, crystallinity and surface topography are characterised in detail. The results and the requirements for the stoichiometric samples are discussed in chapter 6. An outlook is provided in chapter 7 and the thesis is summarised in chapter 8.

Chapter 2

Theory

2.1 Crystal structures and properties of different materials

In the following chapter, the crystalline structure of the materials appearing in this thesis will be discussed. Table 2.1 gives an overview of the symmetries and lattice constants.

2.1.1 SrCoO_x

Strontium cobaltite can form two different crystalline structures for a Co/Sr stoichiometry of 1, based on the oxygen content (fig. 2.1). The two structures have vastly different physical properties like magnetism and conductivity.

In the stoichiometry Sr₁Co₁O₃ (P-SrCoO), strontium cobaltite is a ferromagnetic metal with a Curie temperature between 280 K [9] and 305 K [10]. It forms a cubic perovskite structure [11] with a lattice parameter of $a_P = 3.830 \text{ \AA}$ (space group: Pm $\bar{3}$ m). The corner positions of the unit cell are occupied by Co atoms, surrounded by oxygen octahedra, with each octahedron sharing the O-atoms with its neighbours. The Sr atom is in the centre of the unit cell.

If the oxygen content is decreased to Sr₁Co₁O_{2.5} (BM-SrCoO), the oxygen vacancies order along one direction and form vacancy channels [4], creating alternating layers of CoO₄ tetrahedra and of CoO₆ octahedra. The structure is then orthorhombic brownmillerite, with the lattice parameters $a_{BM} = 5.574 \text{ \AA}$, $b_{BM} = 5.470 \text{ \AA}$, and $c_{BM} = 15.745 \text{ \AA}$, which can be written in the pseudo-tetragonal notation as $a_{BM-t} = b_{BM-t} = 3.905 \text{ \AA}$ and $c_{BM-t}/4 = 3.936 \text{ \AA}$ [12], with a 90° angle between the a_{BM-t} and b_{BM-t} vectors, as well between the b vectors. BM-SrCoO is an antiferromagnetic insulator, with a Néel temperature of 570 K [13].

P-SrCoO thin films can be topotactically transformed into BM-SrCoO by annealing in reducing conditions, or, in the reverse, BM-SrCoO can be annealed in oxidising conditions to form P-SrCoO [14]. The topotactic transition implies that

the crystallographic orientation has to stay the same, although material (in this case oxygen) can be lost or gained. The key property that enables this is the small difference in the inter-atomic distance between two Co or Sr atoms in the two structures, i.e. the difference of the cubic and pseudo-tetragonal lattice constants, which have a mismatch of

$$\frac{a_{\text{BM-t}} - a_{\text{P}}}{a_{\text{BM-t}}} = \frac{3.905 \text{ \AA} - 3.829 \text{ \AA}}{3.905 \text{ \AA}} = 1.9\%. \quad (2.1)$$

The structural change between P-SrCoO and BM-SrCoO is accompanied by the change in magnetic and conductive properties. Another way to influence the properties of SrCoO when it is deposited as a thin film on a substrate is epitaxial strain. If the in-plane lattice constants of the film don't match those of the film, the film is strained. If the lattice parameter of the substrate is larger than that of the film tensile strain is found. For tensile strained P-SrCoO, the Curie temperature decreases with increasing strain. There is also a tendency to develop oxygen vacancies in strained films [6, 15].

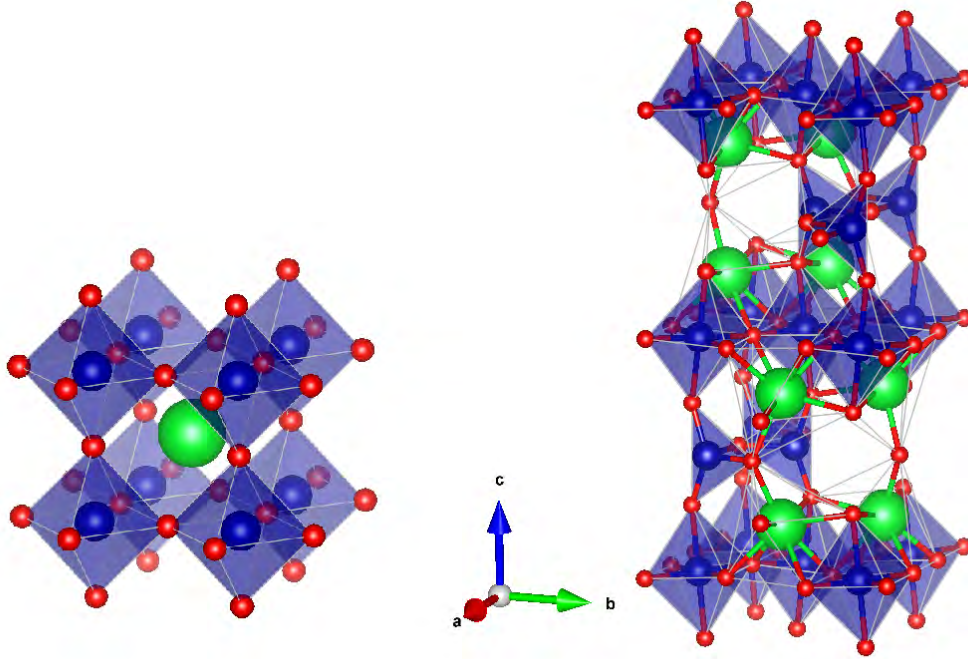


Figure 2.1: Crystalline structure of SrCoO₃ (left) and SrCoO_{2.5} (right). Co is shown in blue, Sr in green, and oxygen in red. The oxygen octahedra and tetrahedra around the Co atoms are shaded in blue. Images generated with VESTA [16].

2.1.2 SrTiO₃

Strontium titanate (SrTiO₃, STO) is used as the substrate material for most samples in this work. For epitaxial thin film growth, the substrate should match

the lattice constant of the deposited material closely, as the substrate provides the in-plane parameter. STO is a cubic perovskite, with the lattice constant of $a_{\text{STO}} = 3.905 \text{ \AA}$ (space group: $\text{Pm}\bar{3}\text{m}$), which is exactly the same as the in-plane lattice parameter of the pseudo-tetragonal BM-SrCoO, with c-axis pointing out-of-plane. This also implies that the lattice mismatch of STO to P-SrCoO is the same as for BM-SrCoO to P-SrCoO, i.e. 1.9% (eq. 2.1). Fig. 2.2 gives an idea for the epitaxial growth of BM-SrCoO on STO.

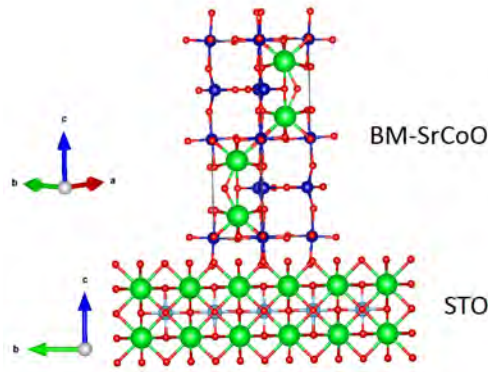


Figure 2.2: Crystalline structure of BM-SrCoO (top) on STO (bottom). Co is shown in dark blue, Ti in light blue, Sr in green, and oxygen in red. The in-plane lattice vectors of BM-SrCoO are rotated by 90° to those of the STO substrate. Image generated with VESTA [16].

Also, because STO is diamagnetic, it doesn't influence the magnetic properties of the film. STO is used for the majority of the samples in this work.

2.1.3 MgO

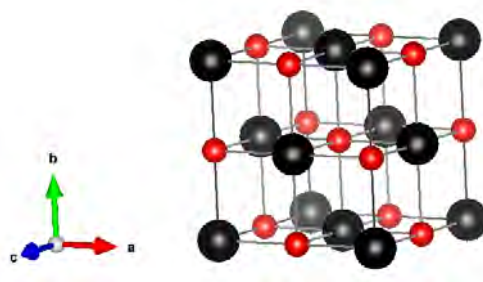


Figure 2.3: Rocksalt structure of MgO. Oxygen is shown in red, Mg in black. CoO and SrO have the same structure. Image generated with VESTA [16].

Magnesium oxide (MgO) was used as an alternate substrate material. It has a cubic rocksalt structure with a lattice constant of $a_{\text{MgO}} = 4.21 \text{ \AA}$ (space group: $\text{Fm}\bar{3}\text{m}$, fig. 2.3), so it matches neither P-SrCoO (mismatch 9.1%) nor BM-SrCoO (mismatch 7.2%). Since MgO contains neither Sr, nor Co it is used to provide

a substrate more suitable for a stoichiometric analysis of the film by Rutherford backscattering spectroscopy (see Chapter 3.3).

2.1.4 Oxides of Co and Sr

In case of Co or Sr excess, CoO, SrO, or SrO₂ may be formed. CoO and SrO exhibit also the rocksalt structure (space group: $Fm\bar{3}m$), like MgO (see fig. 2.3) with lattice constants of 4.26 Å for CoO and 5.16 Å for SrO. In contrast, SrO₂ has a tetragonal structure with lattice constants $a = b = 3.55$ Å and $c = 6.55$ Å (space group: $I4/mmm$).

Table 2.1: Structures and lattice constants of materials appearing in this thesis

Chemical formula	Symmetry	lattice constant
SrCoO ₃	cubic perovskite	3.830 Å
SrCoO _{2.5}	orthorhombic brownmillerite	$a = 5.574$ Å
		$b = 5.470$ Å
		$c = 15.745$ Å
	pseudo-tetragonal notation	$a = b = 3.905$ Å
		$c/4 = 3.936$ Å
SrTiO ₃	cubic perovskite	3.905 Å
MgO	cubic rocksalt	4.210 Å
CoO	cubic rocksalt	4.260 Å
SrO	cubic rocksalt	5.160 Å
SrO ₂	tetragonal	$a = b = 3.550$ Å
		$c = 6.550$ Å

2.2 Scattering theory

In this chapter, the basic principles of scattering are discussed. Scattering methods can be used to determine the crystalline structure and composition of samples. Unless otherwise noted, the wavelength of the probe wave is in the range of the interatomic distance of the sample. This description of scattering theory and scattering methods is based on the JCNS neutron scattering laboratory course lectures [17] and the lecture notes of the 43rd IFF spring school [18] (especially the chapters about general scattering theory [19], reflectometry [20], and diffraction [21]).

2.2.1 General scattering theory

For all methods used here we assume that the scattering process is purely elastic, so the total kinetic energy is conserved. We further assume that the Fraunhofer approximation holds, as the distances between the source and the sample and between the sample and the detector are much larger than the sample. Also, we assume that

the radiation is monochromatic. This lets us describe the wave field incident on the samples as a plane wave with the incidence wave vector \vec{k} and outgoing wave vector \vec{k}'

$$|\vec{k}| = |\vec{k}'| = \frac{2\pi}{\lambda}. \quad (2.2)$$

The magnitude of the scattering vector Q , which describes the direction of the momentum transfer during scattering $\hbar\vec{Q}$, is then

$$|\vec{Q}| = |\vec{k}' - \vec{k}| = \sqrt{k^2 + k'^2 - 2kk'\cos(2\theta)} = \frac{4\pi}{\lambda}\sin\theta. \quad (2.3)$$

It is often used as an alternative to the incidence angle when describing scattering experiments and allows us to directly compare scattering experiments carried out at different wavelengths, and with different probes, e.g. X-rays and neutrons.

To describe the number of particles n scattered into a solid angle $d\Omega$ and an energy interval from E' to $E' + dE$ for a scattering angle 2θ , we define the double differential scattering cross section

$$\frac{d^2\sigma}{d\Omega dE'} = \frac{n}{j d\Omega dE'}, \quad (2.4)$$

with the flux of the incident beam j , for the geometry shown in fig. 2.4.

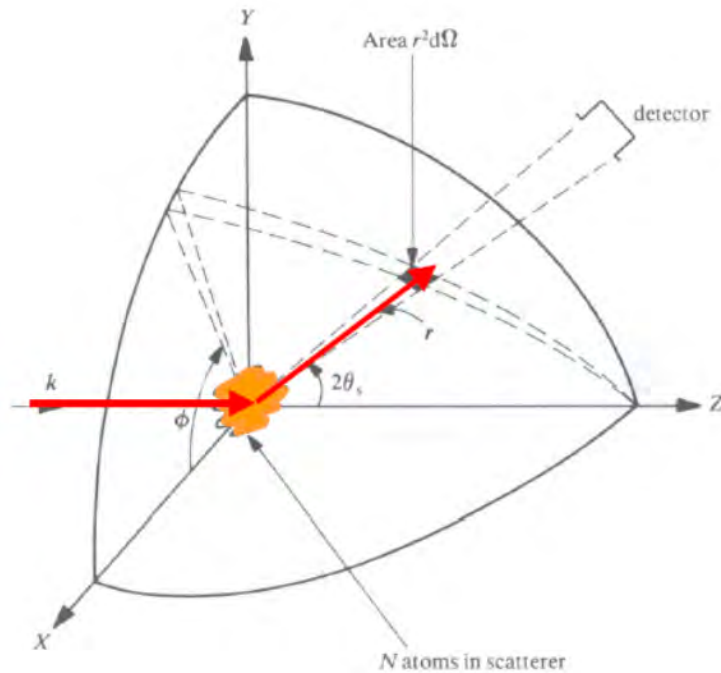


Figure 2.4: Scattering geometry for the differential cross section. Taken from [19].

For a non energy sensitive detector equation 2.4 can be simplified to the differential scattering cross section

$$\frac{d\sigma}{d\Omega}(\theta) = \int_0^\infty \left. \frac{d^2\sigma}{d\Omega dE'} \right|_\theta dE'. \quad (2.5)$$

The total scattering cross section, i.e. for all angles and energy changes, is then

$$\sigma = \int_0^{4\pi} \frac{d\sigma}{d\Omega} d\Omega. \quad (2.6)$$

From the measurement of the scattering cross section, the structure of the sample can be inferred. To do this, one can apply the kinematic scattering approximation, which describes the scattering of a plane wave from a sample by a single event, without refraction at the sample edge. For two waves that are scattered at two different points in the sample (see fig. 2.5), there will be a phase difference, which can be described by

$$\Delta\Phi = 2\pi \cdot \frac{\overline{AB} - \overline{CD}}{\lambda} = \vec{k}' \cdot \vec{r} - \vec{k} \cdot \vec{r} = \vec{Q} \cdot \vec{r}, \quad (2.7)$$

with one wave at a position \vec{r} relative to the other. The individual scattering contributions from all points of the sample can then be integrated to give the total scattering amplitude

$$A(\vec{Q}) \sim A_0 \cdot \int_V \rho_s(\vec{r}) \cdot e^{i\vec{Q} \cdot \vec{r}} d^3x, \quad (2.8)$$

with the scattering density $\rho_s(\vec{r})$, as scattering amplitude at a position \vec{r} .

If the total scattering amplitude were measurable, one could reconstruct the scattering density for all points of the sample and thus gain all information about the sample that is available via scattering. In real experiments however, the total scattering amplitude can not be measured, just the intensity I , so the phase information is lost.

$$I(\vec{Q}) \sim |A(\vec{Q})|^2. \quad (2.9)$$

2.2.2 Reflectometry

Reflectometry is the measurement of the elastic scattering of X-rays (or neutrons) for shallow angles of incidence and is used to analyse the thickness and roughness of films on a substrate. As the incident angle is so low, the scattering information is averaged over the whole sample, and the X-rays are only sensitive to changes in refractive index and not atomic positions.

The incident beam is partly transmitted and specularly reflected from every interface (air-film and film-substrate in the case of thin film samples), based on the

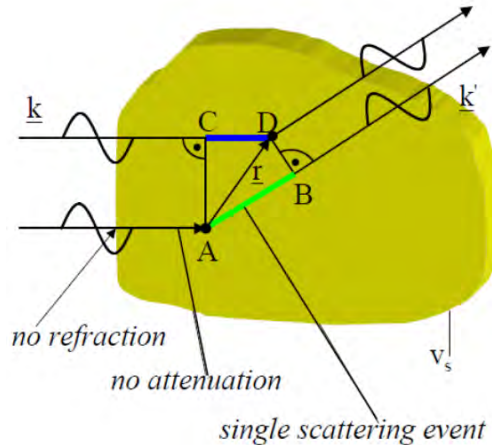


Figure 2.5: Phase difference between two waves, scattered at different point inside a sample. Taken from [19].

refractive index n of the medium. For specular reflection, the angle of incidence α_i and of reflection α_f are the same, and the scattering vector is purely out-of-plane. We define the z -direction to be out-of-plane. The index of refraction is defined by

$$n = \frac{k_1}{k} = 1 - \delta + i\beta, \quad (2.10)$$

with the wave vector k_1 inside the film, the dispersion δ , and the absorption β . It can be calculated by

$$n = 1 - \frac{\lambda^2 r_0}{2\pi} \sum_j \rho_j (Z_j + f'_j + i f''_j) \quad (2.11)$$

$$\delta = \frac{\lambda^2 r_0}{2\pi} \sum_j \rho_j (Z_j + f'_j), \quad (2.12)$$

with the electron radius r_0 , electron density ρ_j , the number of electrons of the atom Z_j , and the correctional factors f'_j for the dispersion and f''_j for the absorption, though they can typically be neglected [18].

From the geometry depicted in fig. 2.6, and the definition for the index of refraction (eq. 2.10), Snell's law can be extracted, taking into account the wave vector component tangential to the surface

$$\frac{\cos \theta_0}{\cos \theta_1} = \frac{k_1}{k_0} = n_1. \quad (2.13)$$

For small angles of incidence, below the critical angle θ_C , there is no transmitted beam. This is a consequence of the index of refraction being smaller than 1 for X-rays. The critical angle is dependent on the dispersion δ , and can be calculated with

$$n = \cos \theta_C \quad (2.14)$$

$$\theta_C \approx \sqrt{2\delta}. \quad (2.15)$$

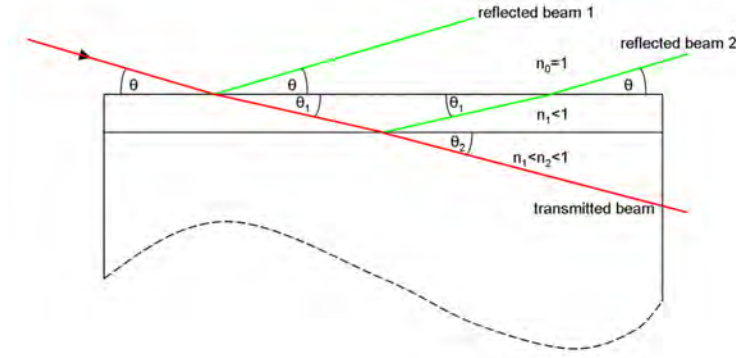


Figure 2.6: Transmission and specular reflection from a film and a substrate.
Taken from [20].

Because of the already discussed phase difference between two waves scattered at different points, the two reflected waves interfere with each other and form alternating interference maxima and minima, so called Kiessig fringes. A maximum occurs if the difference in path length of the two interfering waves is an integer multiple x of the wavelength. This is described by the Bragg condition for scattering in a medium

$$2d \cdot n_1 \sin \theta_1 = x\lambda. \quad (2.16)$$

The difference in scattering angle between two maxima can be used to calculate the film thickness d . With equation 2.10 (while neglecting the absorption term) and 2.13, we can write

$$n_1 \sin \theta_1 = \sqrt{n_1^2 - n_1^2 \cos^2 \theta_1} \quad (2.17)$$

$$= \sqrt{(1 - \delta)^2 (1 - \cos^2 \theta)}. \quad (2.18)$$

This can be simplified by a series expansion of $\cos^2 \theta$ to

$$n_1 \sin \theta_1 = \sqrt{\theta^2 - 2\delta}, \quad (2.19)$$

when neglecting terms of higher order. With the equation for the critical angle 2.15, this gives us the equation for the total layer thickness

$$2d\sqrt{\theta^2 - \theta_C^2} = x\lambda. \quad (2.20)$$

Another property of the sample that can be extracted from reflectivity measurements is the roughness. In general the roughness is the deviation of the local height of the films surface from a mean value. In the reflectivity measurement, the roughness is

$$r_{j,j+1}^{\text{rough}} = r_{j,j+1}^{\text{flat}} \cdot e^{-2\sigma^2 k_{z,j} k_{z,j+1}}, \quad (2.21)$$

with the out-of-plane wave vectors k_z , and the Fresnel coefficients $r_{j,j+1}$ [22]. It is effectively a damping of the reflectivity for a rough surface, because not the whole surface fulfils the Bragg condition.

2.2.3 Diffraction

In contrast to reflectometry, which is sensitive only to the change of the index of refraction, diffraction probes the position of atoms in the sample, and can thus be used to determine the lattice constants if the sample is crystalline.

Because the scattering process is best described in reciprocal space, we define the reciprocal lattice vector $\vec{\tau}_i$ as

$$\vec{\tau}_i = \frac{2\pi(\vec{a}_j \times \vec{a}_k)}{\vec{a}_1 \cdot (\vec{a}_2 \times \vec{a}_3)} = \frac{(\vec{a}_j \times \vec{a}_k)}{V_c}, \quad (2.22)$$

with the real space lattice vectors \vec{a}_i , and the real space unit cell volume V_c . The reciprocal lattice vectors satisfy the conditions

$$\vec{\tau}_i \cdot \vec{a}_i = 1 \quad (2.23)$$

$$\vec{\tau}_i \cdot \vec{a}_j = 0, \text{ for } i \neq j. \quad (2.24)$$

Because the reciprocal lattice is the Fourier transformation of the crystal lattice, each reciprocal lattice point represents a set of planes in real space d_{hkl} . These planes are described by their intercept of the real space lattice axes X, Y, Z, at the points a/h , b/k , and c/l . The equation for the lattice plains (hkl) is then

$$\frac{hx}{a} + \frac{ky}{b} + \frac{lz}{c} = n \quad (2.25)$$

with the integer n , and the so called Miller indices h, k , and l .

The equation for the inter-planar spacing in the orthorhombic symmetry is

$$d(hkl) = \left(\frac{h^2}{a^2} + \frac{k^2}{b^2} + \frac{l^2}{c^2} \right)^{-\frac{1}{2}}, \quad (2.26)$$

which can be simplified for the cubic symmetry to

$$d(hkl) = a \cdot (h^2 + k^2 + l^2)^{-\frac{1}{2}}. \quad (2.27)$$

The length of the reciprocal lattice vectors is proportional to the inter-planar spacing with

$$|\vec{\tau}| = \frac{2\pi}{d_{hkl}}. \quad (2.28)$$

The reciprocal lattice can be used to construct the Ewald sphere, the geometric representation of the scattering condition (see fig. 2.7). The incident wave vector \vec{k} points towards the origin of the reciprocal lattice. A sphere with radius $|\vec{k}|$ around the the origin of \vec{k} is drawn, intersecting the diffracted beam. If a reciprocal lattice point is on this intersection, the scattering condition is fulfilled, and a Bragg peak can be observed. From this construction the Bragg condition can also be verified,

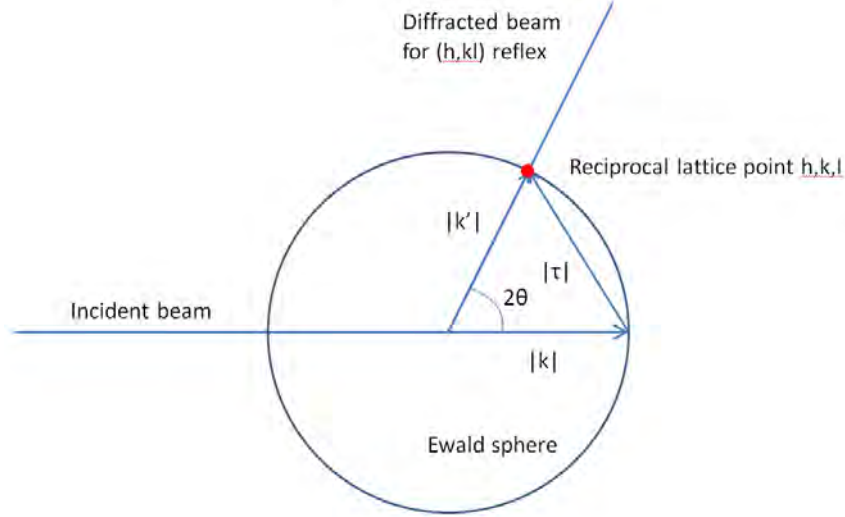


Figure 2.7: Ewald construction for the scattering condition in reciprocal space

since from geometry

$$2|\vec{k}| \cdot \sin(\theta) = |\vec{\tau}| \quad (2.29)$$

so with $k = \frac{2\pi}{\lambda}$ and $\tau = \frac{2\pi}{d_{hkl}}$ the Bragg equation follows

$$2d_{hkl} \cdot \sin(\theta_{hkl}) = \lambda \quad (2.30)$$

$$\Rightarrow d_{hkl} = \frac{\lambda}{2 \sin(\theta_{hkl})}. \quad (2.31)$$

Since we can measure the angles at which a Bragg peak is observed, the Bragg condition can be used to determine the inter-planar spacing d_{hkl} , for a known wavelength.

2.2.4 Rutherford backscattering spectroscopy (RBS)

Rutherford backscattering spectroscopy can be used to determine the stoichiometry of samples by He⁻ (or less often H⁻) ion backscattering [23].

As the interaction energy of the ions with the target nucleus is much larger than the atomic binding energy, but low enough not to initiate nuclear reactions or resonances, they can be modelled by elastic scattering. In this case energy and momentum (parallel and perpendicular) must be preserved, so

$$\frac{1}{2}M_P v_{P_i}^2 = \frac{1}{2}M_P v_{P_f}^2 + \frac{1}{2}M_T v_{T_f}^2 \quad (2.32)$$

$$M_P v_{P_i} = M_P v_{P_f} \cos\theta + M_T v_{T_f} \cos\phi \quad (2.33)$$

$$0 = M_P v_{P_f} \sin\theta - M_T v_{T_f} \sin\phi \quad (2.34)$$

with the particle mass M_P , the target mass M_T , the particle velocity before scattering v_{P_i} , the particle velocity after scattering v_{P_f} , the target velocity after

scattering v_{T_f} , the angle θ the particle is scattered at relative to its trajectory before the scattering, and the angle ϕ the target is scattered at relative to the direction of the particle before the scattering, must hold.

The energy ratio for the particle after and before the scattering is defined as the kinematic factor

$$K = \frac{E_{P_f}}{E_{P_i}} = \left(\frac{\sqrt{M_T^2 - M_P^2 \sin^2 \theta} + M_P \cos \theta}{M_T + M_P} \right)^2. \quad (2.35)$$

Because of the $\cos^2 \theta$ dependence the largest energy difference, i.e. smallest value for K , and, as a consequence, the highest resolution, occurs at a scattering angle of 180° .

$$K(180^\circ) = \left(\frac{M_T - M_P}{M_T + M_P} \right)^2 = K(90^\circ)^2 \quad (2.36)$$

As it is not possible to place a detector at the same angle as the particle beam, it is typically situated at an angle of 170° .

The differential scattering cross section for ions

$$\frac{d\sigma}{d\Omega} \propto \left(\frac{Z_T Z_P e^2}{4E} \right)^2, \quad (2.37)$$

is proportional to Z_T^2 , so backscattering is intrinsically more sensitive to heavy elements. It is also proportional to Z_P^2 , so heavier ions result in a higher number of scattering events, and because of eq. 2.35 also a better energy resolution. As the ion's mass has to be smaller than the target atom's mass for backscattering to occur, the use of He-ions is most common in RBS.

Chapter 3

Methods and instrumentation

3.1 Molecular beam epitaxy set up (MBE)

The DCA M600 molecular beam epitaxy (MBE) set up of the Jülich Centre for Neutron Science (JCNS) at the Heinz Maier-Leibnitz Zentrum (MLZ) was used to prepare all samples. It consists of three vacuum chambers connected by gate valves. Samples are introduced or extracted via the load lock, which can be pumped to a pressure of $2 \cdot 10^{-8}$ Torr. Adjacent to the load lock is the buffer line, which houses the low energy electron diffraction (LEED) and the Auger electron spectroscopy (AES) set ups and reaches pressures as low as $2 \cdot 10^{-10}$ Torr. The sample holders rest on trolleys and can be picked up by the manipulators at different positions for measurements or the transfer manipulator.

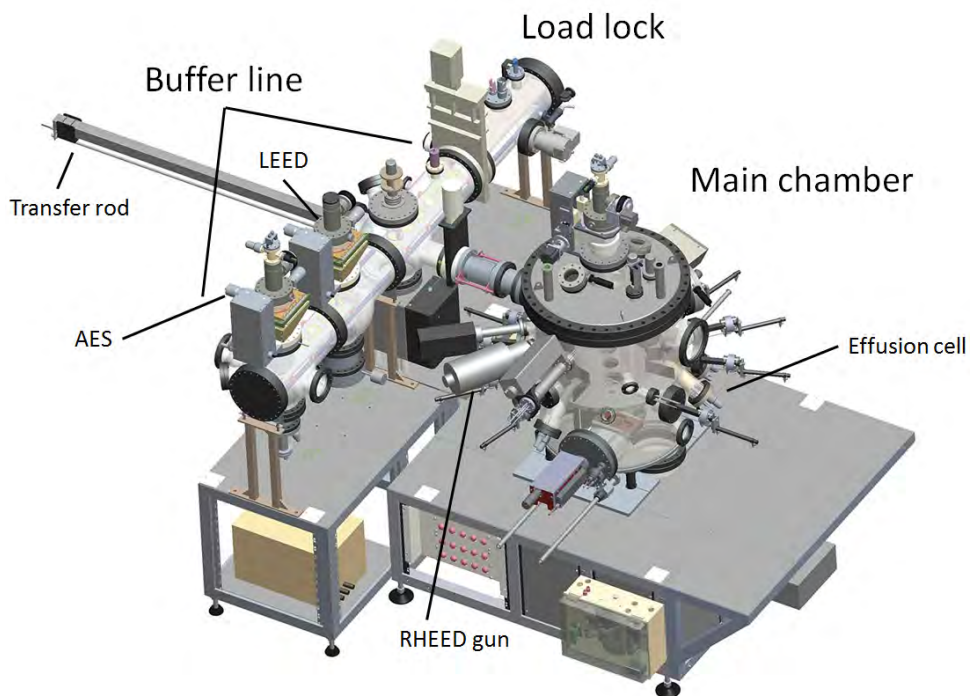


Figure 3.1: Schematic of the DCA M600 molecular beam epitaxy setup. Modified from [24].

A transfer rod is used to transport the samples into the main chamber, connected to the buffer line, where it is picked up by the manipulator. The main chamber is equipped with a residual gas analyser, a reflection high-energy electron diffraction (RHEED) set up, as well as an oxygen plasma source. Around the outside wall of the chamber two e-guns and six effusion cells are arranged, pointing towards the sample position for deposition. The effusion cells bear one elemental material in a crucible. During deposition, the cells are kept at a constant pre-defined temperature and release a molecular beam of their respective element onto the sample. Each cell is equipped with a shutter to start and stop the deposition. The base pressure of the main chamber is $1 \cdot 10^{-10}$ Torr, which rises to $2 \cdot 10^{-5}$ Torr when the plasma source is activated for the deposition of oxides. To set the amount of deposited material, the output of the cells is calibrated individually with a quartz crystal microbalance (QCM). The QCM oscillates at its resonance frequency, which decreases with increasing deposition rate. The temperature of the cells is adjusted according to the targeted frequency change. Because it takes some time for the cells as well as the QCM to reach thermal equilibrium after a change in temperature, the frequency change is observed for at least 30 min after the chosen value is reached.

3.2 Auger electron spectroscopy (AES)

Auger electron spectroscopy (AES) is a surface characterisation technique, used to determine the elemental composition of the first few atomic layers of a sample.

Electrons with an energy of 3 keV are directed onto the sample and scatter from a core electron, transferring enough energy in the process for the core electron to leave the atom. To fill the now empty core shell, a second electron jumps to the lower empty level, either releasing the energy difference as a photon, or — in the case of the Auger process — exciting a third, outer shell electron, which leaves the atom as well. Since the energy transferred to the third electron is characteristic for each element, the spectrometer registers the derivative of the number of these electrons per energy interval ($\frac{dN}{dE}$), thus enabling the identification of the individual elements. As electrons have a very low penetration depth, only the first few atomic layers can be investigated.

3.3 Rutherford backscattering spectroscopy (RBS)

Rutherford backscattering spectroscopy (RBS) is a method to determine the elemental composition of a sample by He-ion backscattering. (Theoretical aspects have been discussed in chapter 2.2.4.)

He-ions are accelerated by a tandem-accelerator to an energy of 1.7 MeV towards the sample and scatter elastically, losing energy in the process depending on the mass of the atom they are scattering from. By measuring the energy and amount

of the He-ions after the scattering, a characteristic spectrum is obtained. RBS is intrinsically more sensitive to higher mass atoms with a quadratic dependence of the differential scattering cross section to the target atoms mass, so the oxygen content of a sample can not be reliably determined by RBS.

The RBS measurements in this thesis were performed by Dr. Jürgen Schubert and Willi Zander (Peter Grünberg Institut (PGI-9), Forschungszentrum Jülich), and by Dr. René Heller (Institute of Ion Beam Physics and Materials Research, Helmholtz-Zentrum Dresden-Rossendorf).

3.4 Atomic force microscopy (AFM)

Atomic force microscopy was used to determine the surface topography and local roughness of the samples.

AFM is a scanning probe technique, which images a sample topography by moving a tip at the end of a cantilever over the sample surface. The tip interacts with the sample by attractive or repulsive forces. There are different sources of these interaction forces, like magnetic, electrostatic, chemical, capillary, van-der-Waals, and Pauli interactions. The dominant interactions for measuring AFM are the Van-der-Waals attraction and Pauli repulsion, which can be modelled by the Lennard-Jones potential (fig. 3.2) [25].

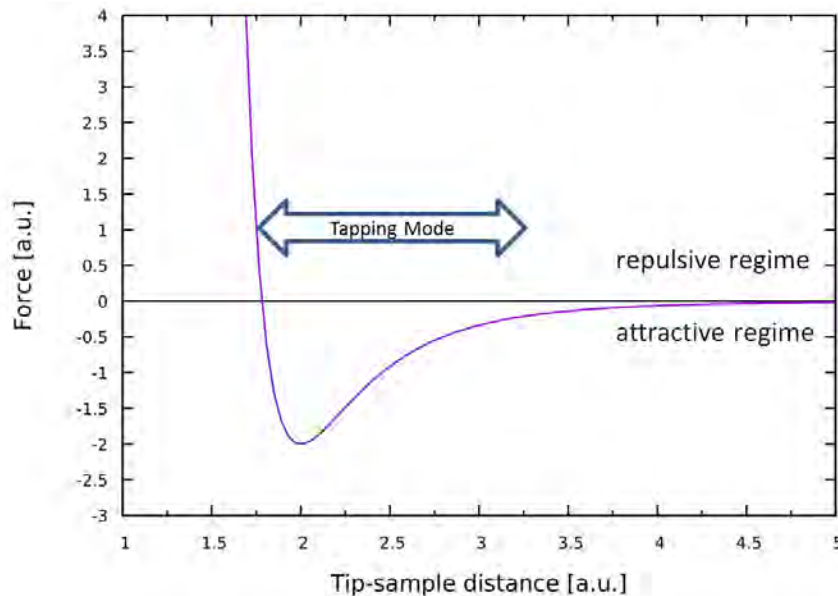


Figure 3.2: Lennard-Jones potential.

Because the tip is non-magnetic (i.e. not ferromagnetic), and there is no sample bias voltage applied in the measurements performed here, the magnetic and electrostatic interactions are not present or negligible. The range of chemical interactions is very short. As all measurements were performed in tapping mode (also called

intermittent contact mode), and the tip is only in contact with the sample for a very short moment, chemical interactions can be neglected.

In tapping mode the cantilever is driven at a constant frequency close to, but lower than, its resonance frequency. The tip-sample interaction changes the amplitude of the oscillation. A feedback loop minimizes the amplitude change by adjusting the tip-sample distance, which is recorded, providing topographic data. The cantilever oscillation and interaction with the sample are measured by a detector which collects the laser beam which was reflected from the cantilever.

From the topography scans, the roughness of the sample can be extracted. It is given here as the root-mean-square roughness σ_{RMS}

$$\sigma_{\text{RMS}} = \sqrt{\frac{1}{N} \sum_{n=0}^N (z_i - z_o)^2}, \quad (3.1)$$

with the mean height z_o , and the local height z_i at the position i .

The instrument used in this thesis is an Agilent Technologies 5500 SPM. Typically the HQ:NSC15/Al BS cantilevers from MikroMasch were used, which have a spring constant of 40 N/m and a resonance frequency around 325 kHz. The data were evaluated with the program Gwyddion [26].

3.5 Low energy electron diffraction (LEED)

LEED is used as a tool to determine the crystallinity and the lattice parameters of a sample. Electrons with an energy between 50 eV and 300 eV are shot on the sample and are scattered back on a fluorescent screen. If the sample has a crystalline structure, distinct Bragg spots will appear. By measuring the distance between the Bragg spots, one can calculate the in-plane lattice parameter of the sample.

In fig.3.3 the LEED geometry is shown. The angle of incidence of the electron beam is perpendicular to the sample surface (wave vector k) and the electrons get scattered back towards the fluorescent screen (wavevector k') under an angle α . Because the electrons penetrate only the first few atomic layers of the film, the scattering contains practically no depth information and can be seen as scattering from a 2D structure. The scattering condition is then

$$k'_{\parallel} - k_{\parallel} = \vec{\tau} \quad (3.2)$$

with the reciprocal lattice vector $\vec{\tau}$. Since the scattering is considered purely elastic, the relation $|\vec{k}| = |\vec{k}'|$ holds.

The intercept theorem can then be used to relate the k-space to the experimental geometry by

$$\frac{|\vec{\tau}|}{|\vec{k}|} = \frac{d}{R} \quad (3.3)$$

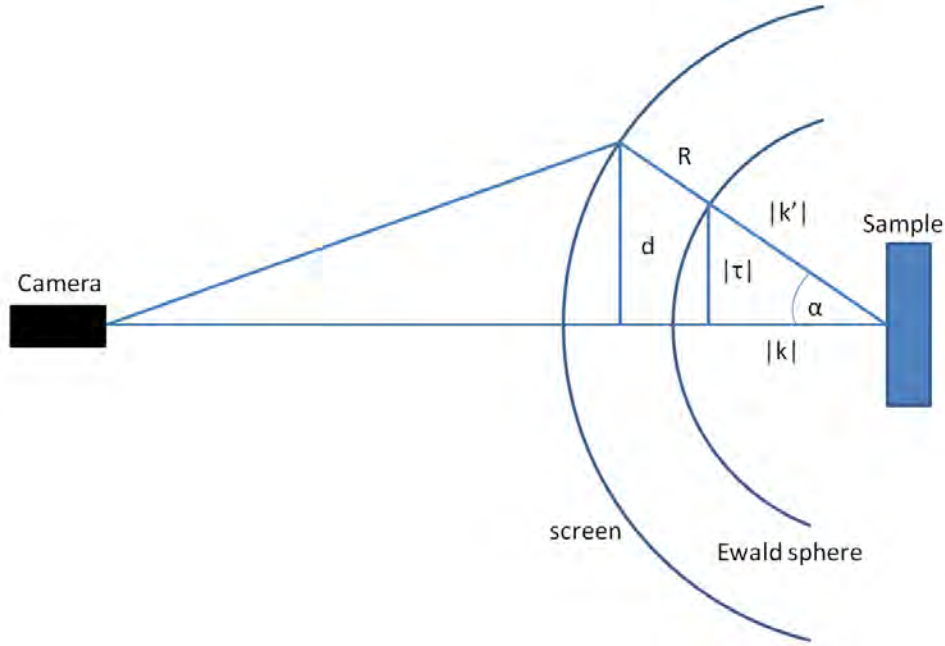


Figure 3.3: LEED geometry with Ewald sphere.

with the screen radius R , and the distance between Bragg spots on the screen d .

The incident wavevector, and thus radius of the Ewald-sphere, is calculated utilizing the acceleration voltage U , the electron mass m_e , the electron charge e , and Plancks constant h , to be

$$E = eU = \frac{\hbar^2 k'^2}{2m_e} \quad (3.4)$$

$$|\vec{k}| = \frac{\sqrt{2m_e eU}}{\hbar}. \quad (3.5)$$

Because the scattering vector is related to the lattice constant a by $|\vec{\tau}| = \frac{2\pi}{a}$, equations 3.3 and 3.5 can be used to calculate the lattice constant by

$$\frac{1}{d} = \frac{a\sqrt{2m_e e}}{hR} \sqrt{U}. \quad (3.6)$$

3.6 Reflection high-energy electron diffraction (RHEED)

RHEED is used to monitor the crystallinity of the film during growth. Similar to LEED, the electrons have a very low penetration depth and thus only carry information about the in-plane lattice structure. This holds even though the electron energy is much higher with 15 keV compared to 50 eV - 300 eV in LEED, since the

scattering angle is very shallow with respect to the sample plane. As the scattering can be considered as scattering from a 2D structure, the reciprocal lattice points are extended into rods (see fig. 3.4). This is because the out-of-plane component of the scattering vector is approximately zero and thus the influence on the Bragg condition is negligible.

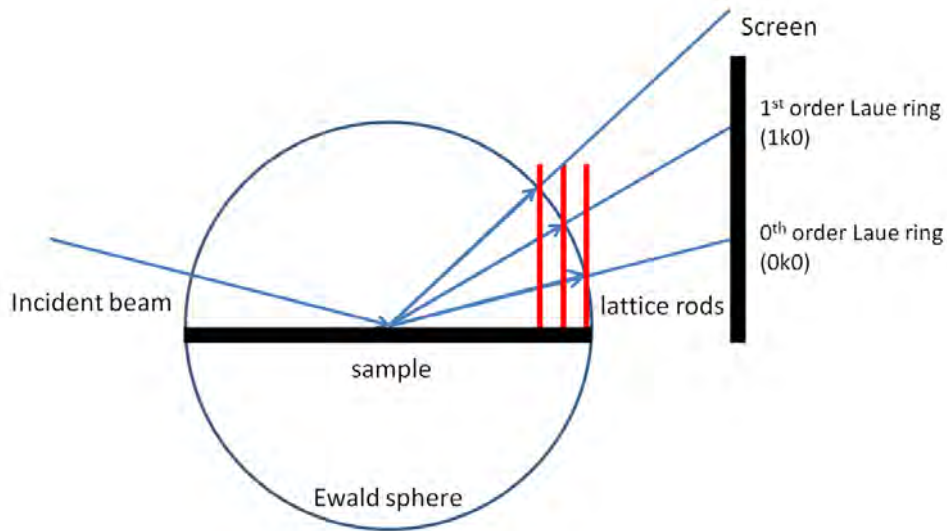


Figure 3.4: Ewald construction for RHEED geometry.

Since the Bragg reflexes are observed on a flat screen intersecting the Ewald sphere, they form circles, so called Laue rings, if one reciprocal lattice vector is parallel to the beam direction. The Laue rings can be enumerated based on the parallel component of the wave vector (h), with the zero'th order Laue ring ($0k0$) at the lowest angle. Commonly the zero'th and first order Laue rings can be observed on the screen. If the crystallinity of the samples is good, the Bragg peaks are sharp. For a rough surface the Bragg peaks are elongated, since the sample does not present a single flat plane for the electron beam, but rather many slightly differently aligned planes, which fulfil the scattering condition at slightly different angles. Another contribution to the RHEED pattern are the Kikuchi lines, which are a result of inelastic scattering. Electrons are first scattered inelastically and then rescattered elastically, forming the Kikuchi lines. They are only observable for a very good crystallinity and a very flat surface.

3.7 X-ray reflectometry (XRR)

X-ray reflectometry is a common method to measure the thickness and roughness of thin films.

An X-ray beam is scattered from the sample at a low angle ($0^\circ - 4^\circ$) and the specular reflex is measured. The reflected beam is a superposition of the thin film and the substrate contribution. The two contributions give rise to an interference

pattern with Kiessig fringes which was already discussed in chapter 2.2.2. From the distance between two Kiessig fringes, the film thickness can be determined, while the slope of the signal can be used to calculate the roughness.

The instrument used here is the Bruker D8 of the neutron optics group of the Heinz Maier-Leibnitz Zentrum, which uses a Cu-K $_{\alpha}$ source without monochromator.

3.8 X-ray diffraction (XRD)

As both LEED and RHEED are only sensitive to a few atomic layers of the film, and only provide information about the in-plane lattice structure, XRD was used to probe the crystallinity of the whole sample.

The set-up for XRD is nearly the same as for XRR, but since XRD is measured at much higher angles (beginning at 10° for a Cu-K $_{\alpha}$ source), the X-rays are no longer sensitive only to changes in the refractive index, but also to the crystal structure.

The measurements were performed with the PANalytical Empyrean diffractometer at the Material Science Lab of the Helmholtz-Zentrum Geestacht (HZG) at MLZ in collaboration with Armin Kriele and with a Bruker D8 diffractometer at the Forschungszentrum Jülich by Dr. Paul Zakalek and Markus Waschke.

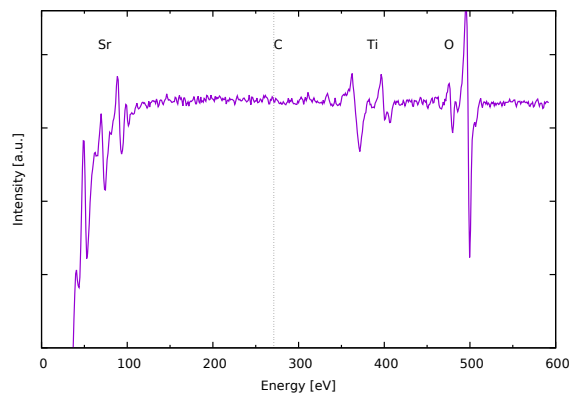
Chapter 4

Overview of the sample preparation

In order to grow high quality thin films by molecular beam epitaxy, there are several requirements that have to be met. First, the substrate has to be treated to remove any contaminations. Next, the temperature of the effusion cells has to be adjusted until the correct deposition rate is reached and has proven to be stable. Then, the oxygen plasma has to be ignited. After these conditions are fulfilled, the substrate can be heated to the deposition temperature and the film can be prepared.

4.1 Substrate treatment

a) SrTiO₃ substrate



b) MgO substrate

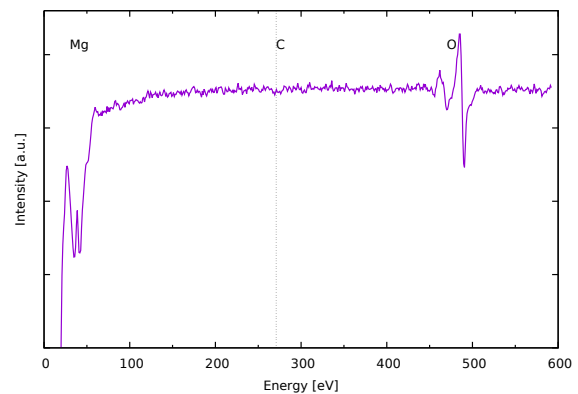


Figure 4.1: Auger electron spectrum of an STO (a) and MgO (b) substrate after annealing at 1000 °C for two hours; The Sr, Ti, and O peaks for STO and Mg and O peaks for MgO are clearly visible. There are no traces of carbon, indicating a clean substrate surface.

In order to ensure a clean sample surface without contamination in ambient air all substrates are annealed at 1000 °C for 2h in ultra-high vacuum (UHV). To verify that this procedure removed any contamination, Auger electron spectroscopy (AES)

was performed. The AES spectrum on an annealed STO substrate reveals only Sr, Ti and O peaks and no C peak, indicating a surface free of organic contamination (Fig. 4.1 a). Similar results were reached for MgO substrates (Fig. 4.1 b).

4.2 Setting of Sr and Co deposition rate

As described in chapter 3.1, the MBE is equipped with a quartz crystal microbalance to measure the amount of material evaporated from the effusion cells. The QCM oscillates at its resonance frequency, which decreases when material is deposited on the QCM. Because the frequency change of the QCM is proportional to the deposition rate, it can be used to measure the evaporation rate of a material [27]. The QCM frequency change is measured for each element individually and the cell's temperature is adjusted (Fig. 4.2). After changing the temperature of the effusion cells, and thereby the deposition rate, it takes a couple of minutes for the QCM frequency change to follow the temperature change, so the adjustment has to be done step-by-step and can be rather time consuming. As the wanted frequency change is reached, it is observed for at least 30 min to confirm its stability. The frequency change was assumed to be stable, if it did not deviate by more than $0.001 \frac{\text{Hz}}{\text{s}}$ from the desired value. This process may take a few hours per element, even if the cells have approximately been at the deposition temperature. The correct temperature for a given deposition rate is also dependent on the amount of material inside the effusion cell, so it has to be adjusted for each sample deposition. Fig. 4.2 a shows the setting of the frequency change for Co, with the temperature shown in yellow, while fig. 4.2 b shows the setting up of Sr. After the last temperature adjustment the Sr frequency change stabilized in about 45 min, while the Co one took about 85 min.

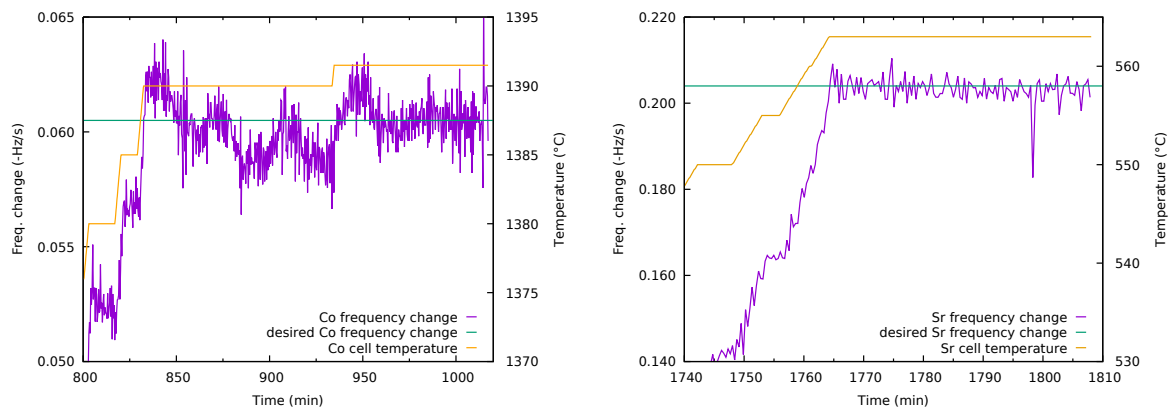


Figure 4.2: QCM frequency changes for Co (left) and Sr (right). The temperature (orange) was adjusted until the frequency change (purple) stabilized at the desired frequency change (green), $-0.061 \frac{\text{Hz}}{\text{s}}$ for Co and $-0.204 \frac{\text{Hz}}{\text{s}}$ for Sr.

4.3 Oxygen plasma

After both Sr and Co frequency changes are set, an oxygen plasma is produced with an oxygen plasma source to provide atomic oxygen. When the total pressure is above $7 \cdot 10^{-6}$ Torr, the plasma is ignited. Usually, the plasma strikes in the low brightness mode, in which the energy is concentrated on a low amount of oxygen atoms, leading to fewer unbound oxygen atoms than in the high brightness mode (HBM), which has a high amount of atomic oxygen. The HBM is the optimal mode for thin film growth, so the plasma source is adjusted to provide a stable HBM. All samples were prepared with an oxygen flow of $0.12 \frac{\text{cm}^3}{\text{min}}$ (sccm), a plasma power of 300 W, and a reflected power of 0 W. The total pressure in the chamber during deposition was between $8.5 \cdot 10^{-6}$ Torr and $1.2 \cdot 10^{-5}$ Torr for all samples, at an oxygen content of typically 95% measured by the residual gas analyser.

4.4 Deposition

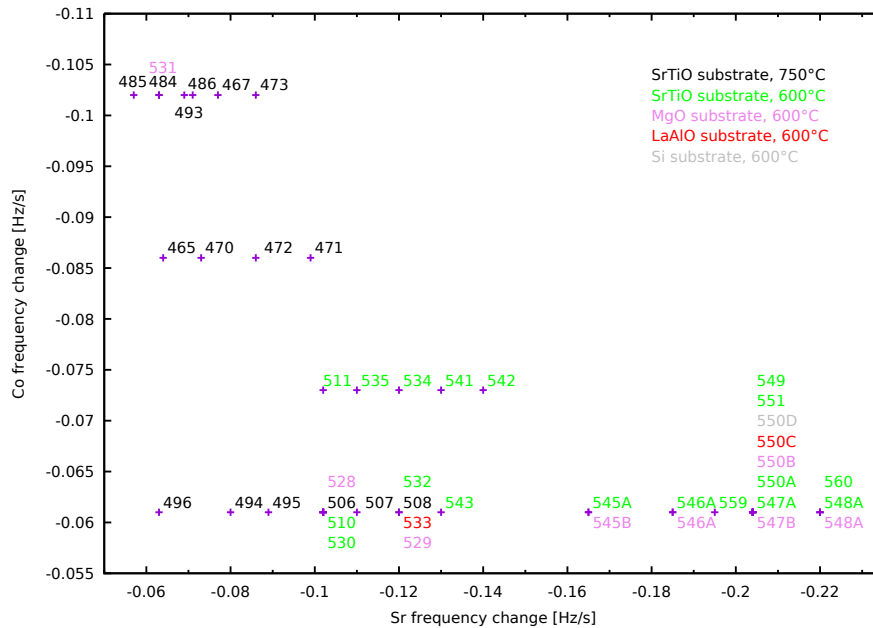


Figure 4.3: Overview of the used Sr and Co frequency changes for all samples, as measured by the quartz crystal microbalance.

When the deposition rates of Sr and Co (i.e. the frequency changes) and the oxygen plasma are stable, the substrate is heated up to the deposition temperature, either 750 °C for samples 465 - 508 and 531, or 600 °C for samples 510 - 560 (see Table 4.1), and kept at constant temperature for about 10 min to ensure that the whole sample is in an equilibrium before starting the deposition. In general, the samples were prepared in single-sample holders, with the substrate in the focal point of the effusion cells and the plasma source. In order to grow films on different substrates at the same time, sample pairs were produced in double holders (samples 545A-548B), with the MgO substrate in the focal point and the STO substrate next to it.

One sample quartet was prepared in a 4-sample holder (samples 550A-D), with each substrate in equivalent positions around the focal point. These samples are identified by a suffix 'A' for STO, 'B' for MgO, 'C' for LaAlO, and 'D' for Si. During the deposition of sample pairs or quartets, the sample holder was rotated with 2 RPM to ensure the same growth conditions for all substrates.

Table 4.1 and figure 4.3 give an overview over the different samples. They were prepared at one of four Co rates (frequency change), while systematically varying the Sr rate (frequency change) to optimize the stoichiometry. In table 4.2 the results for RBS, XRR, and AFM are listed (following chapter). The reason is to enable an easier comparison between deposition parameters and measurements.

Table 4.1: Overview of sample preparation parameter

Sample	Substrate	Substrate temperature [° C]	cooling rate [$\frac{^{\circ}\text{C}}{\text{min}}$]	Growth time [min]	Co frequency change [Hz/s]	Sr frequency change [Hz/s]	Co/Sr frequency ratio
465	STO	750	20	60	-0.086	-0.064	1.34
467	STO	750	20	60	-0.102	-0.077	1.32
470	STO	750	20	60	-0.086	-0.073	1.18
471	STO	750	20	60	-0.086	-0.099	0.87
472	STO	750	20	60	-0.086	-0.086	1
473	STO	750	20	60	-0.102	-0.086	1.19
484	STO	750	20	60	-0.102	-0.063	1.62
485	STO	750	20	60	-0.102	-0.057	1.79
486	STO	750	20	60	-0.102	-0.071	1.44
493	STO	750	20	60	-0.102	-0.069	1.48
494	STO	750	20	120	-0.061	-0.080	0.76
495	STO	750	20	120	-0.061	-0.089	0.69
496	STO	750	20	120	-0.061	-0.063	0.97
506	STO	750	20	120	-0.061	-0.102	0.60
507	STO	750	20	120	-0.061	-0.110	0.55
508	STO	750	20	120	-0.061	-0.120	0.51
510	STO	600	50	120	-0.061	-0.102	0.60
511	STO	600	50	120	-0.073	-0.102	0.72
528	MgO	600	50	120	-0.061	-0.102	0.60
529	MgO	600	50	120	-0.061	-0.120	0.51
530	STO	600	50	120	-0.061	-0.102	0.60
531	MgO	750	20	60	-0.102	-0.063	1.62
532	STO	600	50	120	-0.061	-0.102	0.60
533	LAO	600	50	120	-0.061	-0.102	0.60
534	STO	600	50	120	-0.073	-0.120	0.61
535	STO	600	50	120	-0.073	-0.110	0.66
541	STO	600	50	120	-0.073	-0.130	0.56
542	STO	600	50	120	-0.073	-0.140	0.52
543	STO	600	50	120	-0.061	-0.130	0.47
545-A ^a	STO	600	50	120	-0.061	-0.165	0.37
545-B ^a	MgO	600	50	120	-0.061	-0.165	0.37
546-A ^a	STO	600	50	120	-0.061	-0.185	0.33
546-B ^a	MgO	600	50	120	-0.061	-0.185	0.33
547-A ^a	STO	600	50	120	-0.061	-0.204	0.30
547-B ^a	MgO	600	50	120	-0.061	-0.204	0.30
548-A ^a	STO	600	50	120	-0.061	-0.220	0.28
548-B ^a	MgO	600	50	120	-0.061	-0.220	0.28
549	STO	600	50	120	-0.061	-0.204	0.30
550-A ^a	STO	600	50	120	-0.061	-0.204	0.30
550-B ^a	MgO	600	50	120	-0.061	-0.204	0.30
550-C ^a	LAO	600	50	120	-0.061	-0.204	0.30
550-D ^a	Si	600	50	120	-0.061	-0.204	0.30
551	STO	600	50	120	-0.061	-0.204	0.30
559	STO	600	50	120	-0.061	-0.195	0.31
560	STO	600	50	120	-0.061	-0.220	0.28

a) samples with index A and B (A-D for sample 550) were produced simultaneously in one sample holder. The holder rotated with 2 RPM to have the same conditions for both substrates.

Table 4.2: Overview of RBS, XRR, and AFM measurements

Sample	Co Δ freq. [Hz/s]	Sr Δ freq. [Hz/s]	Co/Sr freq. ratio	RBS Co/Sr ratio	Thickness [Å]	XRR roughness [Å]	AFM roughness [Å]
465	-0.086	-0.064	1.34	2.93	150	23	43
467	-0.102	-0.077	1.32	3.7	167	30	25
470	-0.086	-0.073	1.18	2.75	159	29	26
471	-0.086	-0.099	0.87	1.97	215	23	30
472	-0.086	-0.086	1.00	2.08	233	42	51
473	-0.102	-0.086	1.19	2.18	204	40	51
484	-0.102	-0.063	1.62	5	162	15	10
485	-0.102	-0.057	1.79	10	145	10	10
486	-0.102	-0.071	1.44	4.25	217	33	37
493	-0.102	-0.069	1.48	4.29	227	20	47
494	-0.061	-0.080	0.76	2.63	200	50	71
495	-0.061	-0.089	0.69	2.14	300	40	67
496	-0.061	-0.063	0.97	3	210	45	69
506	-0.061	-0.102	0.60	-	326	54	64
507	-0.061	-0.110	0.55	-	310	45	51
508	-0.061	-0.120	0.51	-	338	40	24
510	-0.061	-0.102	0.60	1.53	263	20	23
511	-0.073	-0.102	0.72	2.45	280	30	26
528	-0.061	-0.102	0.60	1.45	230	20	17
529	-0.061	-0.120	0.51	1.55	315	20	19
530	-0.061	-0.102	0.60	1.22	243	12	18
531	-0.102	-0.063	1.62	7.6	150	10	19
532	-0.061	-0.102	0.60	2.48	253	17	28
533	-0.061	-0.102	0.60	2	290	35	36
534	-0.073	-0.120	0.61	1.88	344	25	25
535	-0.073	-0.110	0.66	1.97	403	25	25
541	-0.073	-0.130	0.56	1.75	442	22	28
542	-0.073	-0.140	0.52	1.53	435	27	29
543	-0.061	-0.130	0.47	1.57	390	17	23
545-A ^a	-0.061	-0.165	0.37	1.00	460	25	28
545-B ^a	-0.061	-0.165	0.37	0.96	470	23	18
546-A ^a	-0.061	-0.185	0.33	1.02	454	26	31
546-B ^a	-0.061	-0.185	0.33	0.99	460	35	35
547-A ^a	-0.061	-0.204	0.30	0.83	518	29	14
547-B ^a	-0.061	-0.204	0.30	0.76	530	23	6
548-A ^a	-0.061	-0.220	0.28	-	-	-	-
548-B ^a	-0.061	-0.220	0.28	0.71	595	32	17
549	-0.061	-0.204	0.30	0.81	535	22	16
550-A ^a	-0.061	-0.204	0.30	0.83	470	16	3
550-B ^a	-0.061	-0.204	0.30	0.79	490	25	21
550-C ^a	-0.061	-0.204	0.30	-	-	-	58
550-D ^a	-0.061	-0.204	0.30	-	-	-	103
551	-0.061	-0.204	0.30	0.87	565	19	14
559	-0.061	-0.195	0.31	0.78	527	19	10
560	-0.061	-0.220	0.28	0.68	584	16	12

a) samples with index A and B (A-D for sample 550) were produced simultaneously in one sample holder. The holder rotated with 2 RPM to have the same conditions for both substrates.

Chapter 5

Sample Analysis

5.1 Stoichiometry

5.1.1 Auger electron spectroscopy (AES)

In general Auger electron spectroscopy is utilized to check the purity of substrates and films and to investigate the composition of the samples after deposition (fig. 5.1). Since the samples are insulators, the samples are typically electrically charged after the deposition, leading to a shift of the spectrum by about 140 eV. Also, the Co peak was very weak or completely undetectable for all samples. Therefore, the AES has not been used to gather any information about the stoichiometry of the sample.

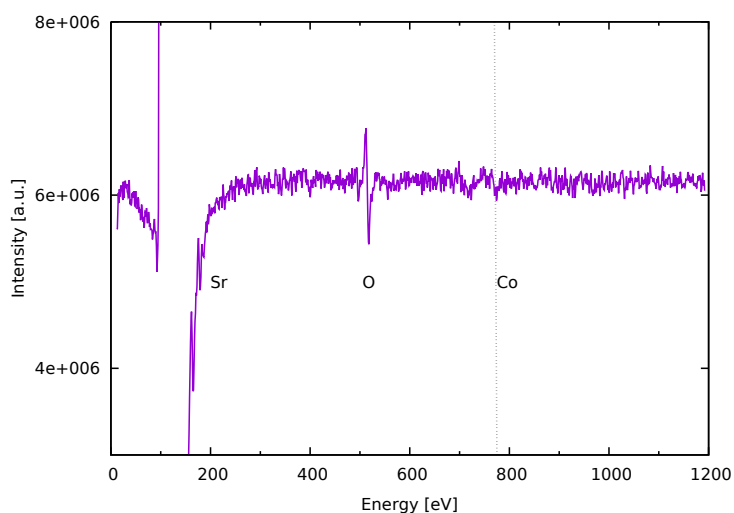


Figure 5.1: Auger electron spectrum of sample 473 after deposition. The Sr and O peaks are visible, but the Co peak is extremely weak. Because the sample was charged after the deposition, elemental peaks are shifted by about 140 eV. The typical intensity onset which for an uncharged SrCoO_x sample occurs at ~ 20 eV starts at ~ 160 eV.

5.1.2 Rutherford backscattering spectroscopy (RBS)

The Rutherford backscattering spectroscopy measurements for samples 465 - 496 and 545A - 550B were performed and analysed by Dr. Jürgen Schubert and Willi Zander (Peter Grünberg Institut (PGI-9), Forschungszentrum Jülich), the samples 510 - 543, 549 and 551 - 560 were performed and analysed by Dr. René Heller (Institute of Ion Beam Physics and Materials Research, Helmholtz-Zentrum Dresden-Rossendorf).

In fig. 5.3 RBS measurements of samples with the perfect stoichiometry (545-A,B and 546-A,B) can be found. For the samples prepared on MgO substrates the peaks are separated, since the substrate doesn't contain any elements present in the film. The STO substrates, on the other hand, also contain Sr. A simulation of separated film and substrate contributions for sample 545-A is given in fig. 5.2. Because of the thickness of the substrate (0.5 mm, which is effectively infinite for RBS), the substrate signal is not peak- but step shaped, as the ions have a limited penetration depth. For this reason the substrate signal is a plateau towards zero energy. The Sr signal of the substrate and film are not separated, as the Sr of the film contributes to the substrate signal at the high energy edge. The Co peak, which is at lower energy because the mass of Co is lower than that of Sr, contributes also to the signal. However the substrate contains no Co, so Co can be easily distinguished from the substrate signal. The Ti signal of the simulation is at a higher energy than the peak in the measurement because the ions lose energy in the film and thus the energy of the substrate signal is lowered.

With respect to a distinction of the surface signal MgO is a good substrate. The Mg signal in MgO substrates also exhibits a step shape, but, as Mg is much lighter than Sr or Co, its signal begins at a much lower energy, so there is no MgO substrate contribution at the relevant energy range of the Co and Sr peaks.

For the individual peaks on the MgO substrate, the elemental signals can be integrated to get the area density and thereby the stoichiometry. For the STO substrates, because of the overlap of signal, this is not possible, so the spectrum has to be fitted.

Figures 5.4 and 5.5 show the ratio of the QCM frequency changes for Co and Sr, in relation to the measured ratio of Co to Sr in the samples by RBS,

$$R = \frac{Co}{Sr}, \quad (5.1)$$

where Co and Sr represent the QCM frequency changes.

The uncertainty for the QCM frequency changes was evaluated for Co and Sr separately by calculating their standard deviation ($\Delta\overline{Co}$ and $\Delta\overline{Sr}$) from the set mean value (\overline{Co} and \overline{Sr} , see table.4.1), which was then used to calculate the error of the ratio ($\Delta\overline{R}$) by the standard differential error propagation formula

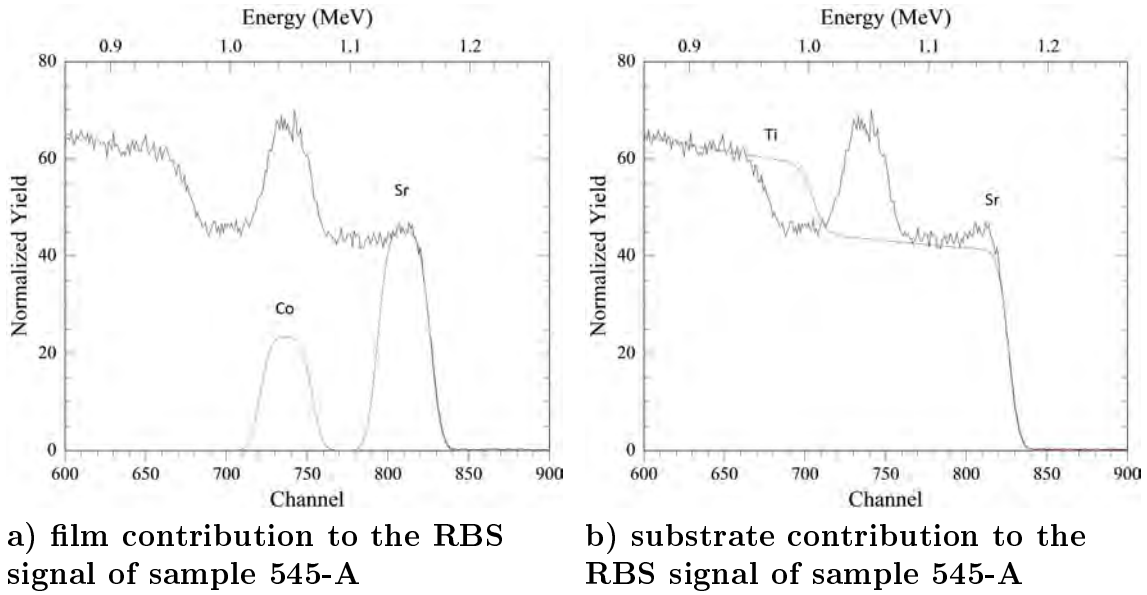


Figure 5.2: Simulation of the film signal of sample 545-A without a substrate (a) and of the pure substrate (b). (Measurement performed by Jürgen Schubert and Willi Zander (PGI-9, Forschungszentrum Jülich)).

$$\begin{aligned}
 \Delta \bar{R} &= \sqrt{\Delta \bar{C}_o^2 \left[\frac{\delta R}{\delta C_o} \right]^2 + \Delta \bar{S}_r^2 \left[\frac{\delta R}{\delta S_r} \right]^2} \\
 &= \sqrt{\Delta \bar{C}_o^2 \left(\frac{1}{\bar{S}_r} \right)^2 + \Delta \bar{S}_r^2 \left(\frac{\bar{C}_o}{-\bar{S}_r^2} \right)^2} \\
 &= \bar{R} \cdot \sqrt{\frac{\Delta \bar{C}_o^2}{\bar{C}_o^2} + \frac{\Delta \bar{S}_r^2}{\bar{S}_r^2}}.
 \end{aligned} \tag{5.2}$$

The uncertainty for the RBS measurements was estimated to be between 5 % and 10 % from the measured value for each element, and the uncertainty of the Co/Sr ratio was also calculated by formula, 5.2, by taking the upper limit of the uncertainty for each element, $\Delta \bar{C}_o$ and $\Delta \bar{S}_r$, as 10 %.

For the samples 465-486 there was no preliminary information about the correct QCM frequency changes to prepare stoichiometric samples, so, as a starting point, samples with relatively similar frequency changes were prepared (samples 465-493). The RBS analysis of these samples lead to the conclusion, that the Sr frequency change has to be higher than the Co one, to achieve a 1:1 ratio of Co to Sr. Consequently, the Co frequency change was to lowered to $-0.061 \frac{\text{Hz}}{\text{s}}$ from $-0.102 \frac{\text{Hz}}{\text{s}}$ and $-0.086 \frac{\text{Hz}}{\text{s}}$ for most subsequent samples, and the Sr frequency change was increased.

In general, the RBS Co/Sr ratio follows the QCM Co/Sr ratio with a proportionality factor of 3 (fig. 5.4).

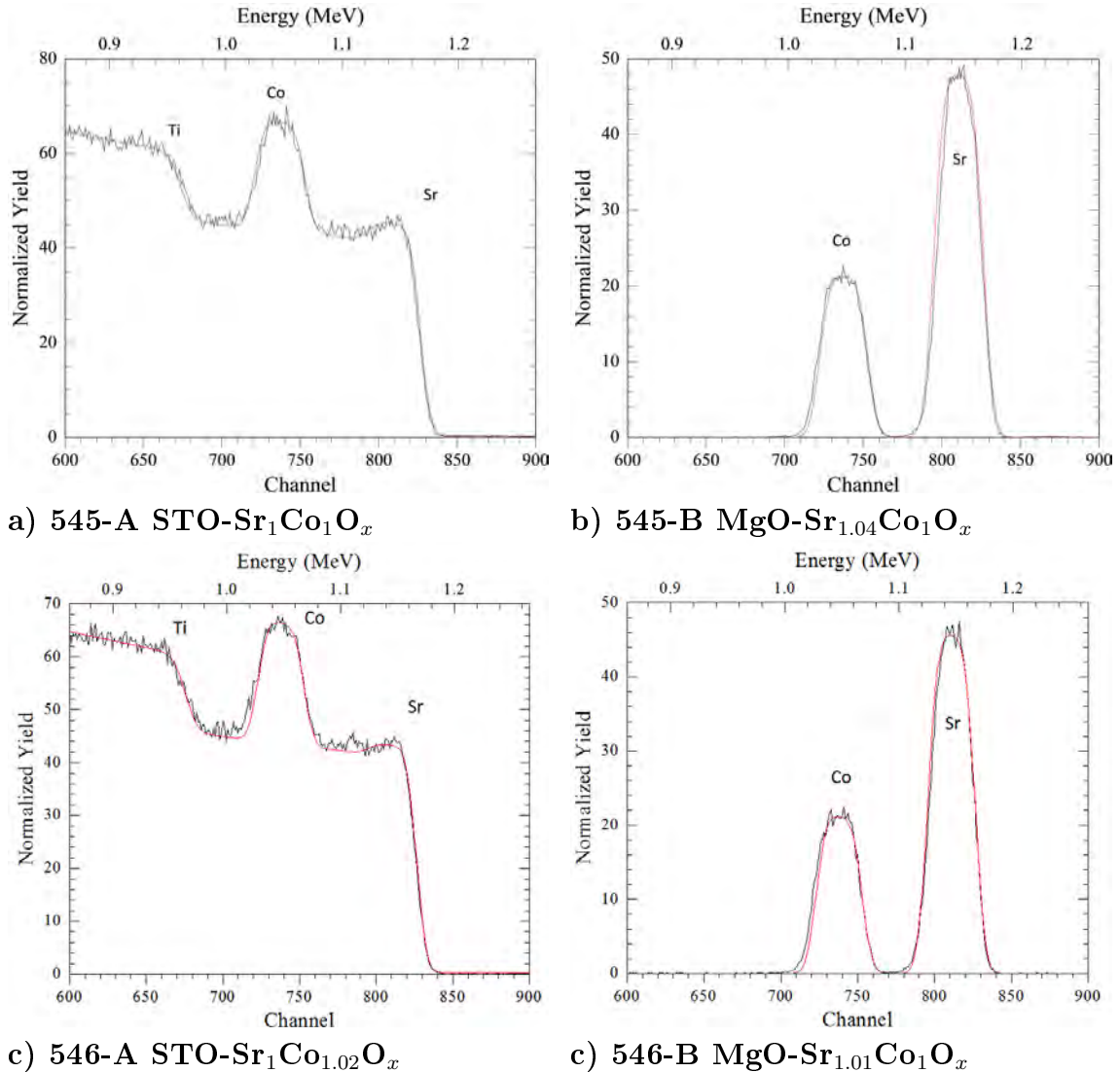


Figure 5.3: Rutherford backscattering spectroscopy measurements for samples 545-A (a) and B (b) and 546-A (c) and B (d) with fits, performed with the Program RUMP [28]. In b) and d) the peaks are separated because the substrate contains no Sr which would overlap with the film peak. Sample-pairs were produced in a double holder, so corresponding A and B samples have same deposition conditions. (Measurement performed by Jürgen Schubert and Willi Zander (PGI-9, Forschungszentrum Jülich).)

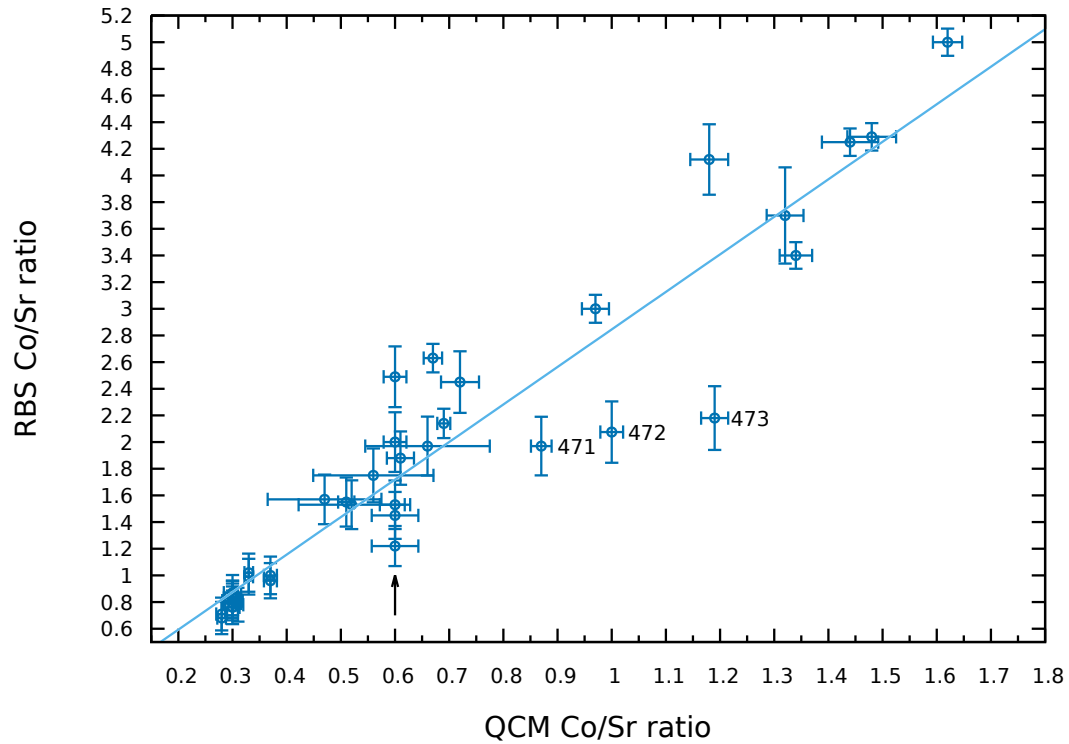


Figure 5.4: Relation of the Co/Sr frequency ratio set by the quartz crystal microbalance and the Co/Sr stoichiometry measured by Rutherford backscattering spectroscopy. An enlarged part can be found in fig. 5.5.

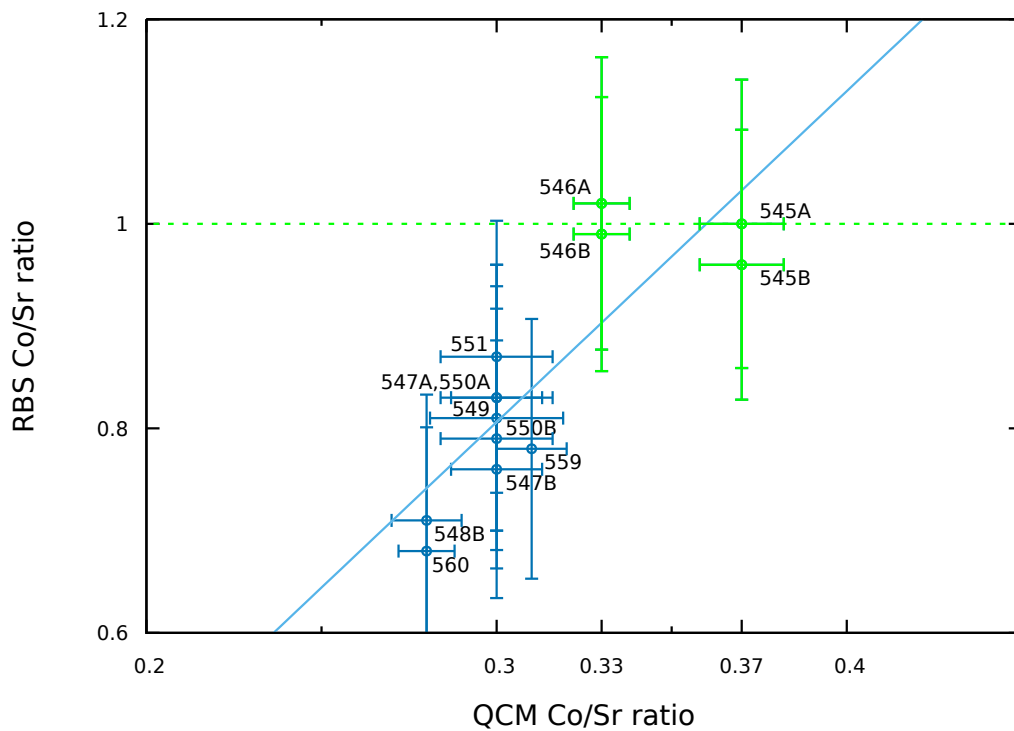


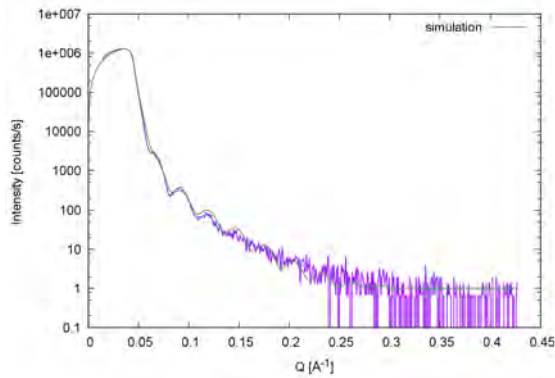
Figure 5.5: Enlarged part of fig. 5.4 around the Co/Sr ratio of 1. Comparison of the Co/Sr ratio as measured by QCM and RBS.

However, there are some samples deviating from the linear dependence, notably samples 471-473, which all have a lower RBS Co/Sr ratio than the found relationship suggests. Also, several samples were prepared at a QCM Co/Sr ratio of 0.6 (samples 510, 528, 530, 532, and 533; marked with an arrow), but the RBS Co/Sr ratio deviates quite strongly. The origin is not yet clear. Of those five samples, samples 528 & 530 and 533 & 532 were prepared as sequential pairs: after the frequency changes were set, the samples on the MgO and LaAlO substrates, 528 (MgO) and 533 (LaAlO) were prepared, and directly afterwards reference samples on STO (530 for 528 and 532 for 533) were produced. For both pairs, the RBS Co/Sr ratio deviates drastically between the corresponding samples. Between the first and second sample of each pair, the oxygen atmosphere was pumped out of the main chamber, in order to transfer the first sample out and the second in. This change of pressure (about 3-4 orders of magnitude) may have a destabilising effect on the rates of the effusion cells, causing the Co/Sr ratio to deviate. Hence, the rates of the effusion cells were not in equilibrium.

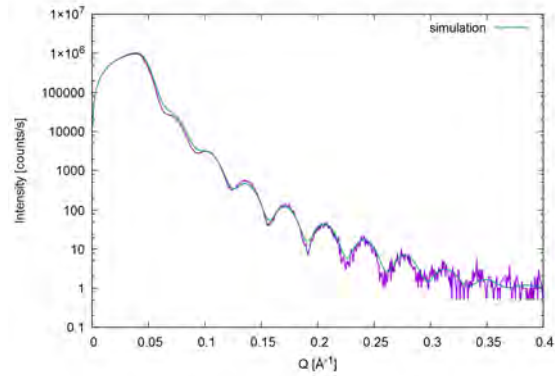
Finally, samples with Co/Sr stoichiometry of 1 were produced for a Co frequency change of $-0.061 \frac{\text{Hz}}{\text{s}}$ and a Sr frequency change of $-0.165 \frac{\text{Hz}}{\text{s}}$ for samples 545-A STO-Sr₁Co₁O_x and 545-B MgO-Sr_{1.04}Co₁O_x and for the same Co frequency change and a Sr frequency change of $-0.185 \frac{\text{Hz}}{\text{s}}$ for samples 546-A STO-Sr₁Co_{1.02}O_x and 546-B MgO-Sr_{1.01}Co₁O_x (see figs. 5.3 and 5.5). That means, a Co/Sr frequency change ratio between 0.33 ± 0.01 and 0.37 ± 0.01 is required for a stoichiometry of 1. The deposition time for the stoichiometric samples was 120 min, with a rate of $3.8 \frac{\text{\AA}}{\text{min}}$.

5.2 X-ray reflectometry (XRR)

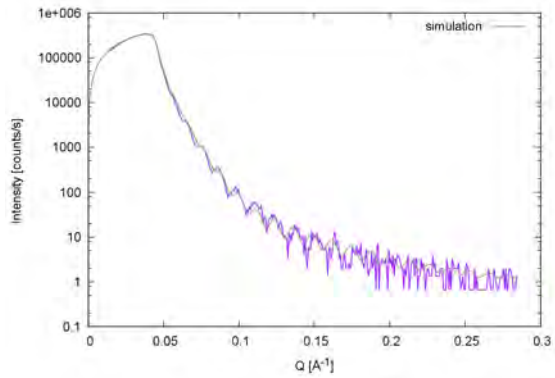
To determine the thickness and global roughness of the samples, X-ray reflectometry was performed with the Bruker D8 reflectometer of the neutron optics group of the Heinz Maier-Leibnitz Zentrum (table 4.2 and fig. 5.6). Fig. 5.6 gives examples for samples of different thickness and stoichiometry. The data evaluation was performed with the software plot.py [29]. A good fit of the data was not always possible, because of the low thickness of some samples. Also, it was often not possible to fit the sample as a single layer on the substrate, but a second layer of about 10 Å and a roughness between 7 Å and 9 Å had to be simulated.



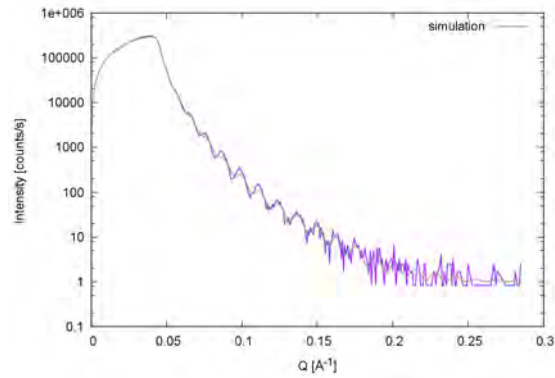
a) 473, Co/Sr: 2.18,
thickness = 204 Å



b) 484, Co/Sr: 5, thickness = 162 Å



c) 545-A, Co/Sr: 1,
thickness = 460 Å



d) 546-A, Co/Sr: 1.02,
thickness = 465 Å

Figure 5.6: XRR data and fit for samples 473 (a), 484 (b), 545-A (c), and 546-A (d). A good fit for sample 473 was not possible. The fit for sample 484 agrees very well with the data.

5.3 Atomic force microscopy (AFM)

To determine the topography and roughness of the samples on a local level, atomic force microscopy was performed. To discuss the different topographies, the scans with similar surface features are grouped in one figure and the influence of different stoichiometries and preparation conditions is discussed. The samples were measured immediately after taking them out of the vacuum. All scans are of an area of $0.25\ \mu\text{m}^2$ - $4\ \mu\text{m}^2$, taken with a scan speed of one line per second, and an I-gain between 0.5 % and 1.5 %, and a P-gain of 1 %.

In the following, a selection of AFM images is shown (fig. 5.7- 5.15). For a better orientation, the stoichiometry ratio and additional growth information have been added to the images.

Samples with a Co/Sr ratio between 4.3 and 2.9 which were deposited at $750\ \text{°C}$ (fig. 5.7) reveal rounded and elongated island-like structures (465, 496, and 493), and cover most of sample 467, having holes between them. The samples 465, 496, and 493 have a roughness between $37\ \text{Å}$ and $47\ \text{Å}$, while sample 467 has the lower roughness of $25\ \text{Å}$. The typical height difference between the islands and holes is about $150\ \text{Å}$ for sample 465 and $200\ \text{Å}$ for sample 467, 486, and 493 (see fig. 5.7c,d), which is in the range of the total film thickness for each sample. This means that during deposition the film didn't grow layer-by-layer, but rather grew into the islands seen in the AFM images.

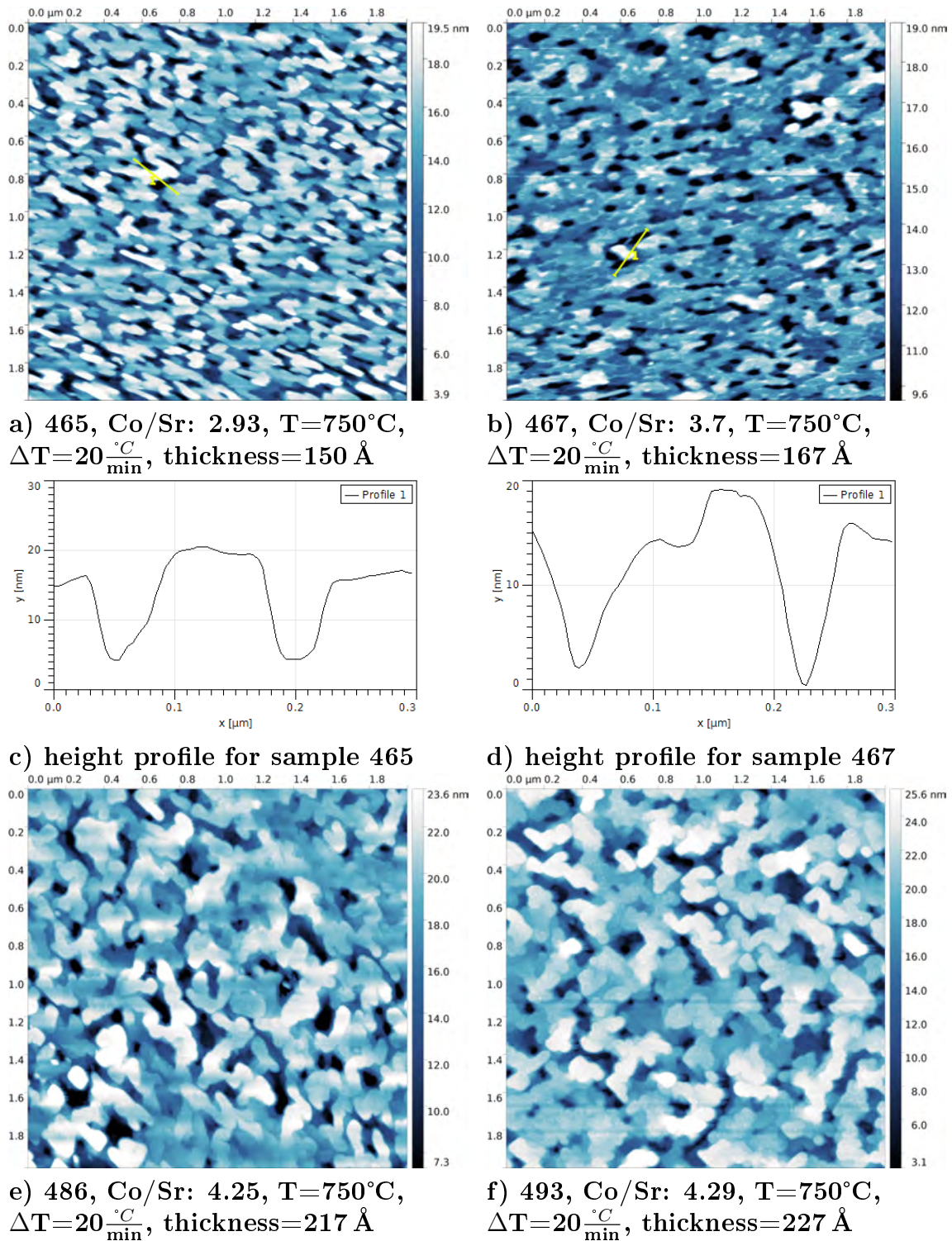


Figure 5.7: AFM topography for samples 465 (a), 467 (b), 486 (e), and 493 (f), and height profiles for samples 465 (c) and 467 (d) along the lines indicated in the respective topography scans. The Co/Sr ratio, growth temperature (T), cooling rate (ΔT), and thickness are given.

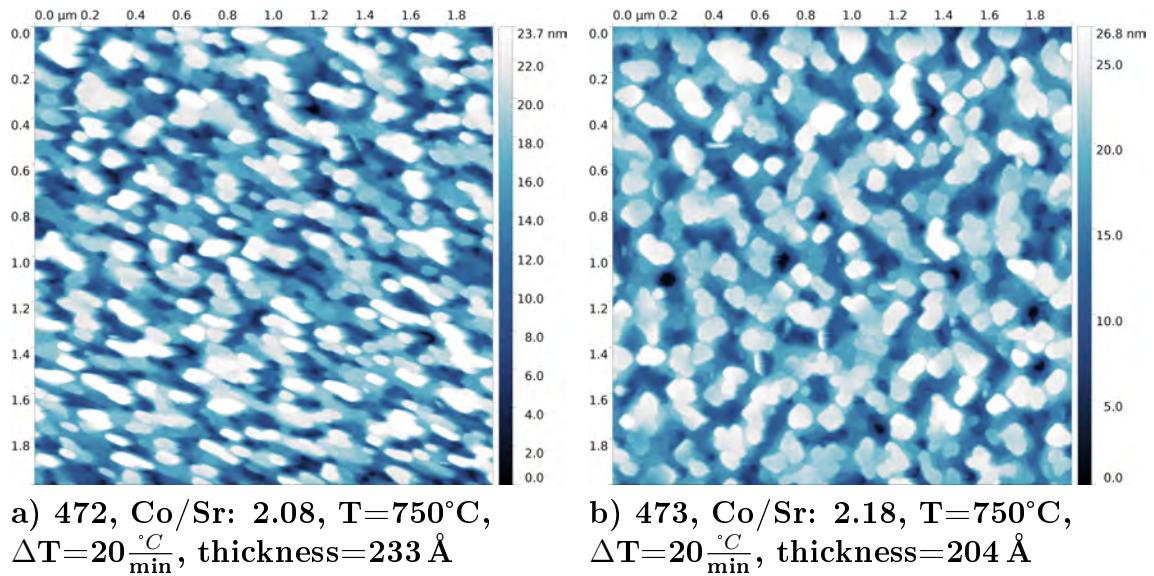


Figure 5.8: AFM topography for samples 472 (a), and 473 (b). There is some left-to-right drift in the scan of sample 472. The Co/Sr ratio, growth temperature (T), cooling rate (ΔT), and thickness are given.

Samples 472 (Co/Sr 2.08) and 473 (Co/Sr 2.18) reveal very similar topographies, composed of islands, with height differences between the islands and holes of 200 Å for sample 472 and 230 Å for sample 473.

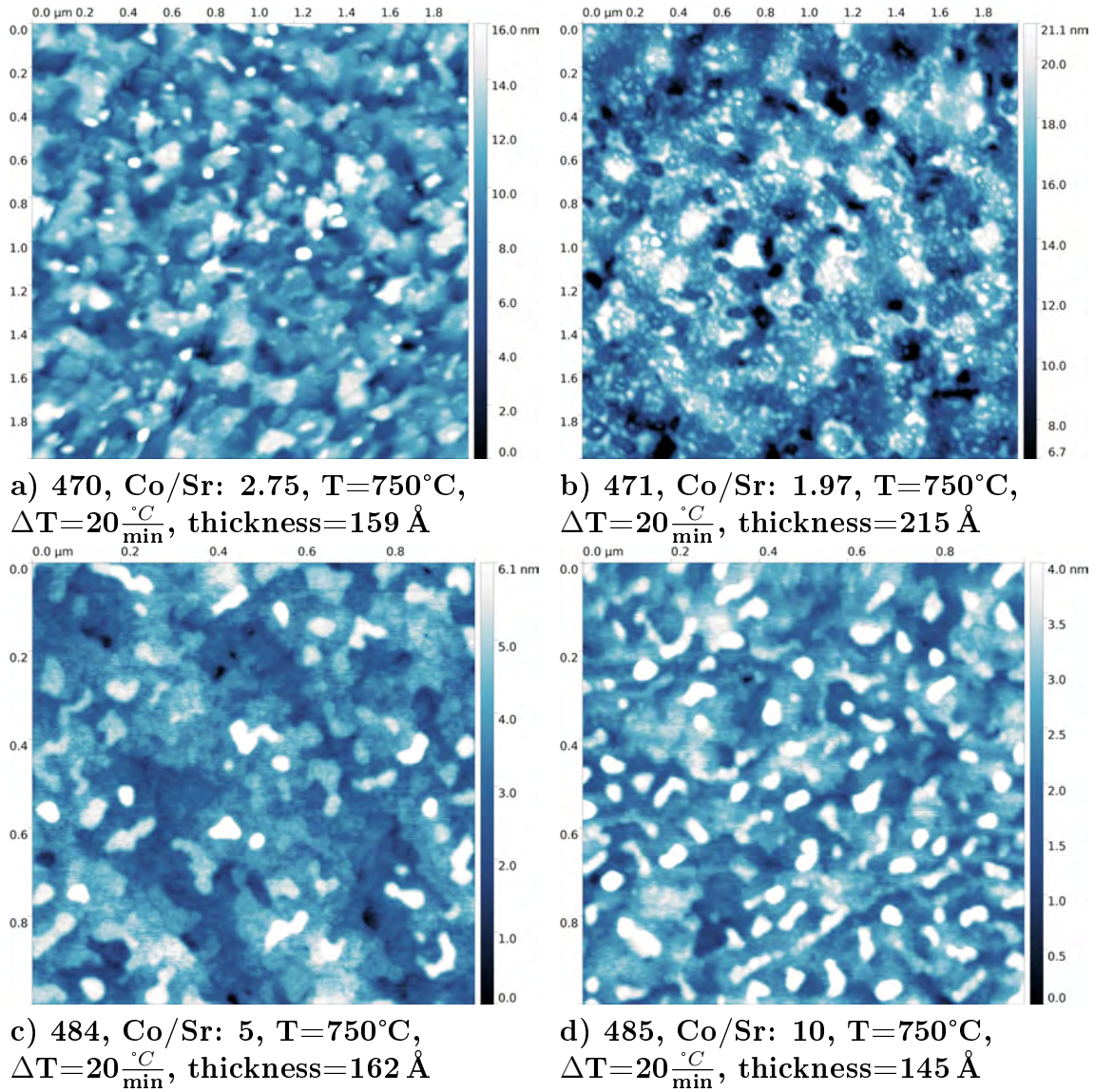


Figure 5.9: AFM topography for samples 470 (a), 471 (b), 484 (c), and 485 (d). The Co/Sr ratio, growth temperature (T), cooling rate (ΔT), and thickness are given.

Samples 470 (Co/Sr 2.75) and 471 (Co/Sr 1.97) have a cloud-like structure (fig. 5.9 a and b). They exhibit roughnesses of 26 Å and 30 Å, with a height difference between the islands and holes of 170 Å and 230 Å, which is again around the measured total thickness of the film.

The samples with the largest RBS Co/Sr ratio, 484 and 485 (Co/Sr of 5 and 10), reveal a similar, very smooth structure with a roughness of 10 Å, and height differences between of 80 Å and 47 Å (fig. 5.9 c and d), which is half the total layer thickness for sample 484 and one third for sample 485.

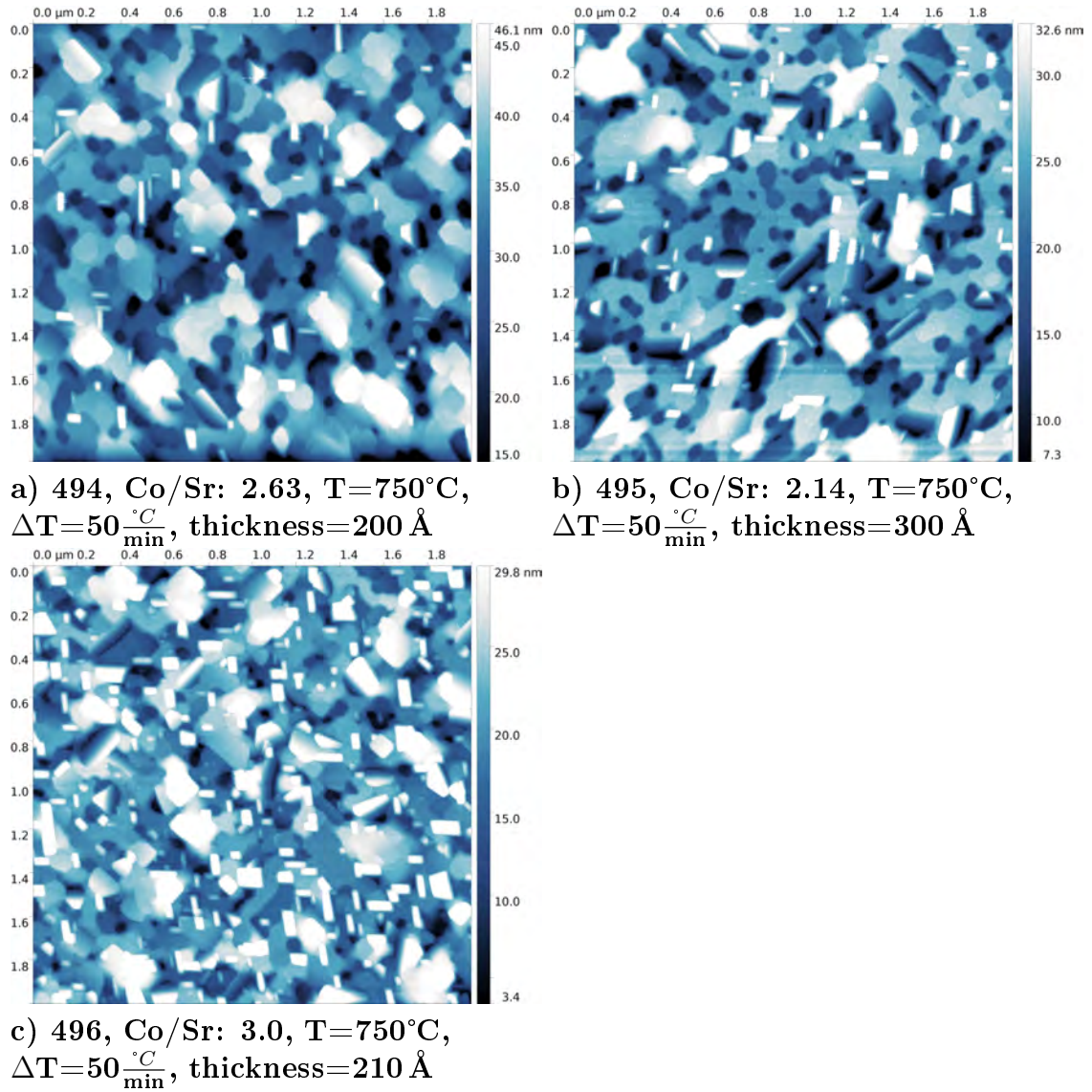


Figure 5.10: AFM topography for samples 494 (a), 495 (b), and 496 (c). The Co/Sr ratio, growth temperature (T), cooling rate (ΔT), and thickness are given.

Samples 494-496 (Co/Sr between 2.1 and 3) exhibit a very similar structure consisting of porous layers, leaving underlying layers visible, and rectangular islands, most prominently for sample 496 (fig. 5.10). They show a very high roughness of 67 Å - 71 Å, and a height differences of 350 Å for samples 494 and 495, and 500 Å for sample 496, which is 1.5 times the total layer thickness for sample 494, 50 Å more for sample 495 and more than double that for sample 496, so the film growth was very inhomogeneous.

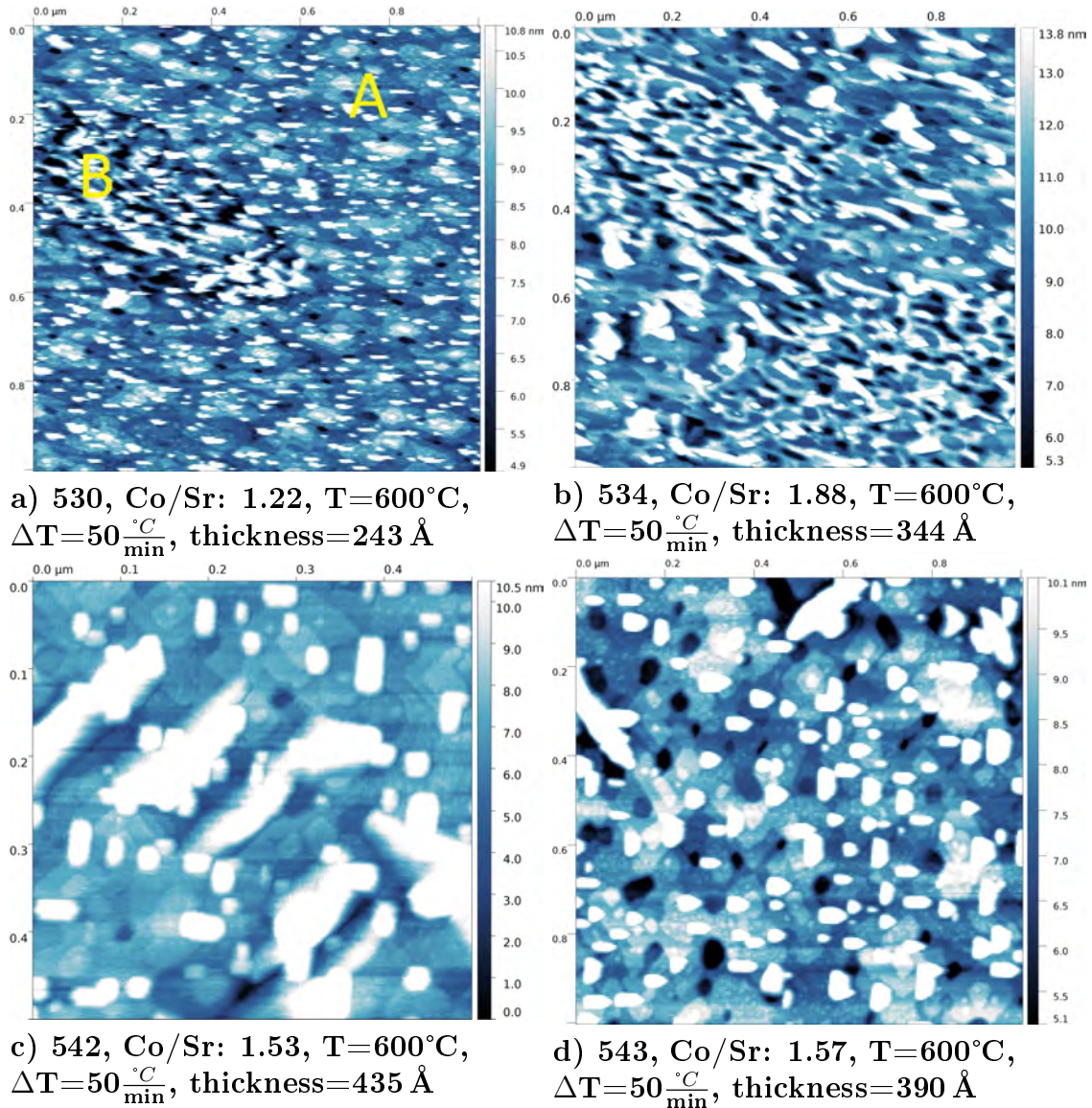
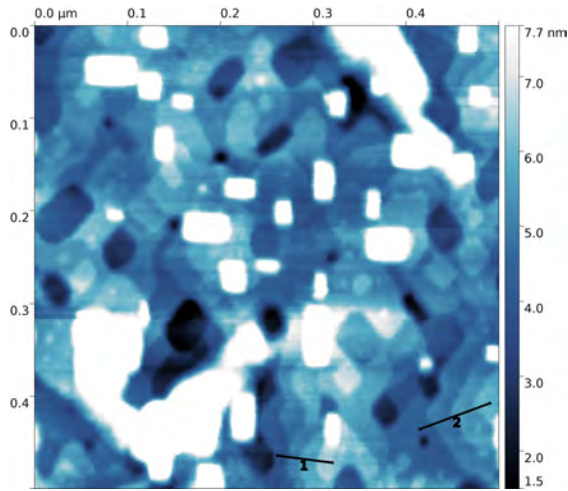


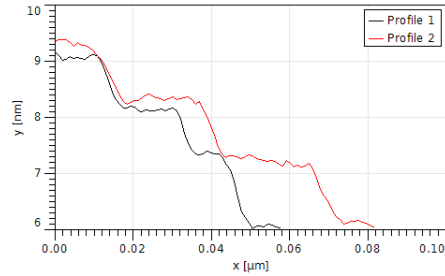
Figure 5.11: AFM topography for samples 530 (a), 534 (b), 542 (c), and 543 (d). There is some drift in the scans for samples 530 and 543, elongating some features to the right, and some noise on the scans for sample 534 and 542. The letters 'A' and 'B' in image a) denote regions with different topographic features, terraces (A) and ridges (B). The Co/Sr ratio, growth temperature (T), cooling rate (ΔT), and thickness are given.

For most samples with a Co/Sr ratio between 1.97 and 1.02 which were prepared at a deposition temperature of 600 °C (samples 530 - 546-A), rectangular islands, like for samples 494- 496 are present (fig. 5.11), but a layered terrace structure, with a step height between 8 and 13 Å, becomes visible. This is most clearly the case for sample 541 (fig. 5.12a; and region A in fig. 5.11a for sample 530). This structural change coincides with a change in growth temperature from 750 °C to 600 °C, and a decrease of the Co/Sr ratio to below 2. However, the more important change is the deposition temperature, as both samples 471 (750 °C) and 541 (600 °C)

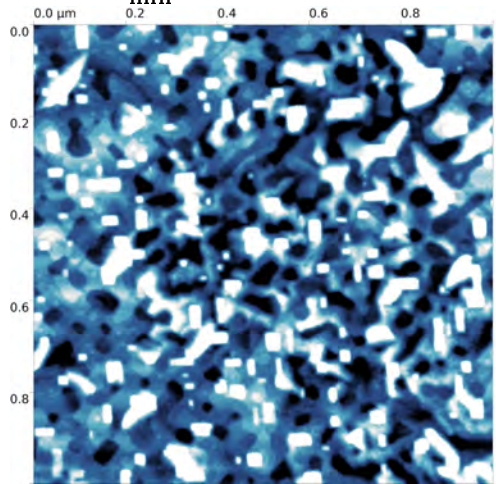
show a Co/Sr ratio of 1.97, but only the latter exhibits the terrace structure. The scans for samples 530, 534, 535, and 542 also show that the surface topography is not homogeneous, but that there are regions where the terraces give way to thin ridges and valleys (fig. 5.12; and region B in fig. 5.11a for sample 530). The total height difference for the ridge-and-valley structure is higher with 130 Å for sample 530, and 90 Å for sample 535, compared to 110 Å, and 65 Å, in the terrace region. This difference arises from a higher maximum and a lower minimum height in the ridge-and-valley region.



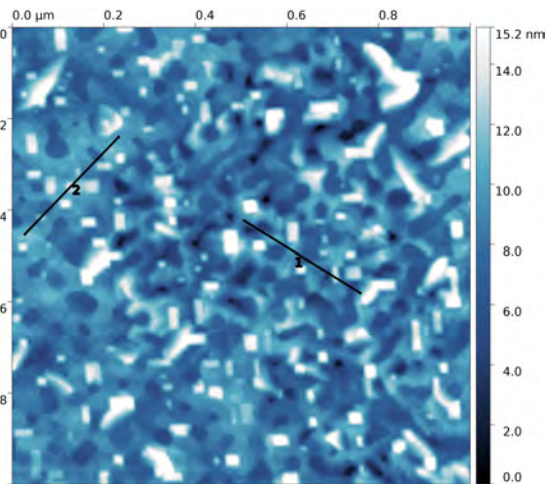
a) 541, Co/Sr: 1.75, $T=600^{\circ}\text{C}$, $\Delta T=50 \frac{^{\circ}\text{C}}{\text{min}}$, thickness=442 Å



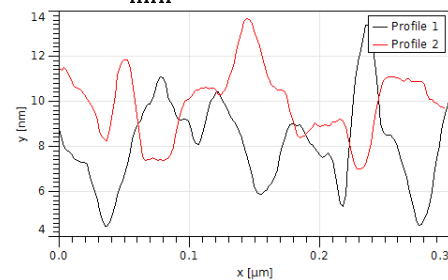
b) height profile of terraces for sample 541



c) 535, Co/Sr: 1.97, $T=600^{\circ}\text{C}$, $\Delta T=50 \frac{^{\circ}\text{C}}{\text{min}}$, thickness=403 Å

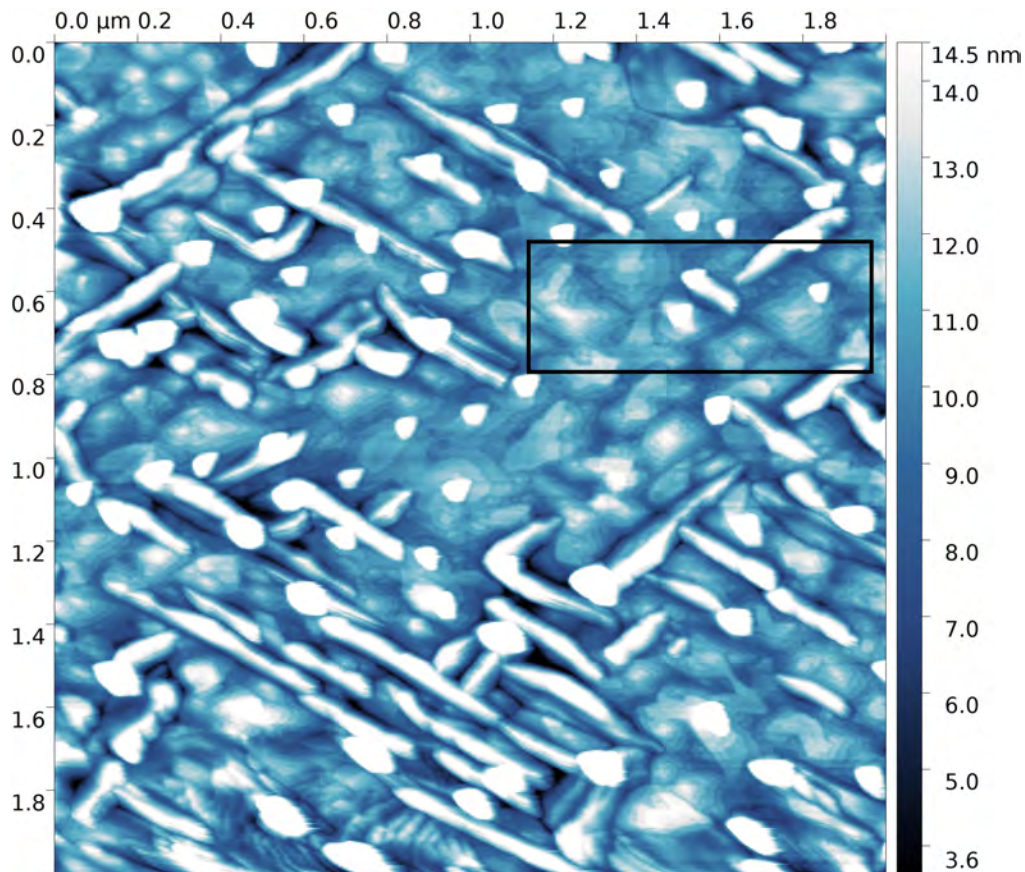


d) 535

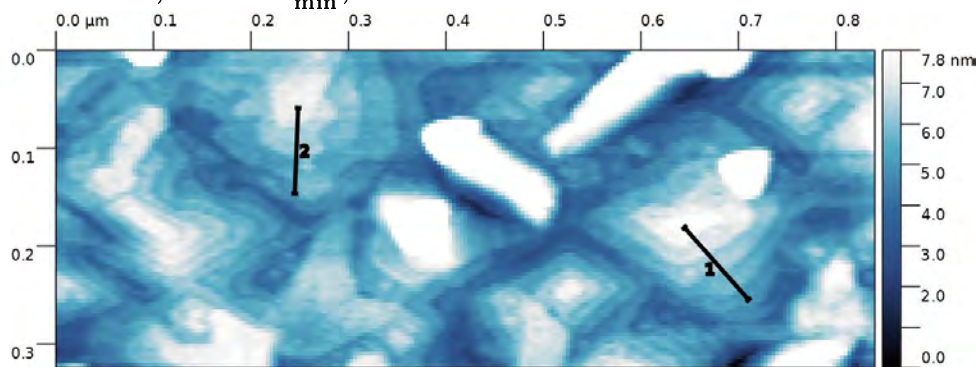


e) height profile for sample 535

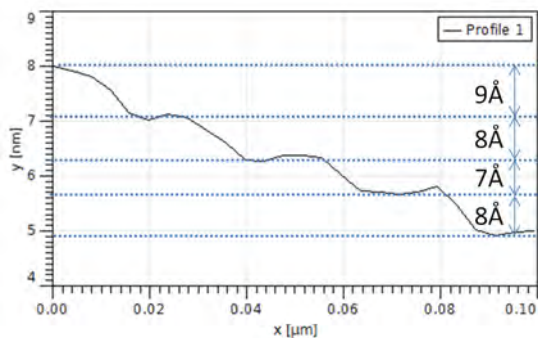
Figure 5.12: AFM topography for sample 541 (a) with the height profile (b) along the indicated line, and the topography for sample 535 with two different colour scales which emphasize the terraces (c) and the valleys (d), with the height profile (e) along the indicated lines. The Co/Sr ratio, growth temperature (T), cooling rate (ΔT), and thickness are given.



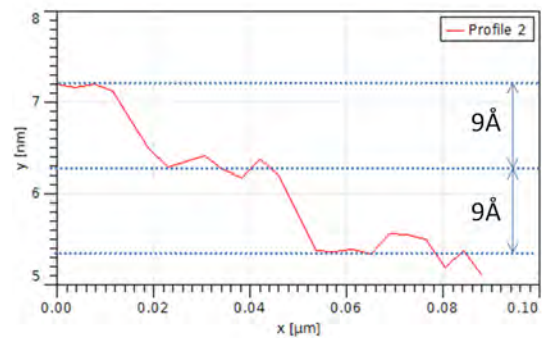
a) topography of sample 546-A, Co/Sr: 1.02, $T=600^{\circ}\text{C}$, $\Delta T=50^{\circ}\text{C}_{\text{min}}$, thickness=455 Å



b) magnified topography of sample 546-A



c) height profile 1



d) height profile 2

Figure 5.13: AFM topography for sample 546-A (a). The area of the topography indicated by the rectangle is magnified in image b. Indicated lines are given as line profiles c and d. The Co/Sr ratio, growth temperature (T), cooling rate (ΔT), and thickness are given.

The terrace and ridge structures are also present in sample 546-A (Co/Sr 1.02), though they are no longer separated in different areas, like the regions 'A' and 'B' in sample 530 (fig 5.11a), but they rather intermix (fig. 5.13). The height of the terraces typically lies between 7 and 10 Å (fig. 5.13 c and d). The roughness of sample 546-A is 30 Å and it has a total height difference of 260 Å, which is lower than the layer thickness of 454 Å.

The terraces could originate from incomplete BM-SrCoO_x layers, as the distance between the top-most O-atoms for a step size of half a unit cell is 7.90 Å (see fig. 5.14), corresponding to half of the out-of-plane lattice vector. Another possibility is, that the terraces indicate a CoO terminated surface, as the CoO lattice constant is 4.26 Å, which means a step height of two unit cells would be 8.52 Å. However, no CoO_x is observed in XRD (chapter 5.4.3). Further measurements are required to determine the origin of the terrace structure.

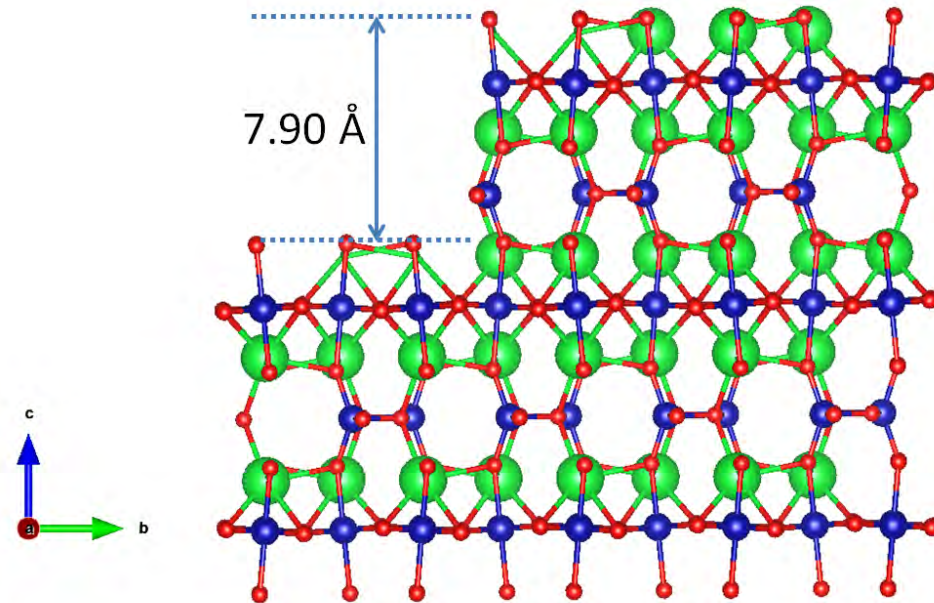


Figure 5.14: Crystal structure of BM-SrCoO_x with terraces of half a unit cell in height as a possible origin of the terraces observed for samples 530 - 546-A. The distance between the O-atoms (red) in the BM-SrCoO_x structure (arrow) is 7.90 Å. Co atoms are given in blue and Sr in green.

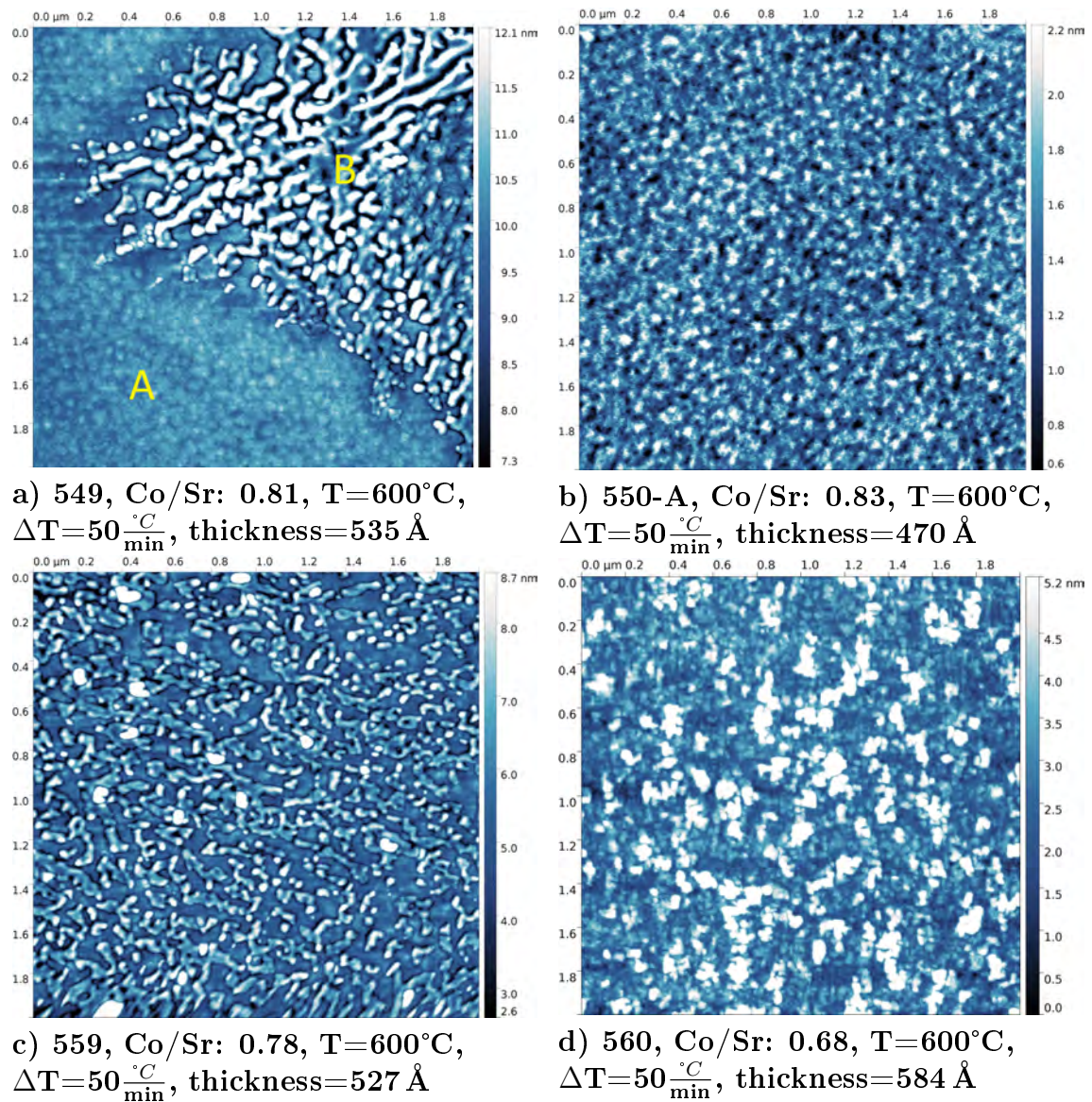


Figure 5.15: AFM topography for samples 549 (a), 550-A (b), 559 (c), and 560 (d). The letters 'A' and 'B' denote regions in image a) with different topographic features, very flat area (A) and ridges (B). The Co/Sr ratio, growth temperature (T), cooling rate (ΔT), and thickness are given.

When the Co/Sr ratio is below 1, the topography becomes inhomogeneous, as sample 549 (Co/Sr 0.81) has a ridged structure that has a roughness of 20 Å and a very flat area with a roughness of 3 Å (regions A and B in figure 5.15). These two topographic features are also reflected in the scan for samples 550-A (Co/Sr 0.83), which is a very flat sample with a roughness of 3 Å, and sample 559 (Co/Sr 0.78), which has the ridged structure of region B. For both samples scans from different areas on the sample were taken, but there was no indication of the other topographical feature, i.e. no ridges in the measurements for sample 550-A and no flat areas in sample 559. Although samples 549 and 559 share the ridged structure, the roughness of sample 559 is with 10 Å half that of sample 549. Sample 560

(Co/Sr 0.68) has a "flaky" structure, composed of many islands. The roughness for this sample varies between 9 and 14 Å between scans of different regions of the sample.

When comparing all samples with respect to the AFM measurements it seems that for a Co excess the exact Co/Sr ratio has less influence on the topography than the preparation parameters like temperature, cooling rate and deposition time. The samples 473 and 495 have a very similar Co/Sr ratio with 2.18 and 2.14, but they exhibit quite different topographies, namely islands for Sample 473 (fig. 5.8a) and a porous layer and rectangular islands for sample 495 (fig. 5.10b). The difference in preparation parameters is that for sample 495 the film was deposited for 120 min, which is twice the deposition time as for sample 473 and at a lower Co frequency change of $-0.061 \frac{\text{Hz}}{\text{s}}$ i.e. a film deposition rate of $2.5 \frac{\text{Å}}{\text{min}}$, compared to $-0.102 \frac{\text{Hz}}{\text{s}}$ i.e. $3.4 \frac{\text{Å}}{\text{min}}$. This leads to a higher thickness of 300 Å for sample 495, compared to 204 Å for sample 473. Also, the cooling rate after the deposition for sample 495 was with $50 \frac{\text{°C}}{\text{min}}$, 2.5 times higher than for sample 473. Similarly, samples 470, and 494 have Co/Sr ratios of 2.75 and 2.93, but have different structures, with a cloud-like topography for sample 470 and a porous layer with rectangular islands for sample 494. Sample 494 is again thicker because of a longer deposition time. It was prepared at a lower temperature of 600 °C compared to 750 °C for sample 470, but a higher cooling rate with $50 \frac{\text{°C}}{\text{min}}$ compared to $20 \frac{\text{°C}}{\text{min}}$. The samples 471 and 535 have the exact same Co/Sr ratio of 1.97 but different preparation temperatures and cooling rates (750 °C and $20 \frac{\text{°C}}{\text{min}}$ to 600 °C and $50 \frac{\text{°C}}{\text{min}}$). They also have different deposition times (60 min for sample 471 and 120 min for sample 535), which results in twice the thickness for sample 535. The change in preparation conditions again leads to different topographies, namely a cloud-like structure for sample 471 and a terrace and ridge structure for sample 535.

On the other hand, samples with different Co/Sr ratios but similar deposition conditions tend to have similar structures, like the terraces and ridges for samples 530 (Co/Sr 1.22) and 535 (Co/Sr 1.97). This means that the structure is reproducible for similar conditions and can be changed by tuning the deposition parameters.

If the samples become Co deficient however, like for samples 549 - 560 (Co/Sr 0.81-0.68) the topography changes a lot and no longer forms terraces that were prevalent for samples 530 - 546-A (Co/Sr 1.97-1.02).

Comparison of the roughness obtained from XRR and AFM

A comparison of the roughness obtained by AFM and XRR reveals that the AFM roughness is larger in general (fig. 5.16). Assuming a linear dependence between the roughness, i.e.

$$R_{XRR} = a \cdot R_{AFM} + b, \quad (5.3)$$

with the roughness obtained by XRR, R_{XRR} , and by AFM, R_{AFM} , the fit results in

$$a = (0.56 \pm 0.08); b = (9 \pm 3) \text{ \AA}. \quad (5.4)$$

The given error is the pure fitting error, and this fit is not meant to describe an exact dependence, but rather describes a tendency.

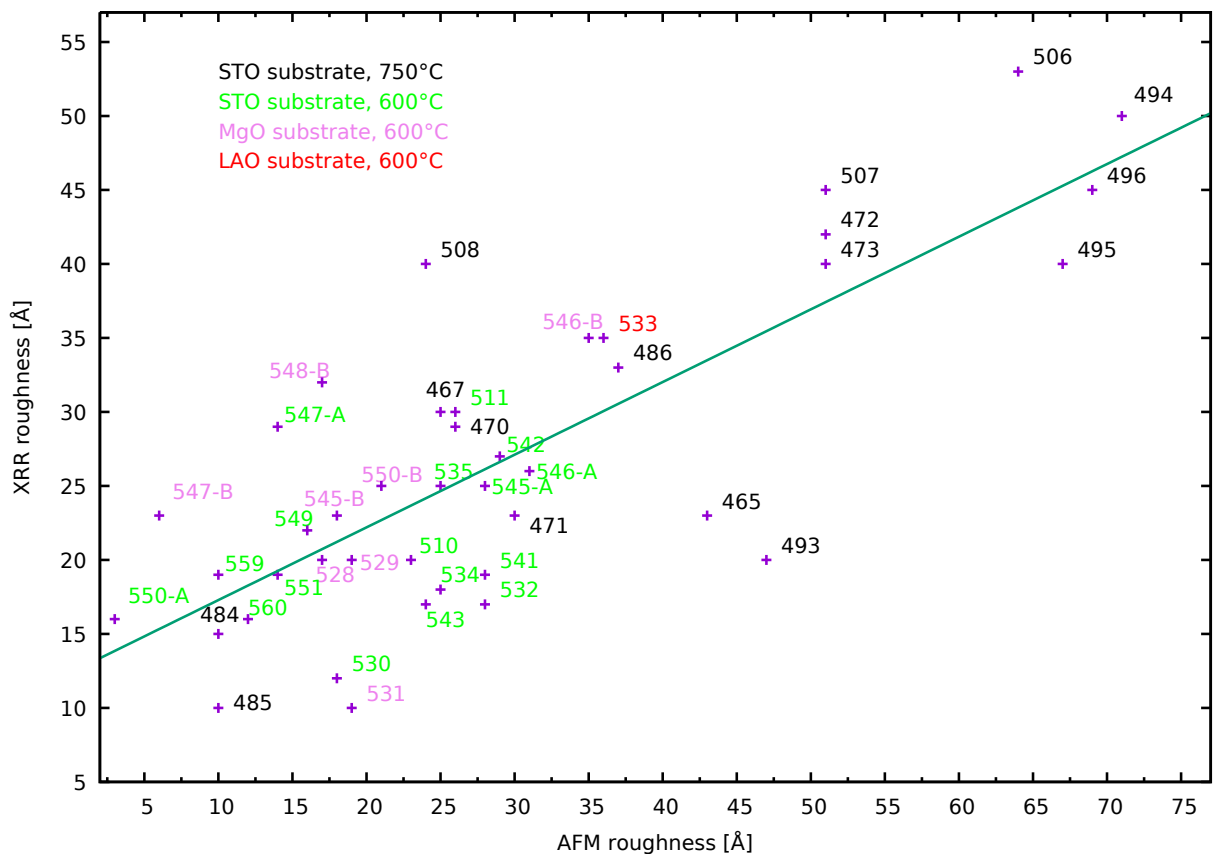


Figure 5.16: Comparison of the roughness measured by AFM and XRR. A linear dependence of the form $R_{XRR} = 0.56 \cdot R_{AFM} + 9$ was fitted (see eq. 5.3).

5.4 Crystallinity

5.4.1 Low energy electron diffraction (LEED)

LEED was performed to study the crystallinity and, if possible, to determine the structure of the thin film surfaces.

Figs. 5.17- 5.19 show the fluorescent screen with the bright Bragg spots, and the electron source blocking the centre of the image. From the distance of the Bragg spots at a given acceleration voltage, the in-plane lattice constants can be calculated by

$$\frac{1}{d} = \frac{a\sqrt{2m_e e}}{hR} \sqrt{U}, \quad (5.5)$$

with the distance between Bragg spots d , the lattice constant a , the electron mass m_e , the elemental charge e , the Planck constant h , the screen radius R , and the acceleration voltage U (see chapter 3.5). To get a mean value for the lattice constant one can plot $\frac{1}{d}$ against \sqrt{U} for multiple voltages and fit linearly. The slope s of the fit corresponds to the factor $\frac{a\sqrt{2m_e e}}{hR}$, which leads to the equation for the lattice constant

$$a = \frac{shR}{\sqrt{2m_e e}}. \quad (5.6)$$

For sample 471 the slope is $6.4 \frac{1}{\text{\AA}\sqrt{\text{V}}}$ (Fig. 5.17 e). Using equation 5.6 reveals a lattice constant of 5.7\AA for sample 471. Since the Bragg spots are not point-sized, but rather have a certain extension, there is an intrinsic error in measuring the distance between spots, which is estimated to be 4 pixel, or about 1 mm, for the screen size of 104 mm. To determine if it is possible to distinguish the two in-plane lattice parameters of BM-SrCoO_x which deviate by 0.104\AA (see page 10 for the theoretical explanation), the distance in Bragg spots for the a and b lattice constants of BM-SrCoO_x can be calculated for a voltage of 100 V to differ by

$$\Delta d = \frac{hR}{a_{BM}\sqrt{2m_e eU}} - \frac{hR}{b_{BM}\sqrt{2m_e eU}} = 0.3 \text{ mm}, \quad (5.7)$$

which is much lower than the intrinsic error, so the two different in-plane lattice constants can not be distinguished via LEED. The error of the lattice constant for all samples is estimated to be about 0.3\AA .

Twelve samples exhibit a LEED pattern (see table 5.1). Nine of them have a lattice constant that fits well to the BM-SrCoO_x lattice constants, all of them have a Co/Sr ratio below 2. The other three samples exhibit a lower lattice constant between 3.1 and 3.2\AA and a visible surface reconstruction (samples 467 (2x2 reconstruction) and 547-A (4x4 reconstruction)).

However, samples that don't reveal a LEED pattern may still be crystalline with respect to the bulk. If these samples are insulators, they may exhibit a charge

effect which hinders the investigation with LEED. This could also be the reason why all BM-SrCoO_x patterns generally exhibit a much lower intensity than the annealed substrate. Also, as LEED is only sensitive to the first few atomic layers, an amorphous top-layer would yield a diffuse screen, but would not exclude the existence of a crystalline structure in bulk.

On the next pages, the LEED patterns are shown (Figs. 5.17 - 5.19). Fig. 5.20 relates the Co/Sr ratio of samples with the existence of a LEED pattern. As can be seen, a lattice constant which is consistent with BM-SrCoO_x only occurs for a Co/Sr ratio below 2.

Table 5.1: Lattice constants calculated from LEED images

Sample Number	LEED lattice constant ^a [Å]	Co/Sr ratio
467	3.09 ± 0.06	3.70
472	3.08 ± 0.01	2.08
471	5.69 ± 0.03	1.97
535	5.56 ± 0.04	1.97
534	5.58 ± 0.04	1.88
541	5.55 ± 0.05	1.75
543	5.60 ± 0.02	1.57
510	5.61 ± 0.02	1.53
542	5.61 ± 0.02	1.53
530	5.58 ± 0.07	1.22
547-A	3.17 ± 0.04	0.83
560	5.58 ± 0.03	0.68

^a the error given here is the standard error of the linear fit, it does not include uncertainties pertaining to the measured distance between Bragg spots (± 0.3 Å, as described at the beginning of this chapter).

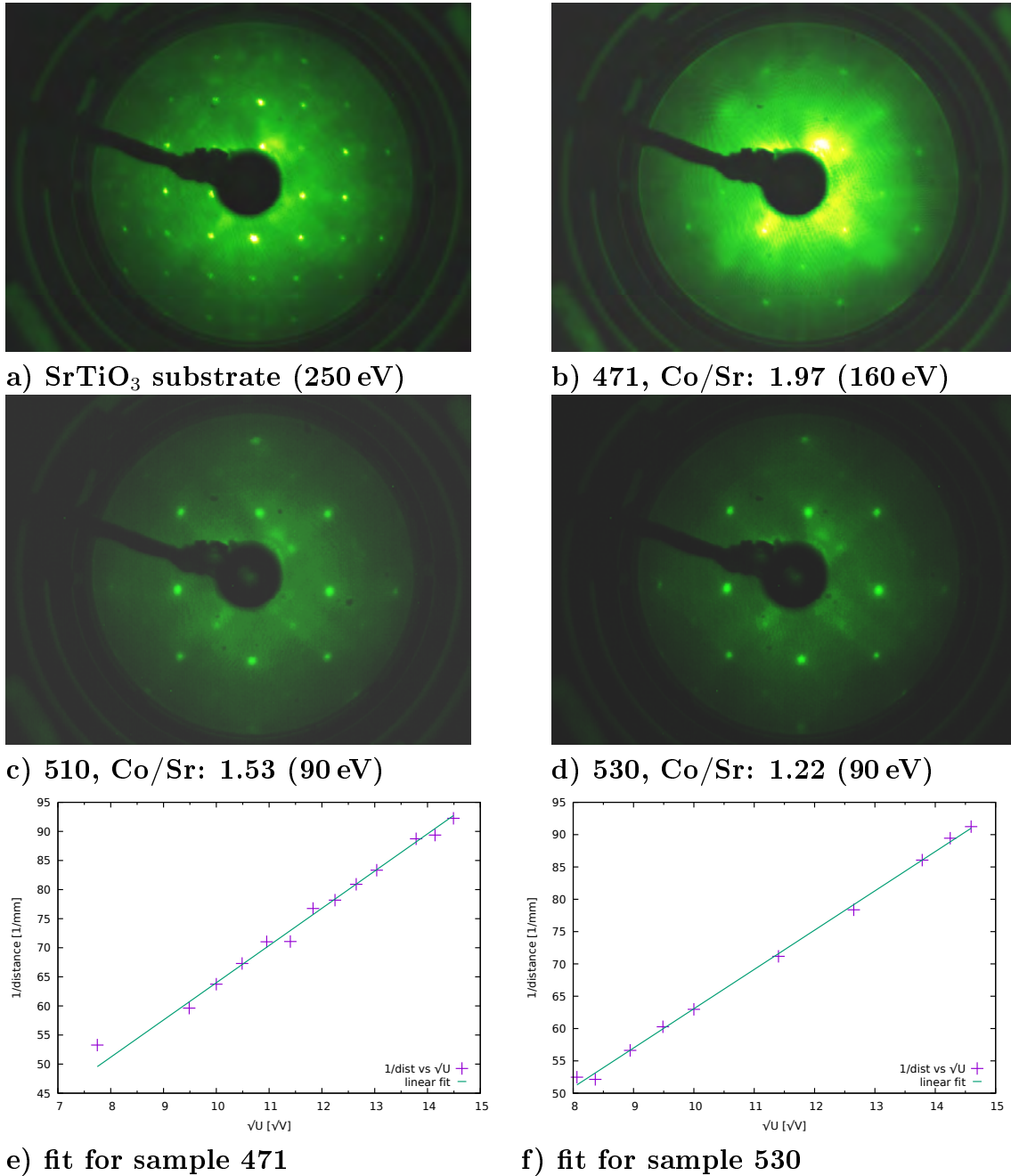
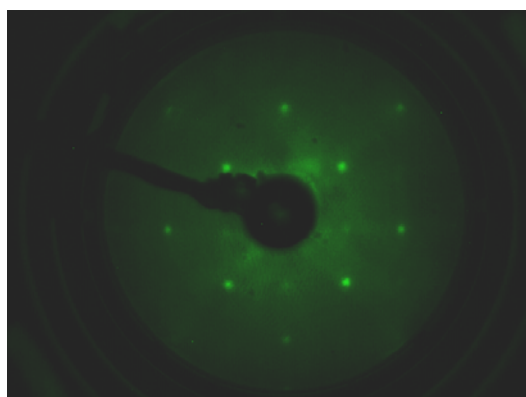
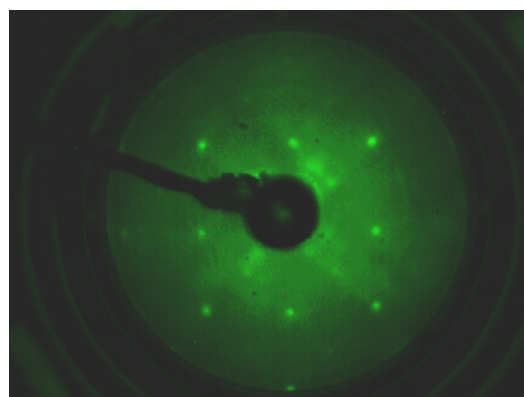


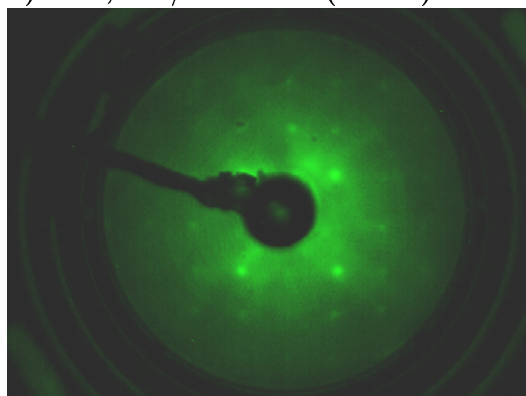
Figure 5.17: LEED images of an STO substrate at 250 eV (a) and different SrCoO_x samples with given Co/Sr ratio, sample 471 at 160 eV (b), sample 510 at 90 eV (c), and sample 530 at 90 eV (d). The brightness and contrast were optimized. In figs. (e) and (f) the inverted distance between Bragg-spots in the LEED images are plotted against the square root of the voltage according to equation 5.5. This is shown for sample 471 (e) and 530 (f), as an example. The resulting lattice constants are 5.7 Å and 5.6 Å, respectively.



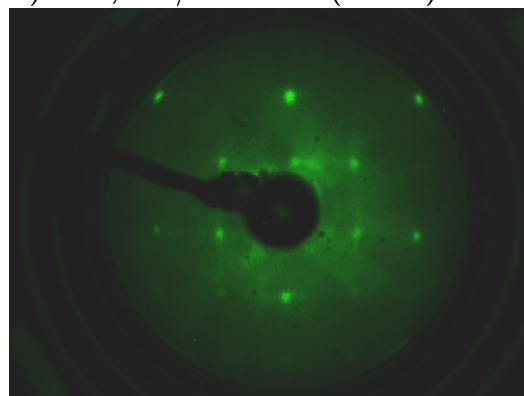
a) 534, Co/Sr: 1.88 (90 eV)



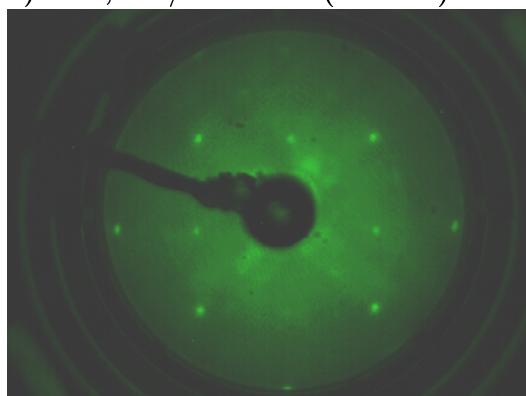
b) 535, Co/Sr: 1.97 (85 eV)



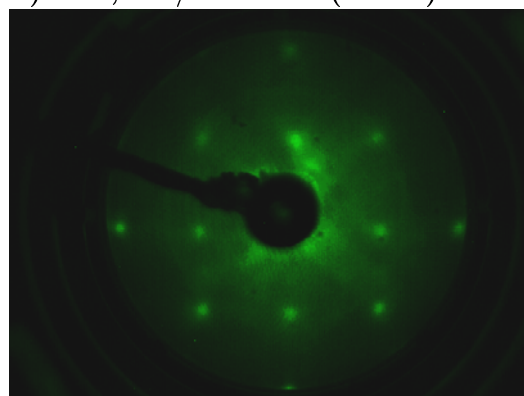
c) 541, Co/Sr: 1.75 (140 eV)



d) 542, Co/Sr: 1.53 (70 eV)

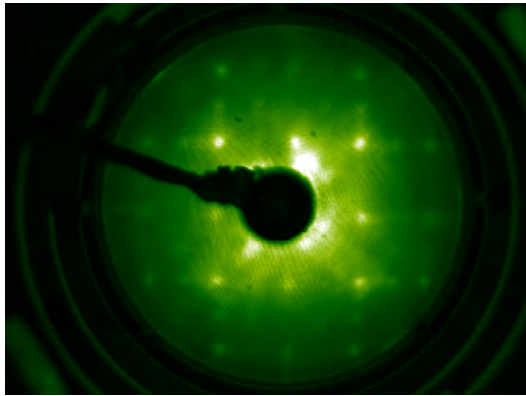


e) 543, Co/Sr: 1.57 (80 eV)

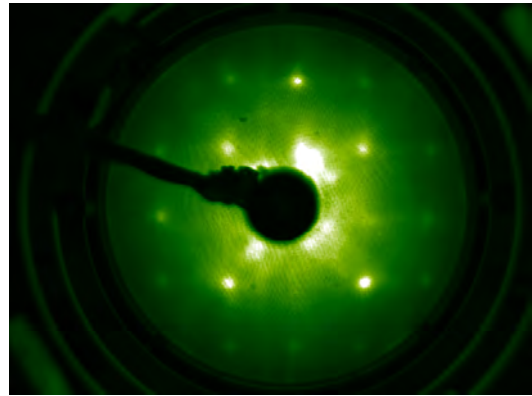


f) 560, Co/Sr: 0.68 (80 eV)

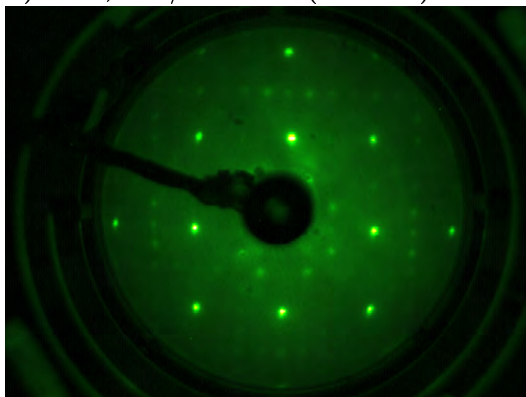
Figure 5.18: LEED images of sample 534 at 90 eV (a), sample 535 at 85 eV (b), sample 541 at 140 eV (c), sample 542 at 70 eV (d), sample 543 at 80 eV (e), and sample 560 at 80 eV (f). The brightness and contrast were optimized.



a) 467, Co/Sr: 3.7 (200 eV)



b) 472, Co/Sr: 2.08 (220 eV)



c) 547-A, Co/Sr: 0.83 (80 eV)

Figure 5.19: LEED images of sample 467 at 200 eV (a), sample 472 at 220 eV (b), and sample 547-A at 80 eV (c). The brightness and contrast were optimized. Sample 547-A has a clearly visible 4x4 superstructure. Sample 467 also has a superstructure, possibly 2x2. Obviously, the stoichiometry does not have an influence.

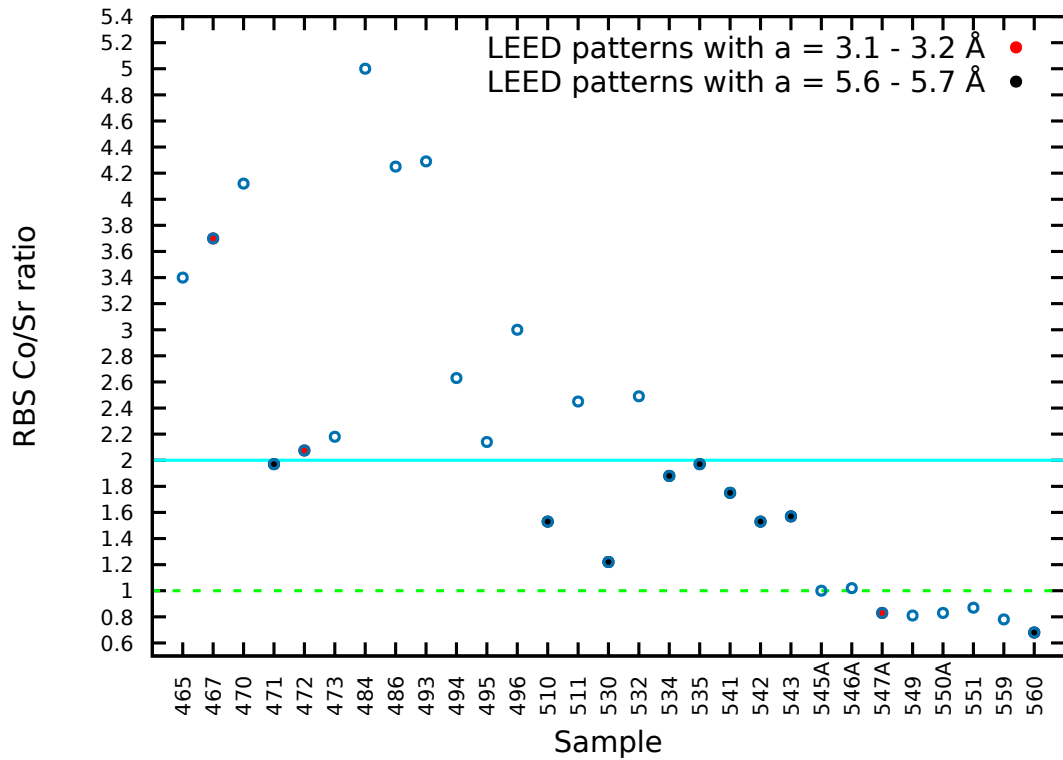
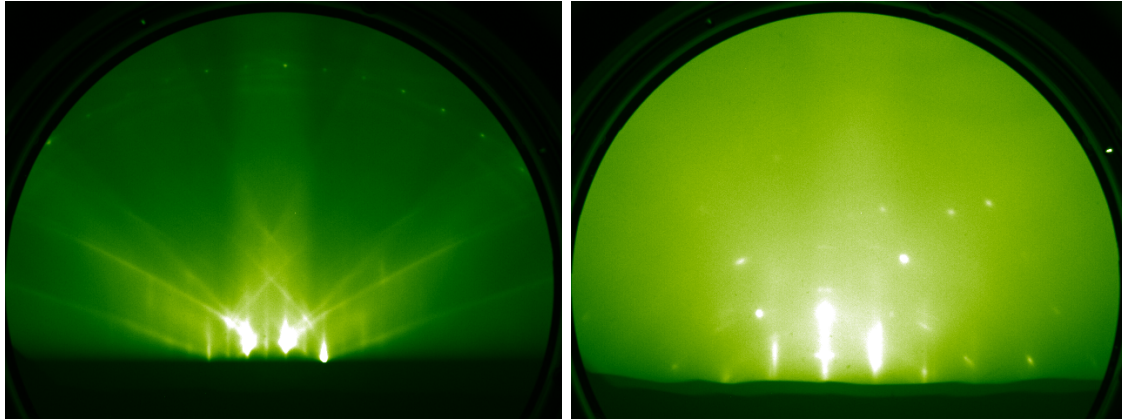


Figure 5.20: Overview of the Co/Sr ratio of samples prepared on a STO substrate indicating if a LEED pattern exists. Samples with a Co/Sr ratio higher than 2 show a LEED pattern only for samples 467 and 472, with calculated lattice parameters of 3.1 \AA . Below a Co/Sr ratio of 2, 9 of 16 samples show a LEED pattern with a calculated lattice parameter between 5.6 \AA and 5.7 \AA , which is consistent with a brownmillerite structure, while sample 574-A has nearly the same lattice parameter as 467 and 472, with 3.2 \AA .

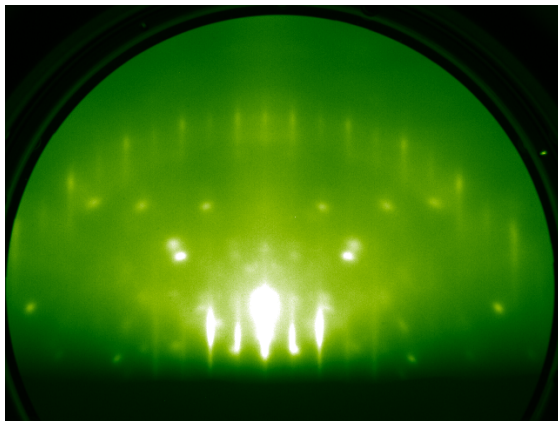
5.4.2 Reflection high-energy electron diffraction (RHEED)

RHEED was performed during and after sample growth to gather information about the crystalline quality of the films. The RHEED patterns shown here were taken at or below room temperature at an acceleration voltage of 15 keV.



a) SrTiO_3 substrate

b) 471 STO-SrCoO, Co/Sr: 1.97,
T = 750 °C, thickness = 215 Å



c) 510 STO-SrCoO, Co/Sr: 1.53,
T = 600 °C, thickness = 263 Å

Figure 5.21: RHEED patterns taken in-situ of annealed STO (a) and of samples 471 (b) and 510 (c). The samples were prepared at different deposition temperatures, 750 °C for sample 471 and 600 °C for sample 510, which leads to a RHEED pattern of much higher quality for sample 510.

Fig. 5.21a shows the RHEED pattern of an annealed STO substrate exhibiting very bright Bragg spots that are elongated into streaks at the bottom of the image, sharp spots on the first order Laue ring and Kikuchi lines going outwards from the bottom center. The RHEED pattern of sample 471, i.e. $\text{SrCo}_{1.97}\text{O}_x$, shows only weak indications of a Laue ring and very broad and not well defined streaks. The pattern also shows several brighter spots. Sample 510, with a stoichiometry of $\text{Co}/\text{Sr} = 1.53$, on the other hand is characterised by a clear Laue ring and well defined streaks, while still having similar spots as sample 471. Apart from the different stoichiometry, the growth temperature for sample 471 was higher, with 750 °C, than that of sample 510

with 600 °C. The lower growth temperature seems to be better for the crystallinity of the film, as all samples prepared at 600 °C show a similar or better RHEED pattern than sample 510, as long as they had a Co excess.

The MgO substrate, like the STO substrate, also shows elongated surface spots and very sharp Kikuchi lines, but the first order Laue ring is not visible because the sample was slightly tilted (fig. 5.22a). Samples prepared on MgO substrates do not form a crystalline structure because of the large mismatch of in-plane lattice constants for MgO and BM-SrCoO_x (7.2%) and therefore produce only a diffuse background (fig. 5.22d).

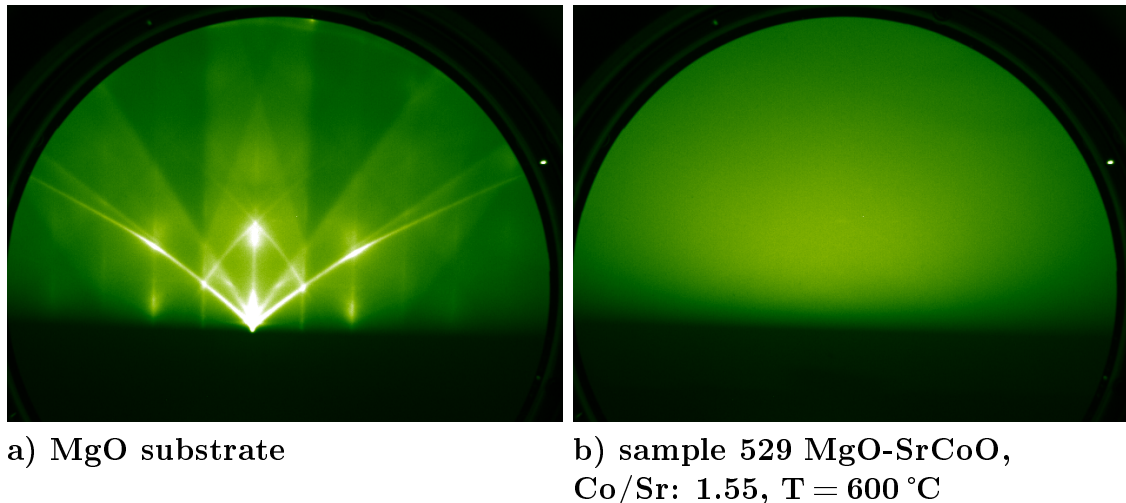
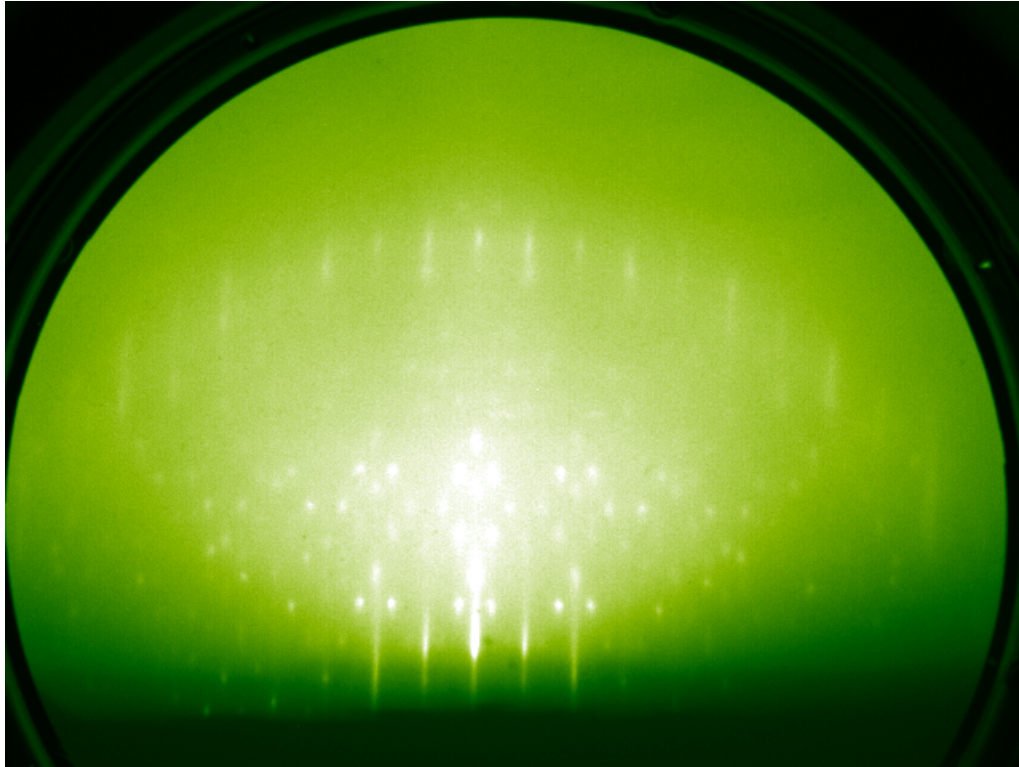
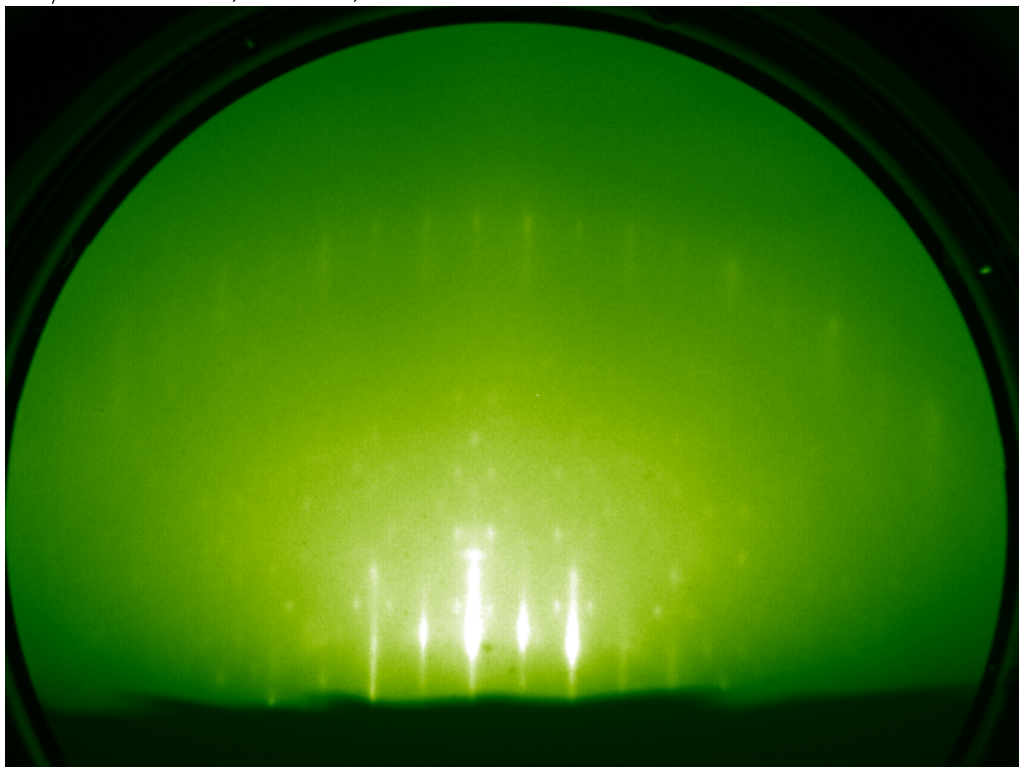


Figure 5.22: RHEED patterns of the MgO substrate (a) of sample 529 before deposition and of sample 529 MgO-SrCoO (b) after the deposition. They are slightly tilted. The Co/Sr ratio, growth temperature (T) are given.

For the stoichiometric samples 545-AB and 546-AB (fig.5.23a and b) the RHEED patterns from the two twin samples 'A' and 'B' cannot be separated since they were produced in a double sample holder. However, as the B samples on MgO contribute only to a diffuse background, the patterns of the A samples on STO can still be evaluated. The samples 545-A and 546-A exhibit elongated surface spots at the bottom of the images, as well as a first order Laue ring, though the spots are sharper than for sample 510 (fig. 5.21c). There are also many small sharp spots in between the Bragg spots and the Laue ring, the origin of which is still unclear and needs to be further investigated. Because of the sharpness of both the Bragg spots and the Laue rings, it can be concluded that the crystalline quality of the sample is quite good.

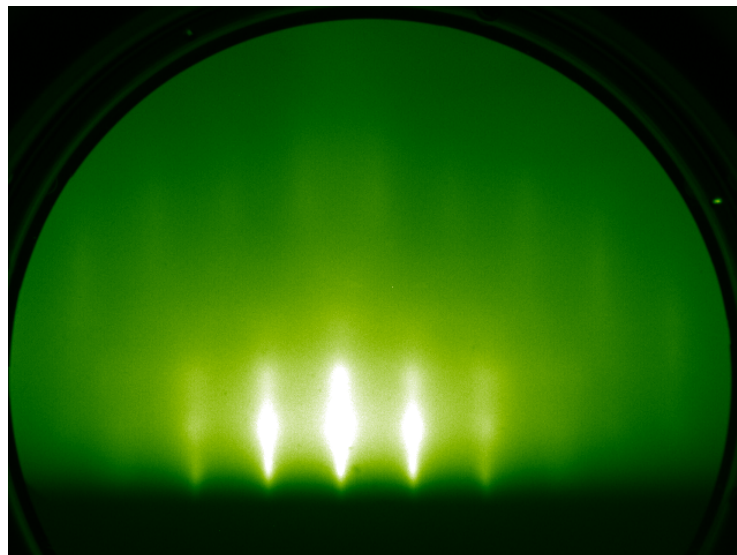


a) sample 545-AB STO/MgO-SrCoO,
Co/Sr: A:1.00, B:0.96, T = 600 °C



b) sample 546-AB STO/MgO-SrCoO,
Co/Sr: A:1.02, B:0.99, T = 600 °C

Figure 5.23: RHEED patterns of samples 545-AB (a) and 546-AB (b). The patterns originate only from the layer on STO ('A' samples), as the samples grown on MgO ('B' samples) only contribute to a diffuse background.



**sample 560 STO-SrCoO,
Co/Sr: 0.68, T = 600 °C**

Figure 5.24: RHEED pattern of sample 560.

For samples with a Sr excess, like sample 560 (fig. 5.24), the RHEED images reveal very diffuse spots and only show a very weak Laue ring, indicating poor crystallinity.

5.4.3 X-Ray diffraction (XRD)

In order to determine the crystalline structure of the films, X-ray Diffraction (XRD) measurements were performed with the PANanalytical Empyrean diffractometer of the Material Science Lab of the Helmholtz-Zentrum Geestacht (HZG) at MLZ in collaboration with Armin Kriele and with a Bruker D8 diffractometer at the Forschungszentrum Jülich by Dr. Paul Zakalek and Markus Waschke. The Empyrean employs a Mo-K_{α1} X-ray tube without monochromator, so K_{α1} and K_{α2} contributions are observed, while the D8 uses a Cu-K_{α1} tube with a monochromator (see Table 5.2 for X-ray wavelengths).

Table 5.2: X-ray Wavelengths

Device	Radiation	Wavelength [Å]
PANanalytical Empyrean	Mo-K _{α1}	0.70933
PANanalytical Empyrean	Mo-K _{α2}	0.71359
Bruker D8	Cu-K _{α1}	1.54056

To compare scans which were taken at different wavelengths, the scattering angle was converted into Q-values,

$$Q = \frac{4\pi}{\lambda} \sin(\theta), \quad (5.8)$$

with wavelength λ and incidence angle θ .

All measurements performed with the Empyrean reveal lines from a contamination of the tube. Therefore a scan of a pure STO substrate (black line) is given to unambiguously distinguish the peaks caused by the film (red line). The measurements with the Bruker D8 are given in blue. Table 5.3 gives the expected peak positions for STO, BM-SrCoO_x, and for the oxides of Co and Sr for the measured Q-range. The data was calculated with eq. 5.8, the lattice constants in table 2.1, and the Bragg equation for diffraction which is given in eq. 2.31.

Table 5.3: Theoretical Q values for STO, CoO, SrO, SrO₂, and BM-SrCoO_x peaks

	hkl	Q [Å ⁻¹]
STO	0 0 1	1.6094
STO	0 0 2	3.2212
CoO	0 0 2	2.9477
SrO	0 0 2	2.4346
SrO ₂	0 0 2	1.9185
SrO ₂	0 0 4	3.8371
	0 0 2	0.8036
	0 0 4	1.6071
BM-	0 0 6	2.4107
SrCoO _x	0 0 8	3.2142
	0 0 10	4.0178

The XRD measurements show peaks at Q values that match the Bragg condition. XRD allows the measurement of the interplanar spacing, i.e. the out-of-plane lattice constant, and the identification of the crystalline structure. Unlike the previously discussed electron scattering, X-rays have a large penetration depth and so XRD not only has contributions from the film surface, but from the whole film and the substrate. Fig. 5.25 shows the XRD spectrum for sample 546-A. The two peaks of high intensity, labelled STO (001) and STO (002), correspond to the first and second order Bragg reflections from the STO substrate. The other four peaks originate from the BM-SrCoO_x film. The BM-SrCoO_x (004) peak overlaps partially with the STO (001) peak and the BM-SrCoO_x (008) with the STO (002) peak. This is because the BM-SrCoO_x out-of-plane lattice constant is slightly larger than four times the out-of-plane lattice constant of the STO substrate ($c_{BM-SrCoO_x} = 15.745 \text{ \AA}$; $4 \cdot c_{STO} = 15.62 \text{ \AA}$). Thus the Q value of a given peak for the film is slightly less than one fourth of the Q value of the corresponding film of the substrate (see Table 5.3).

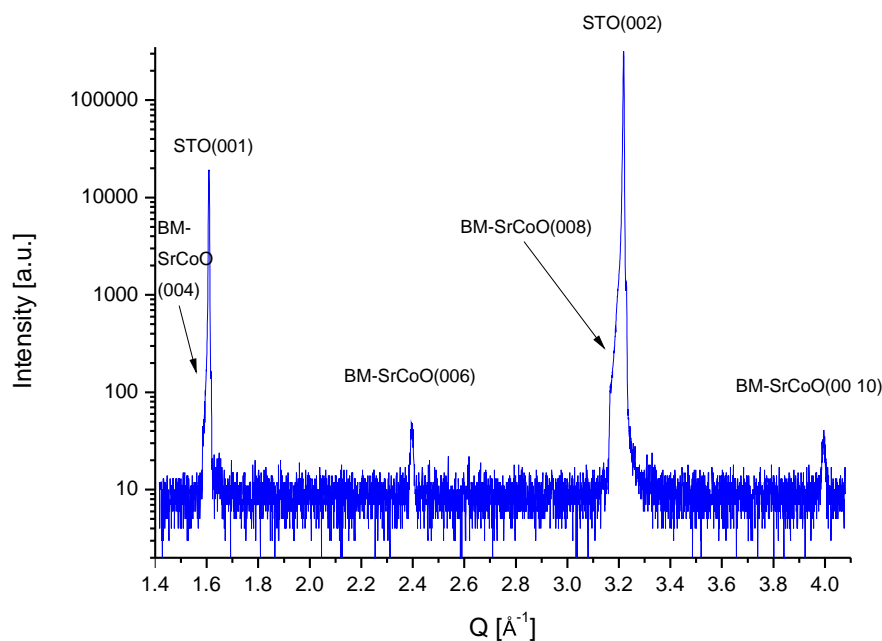
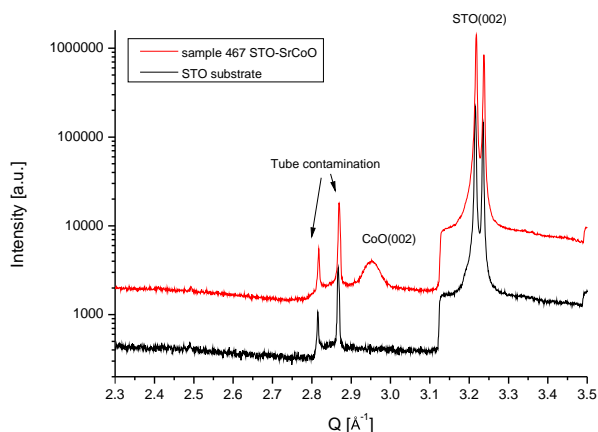


Figure 5.25: XRD measurement of sample 546-A. The Co/Sr ratio is 1.02.

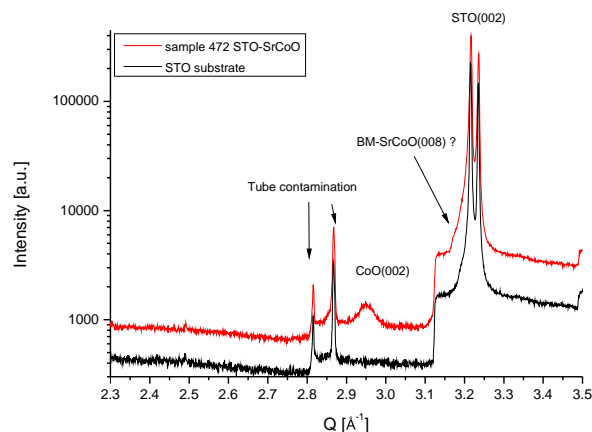
Fig. 5.26 shows a series of XRD measurements with decreasing Co excess. At a high Co/Sr ratio (3.7 for sample 467, fig. 5.26a), the only structural peak originating from the film is a CoO (002) peak. With decreasing Co/Sr ratio, the CoO peak decreases (samples 472-541, fig. 5.26b-d), while the BM-SrCoO_x (006) and (008) peaks become visible. For sample 543 (Co/Sr 1.57, fig. 5.27a), which was measured with the Bruker D8, there is still a CoO (002) peak, but the BM-SrCoO_x (004)-(00 10) peaks are prominent. For sample 510 (Co/Sr 1.53, fig. 5.27b) the CoO peak is even smaller. In sample 530 (Co/Sr 1.22, fig. 5.27c), the CoO peak is only very faintly visible, but the BM-SrCoO_x peaks are also quite weak, owing to a shorter measurement time. As the correct stoichiometry was reached for samples 545-A and 546-A (Co/Sr of 1 and 1.02, fig. 5.28a,b), the CoO peak has vanished and only the BM-SrCoO_x and substrate peaks remain. As the Co/Sr ratio drops below 1, i.e.

to 0.83 for samples 547-A and 550-A (fig. 5.28c,d), the BM-SrCoO_x peaks start to disappear and there is no visible BM-SrCoO_x peak in sample 547-A, while 550-A still has a BM-SrCoO_x (008) peak. There is, however, no indication for the formation of strontium-oxide in either SrO or SrO₂ stoichiometry yet, likely because the amount is too small, since a comparable Co excess in sample 530 also showed only a quite weak CoO peak.

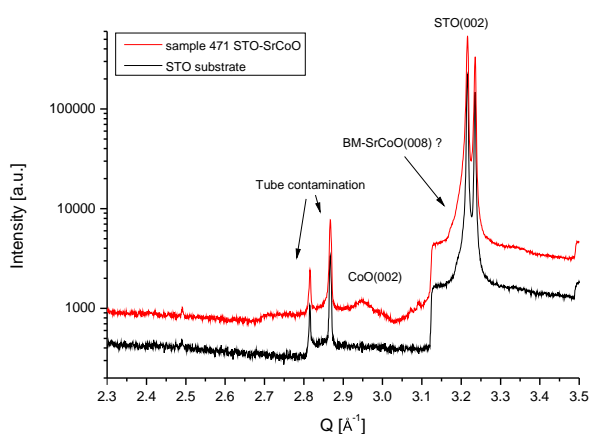
Taken together, for samples with a Co/Sr ratio between 2 and 1 the CoO peak decreases and the BM-SrCoO_x peak becomes more prominent, with a decreasing Co/Sr ratio. For stoichiometric samples the only visible peaks originating from the film are from the BM-SrCoO_x structure, confirming the growth of pure crystalline BM-SrCoO_x. For a Co/Sr ratio below 1, the BM-SrCoO_x structure vanishes.



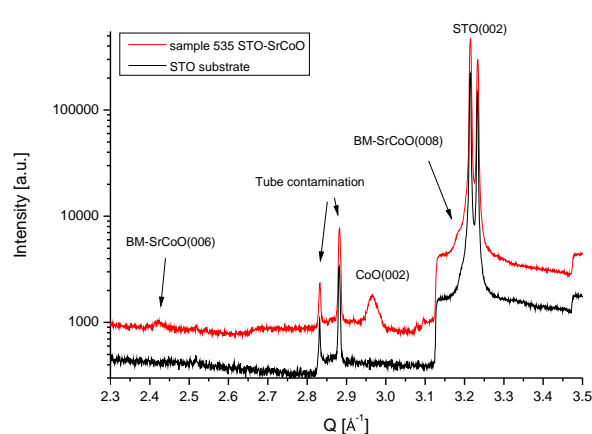
a) 467, Co/Sr: 3.70 (3 h)



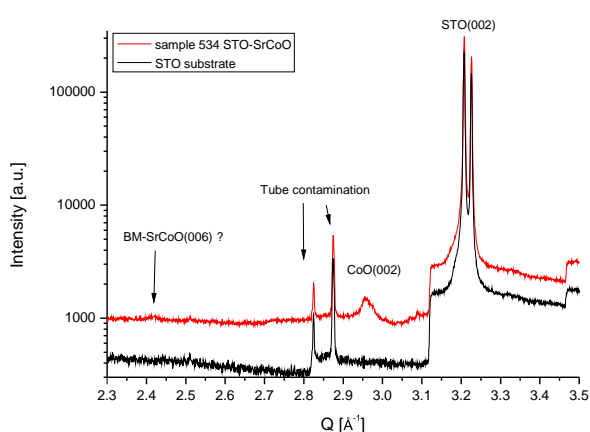
b) 472, Co/Sr: 2.08 (15.5 h)



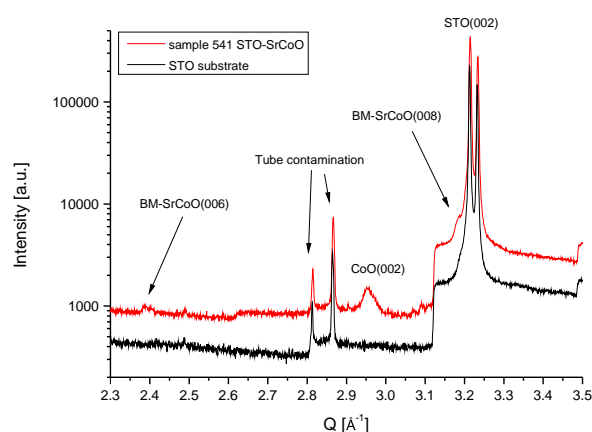
c) 471, Co/Sr: 1.97 (15.5 h)



d) 535, Co/Sr: 1.97 (15.5 h)



e) 534, Co/Sr: 1.88 (3 h)



f) 541, Co/Sr: 1.75 (15 h)

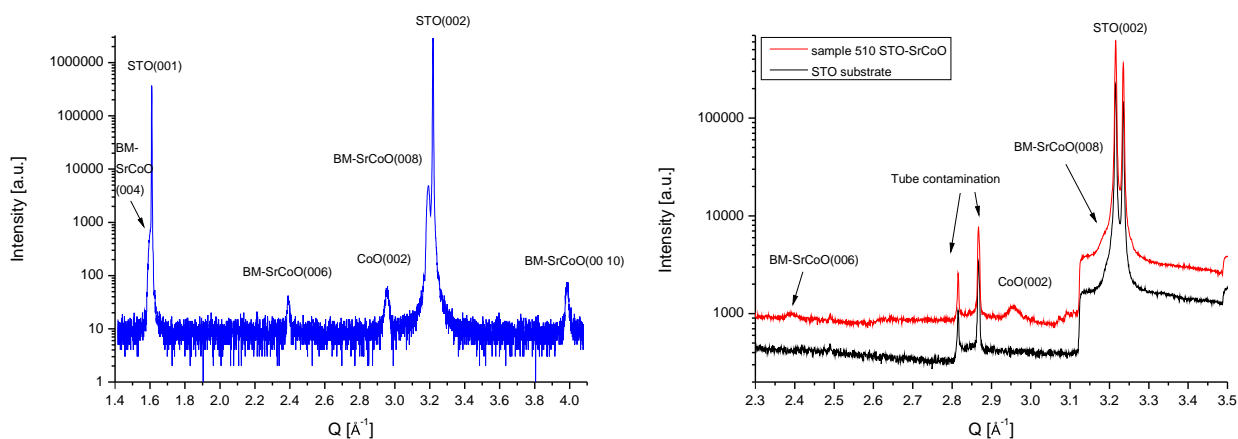
Figure 5.26: XRD measurements in decreasing order of Co/Sr ratio for samples. The measurement time is given in brackets.

a) 467, b) 472, and c) 471: Only the substrate peak and CoO peak are visible.

d) 535: The substrate peak, CoO peak, and small BM-SrCoO_x(006) and (008) peaks are visible.

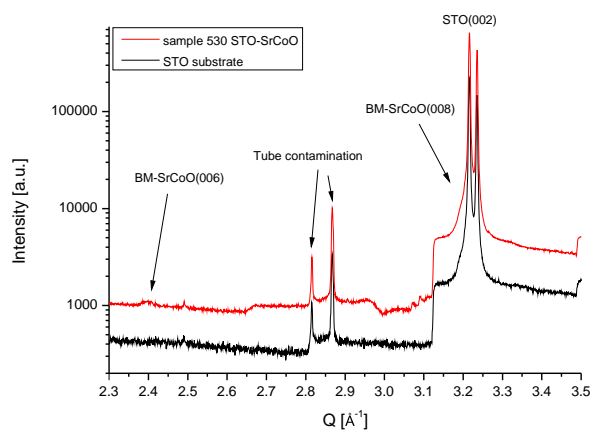
e) 534: The substrate peak, CoO peak, and an indication of the BM-SrCoO_x(006) are visible.

f) 541: The substrate peak, CoO peak, and BM-SrCoO_x(006) and (008) peaks are visible.



a) 543, Co/Sr: 1.57

b) 510, Co/Sr: 1.53 (3 h)



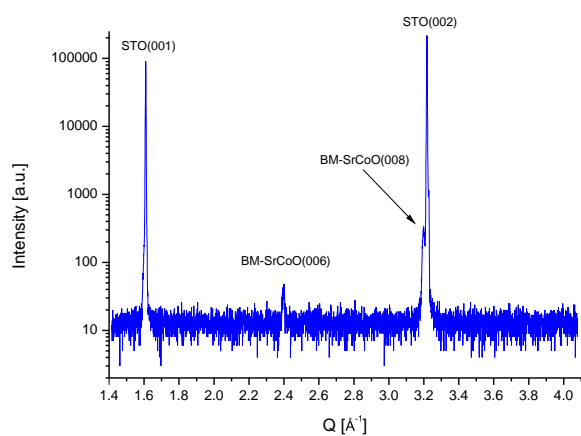
c) 530, Co/Sr: 1.22 (3 h)

Figure 5.27: XRD measurements in decreasing order of Co/Sr ratio for samples. The measurement time is given in brackets.

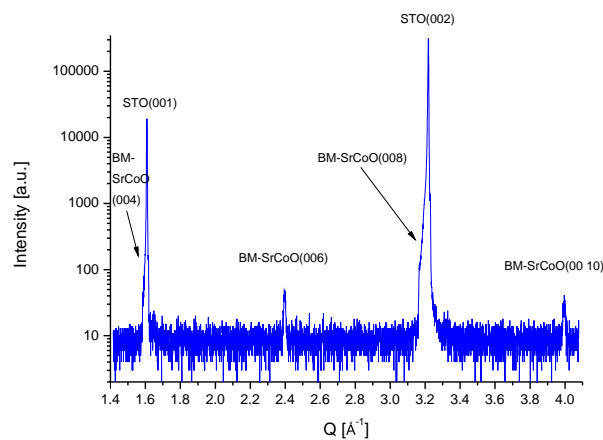
a) 543: The BM-SrCoO_x(004)-(00 10), CoO, and STO-substrate peaks are visible. The BM-SrCoO_x(004) peak is partially overlapping with the STO(001) peak. Measurement performed by Paul Zakalek.

b) 510: The substrate peak, CoO peak, and BM-SrCoO_x (006) and (008) peaks are visible.

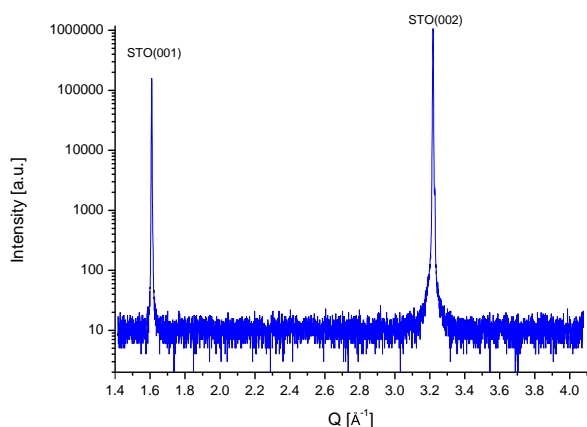
c) 530: The BM-SrCoO_x(006) and (008), STO-substrate peaks and a very small CoO peak are visible.



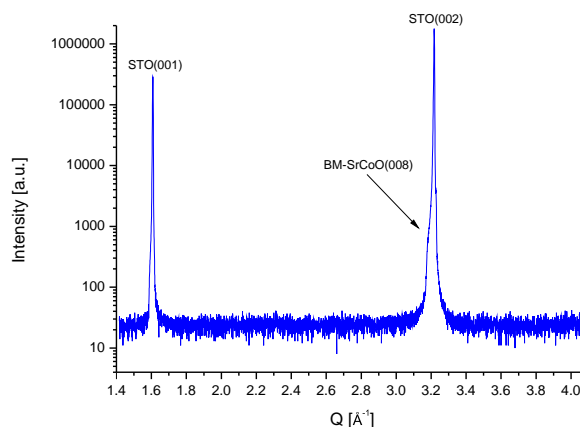
a) 545-A, Co/Sr: 1.00



b) 546-A, Co/Sr: 1.02



c) 547-A, Co/Sr: 0.83



d) 550-A, Co/Sr: 0.83

Figure 5.28: XRD measurements in decreasing order of Co/Sr ratio for samples.

a) 545-A: $\text{BM-SrCoO}_x(006)$ and (008) , as well as STO-substrate peaks are visible. There is no indication of a CoO peak. Measurement performed by Paul Zakalek.

b) 546-A: $\text{BM-SrCoO}_x(004)$ - (0010) , as well as STO-substrate peaks are visible. There is no indication of a CoO peak. The $\text{BM-SrCoO}_x(004)$ and (008) peak are partially overlapping with the STO(001) and (002) peaks. Measurement performed by Paul Zakalek. (this measurement is also shown in fig. 5.25)

c) 547-A: Only the STO-substrate peaks are visible. Measurement performed by Paul Zakalek.

d) 550-A: Only the $\text{BM-SrCoO}_x(008)$ and STO-substrate peaks are visible. The $\text{BM-SrCoO}_x(008)$ peak is partially overlapping with the STO(002) peak. Measurement performed by Paul Zakalek.

Chapter 6

Discussion

In the preceding chapters, $\text{Sr}_a\text{Co}_b\text{O}_x$ thin film samples, which were grown by molecular beam epitaxy, were investigated concerning stoichiometry, crystallinity, roughness, and topography. The aim was to find the growth conditions for stoichiometric samples i.e. $\text{Sr}_1\text{Co}_1\text{O}_x$ and to determine the influence of the growth conditions on the film properties.

Fig.6.1 gives an overview of the fabricated samples and their properties. The crystal structures of the samples were studied by LEED and XRD and the quality of the crystallinity based on the RHEED pattern in correlation to the stoichiometry and the deposition temperature are demonstrated. For a Co/Sr ratio above 2 (light brown region in fig.6.1) only CoO peaks were found in the XRD spectra. The brownmillerite structure started to emerge for Co/Sr ratios between 2 and 1 (yellow region), while CoO was still present. The stoichiometric samples (green region) revealed a pure BM- SrCoO_x structure. For samples with a Sr excess (light blue region) the crystalline structure vanished.

To find the correct frequency changes for stoichiometric samples i.e. the growth rates of the different materials, the Co frequency change was kept at one of four constant values, while the Sr frequency change was varied between the samples. For Sr frequency changes that were similar or lower than the Co frequency change, the samples had an excess of Co. Samples with the correct stoichiometry require a Co/Sr frequency change ratio between 0.33 and 0.37. For lower ratios the samples revealed a Sr excess.

In case of Co excess the samples have a tendency to form islands with a height difference between the islands and holes, which is in the range of the total layer thickness for Co/Sr ratios above 2, and still about half the thickness for Co/Sr ratios below 2. It is reasonable to assume that during the deposition individual islands grow independently of each other, only forming a complete layer when they become big enough to coalesce.

For a Co/Sr ratio below 2, the films start to form terraces in addition to the islands. The emergence of the terraces in the AFM topography also corresponds to the observation of clearly defined peaks and first order Laue rings in the RHEED images and the formation of BM- SrCoO_x peaks in the XRD spectra, starting with

the sample 510 (Co/Sr = 1.53). The difference to samples 465-508 is the change in deposition temperature from 750 °C to 600 °C, and, apart from samples 511 and 532, a Co/Sr ratio below 2.

With decreasing Co/Sr ratio, the XRD peaks for the BM-SrCoO_x structure become stronger, while the CoO peaks shrink until they vanish for the samples with Co/Sr ≈ 1. For the stoichiometric samples 545-A and 546-A, only BM-SrCoO_x peaks exist. The samples exhibit very clear RHEED patterns with sharp streaks and first order Laue rings.

As soon as the samples become Co deficient, the BM-SrCoO_x structure does not exist anymore. The XRD measurements show only very weak indications of structural film peaks, the RHEED patterns become very diffuse, and the AFM topography measurements don't show a terrace structure.

To summarize, the growth conditions for the preparation of Sr₁Co₁O_x thin film samples by molecular beam epitaxy were investigated and the preparation of stoichiometric Sr₁Co₁O_x with brownmillerite crystal structure was successful.

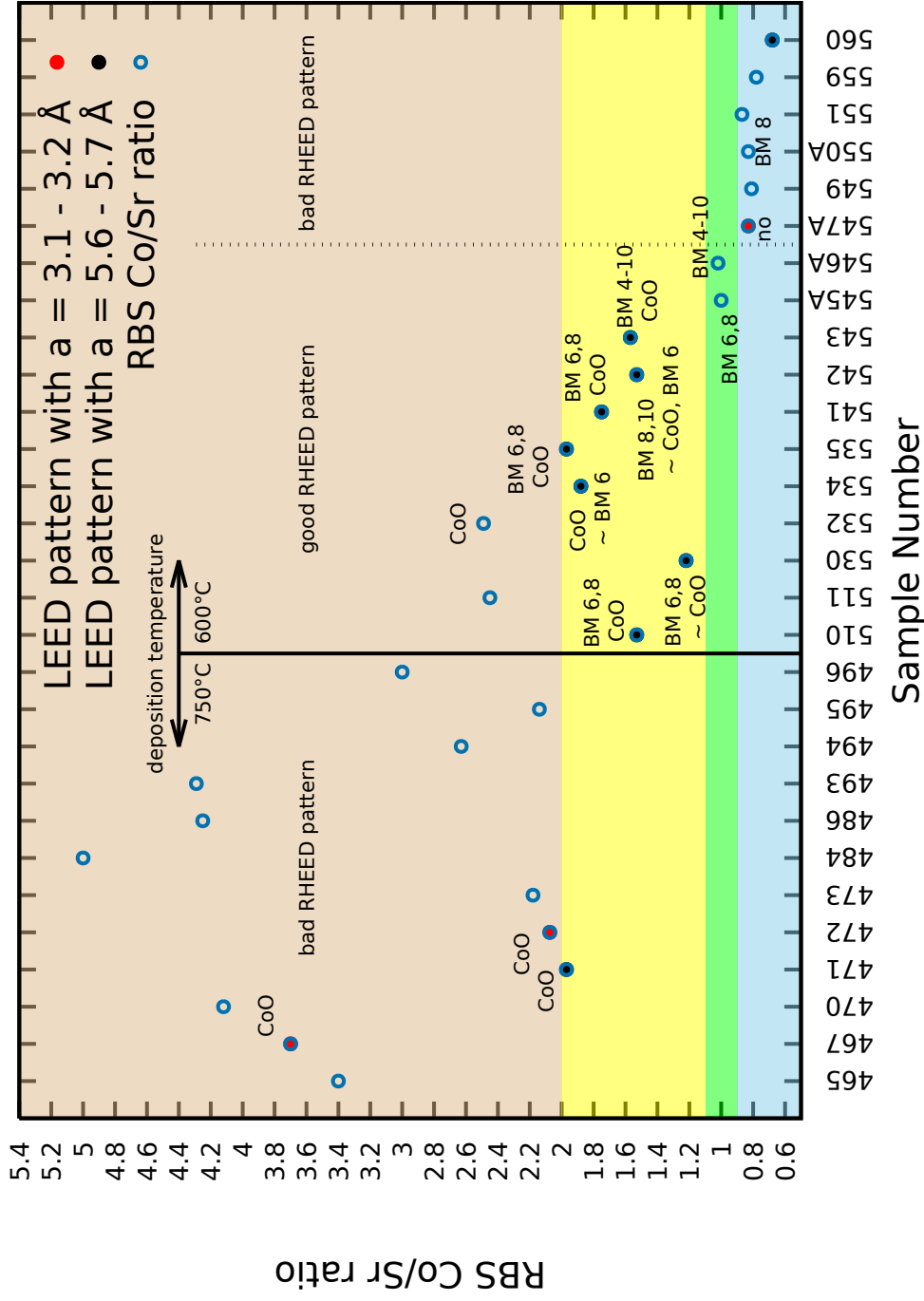


Figure 6.1: Overview of the Co/Sr ratio of samples prepared on a STO substrate with visible LEED patterns (red and black filled circles) and corresponding XRD film peaks. Samples with a label 'CoO' reveal a visible CoO (002) peak, while 'BM a' indicates the existence of a BM-SrCoO_x (00a) peak. A very weak peak is identified by a '~' symbol. Sample 547-A does not exhibit a visible film peak. The deposition temperature is indicated. Samples from 510 to 546-A have good RHEED patterns.

The different coloured regions correspond to the XRD peaks found in that region:

light brown: only CoO; yellow: CoO and BM-SrCoO_x; green: only BM-SrCoO_x; blue: only weak indications of BM-SrCoO_x.

Chapter 7

Outlook

After the successful growth of $\text{Sr}_1\text{Co}_1\text{O}_x$ in brownmillerite structure, there are still some open questions and fields of investigation.

In order to grow thin film heterostructures, which are often required for applications, such as resistive switching memories [30], tunnel junctions based on ferroelectric/multiferroic structures [31], or even multiferroic/superconducting interfaces [32] the samples have to have a roughness in the low Å range. The samples prepared in this thesis are still quite rough with about 25 Å for the stoichiometric samples, so the growth conditions, in particular the deposition temperature and cooling rate, still need to be studied to obtain smooth films. Also, the absence of a LEED pattern for the stoichiometric samples, while a clear RHEED pattern is observable, remains puzzling, especially since the LEED patterns for samples with a slight Co excess and even two samples with a Sr excess are clearly visible.

Since one of the defining characteristics of strontium cobaltite is the ability to switch topotactically between the brownmillerite and perovskite structure, investigating the conditions under which the perovskite structure can be grown would be a next step. These conditions are well known for PLD [4], but have to be adapted for MBE growth. Along the same lines, annealing the brownmillerite samples in an oxygen atmosphere for different time intervals and at different temperatures would be another goal to induce the perovskite structure and to determine the conditions for the structural change.

As the oxygen content of SrCoO_x , and thus the magnetic properties, can be influenced by lattice strain, it would be very interesting to grow a SrCoO_x film on a ferroelectric or piezoelectric substrate, forming an artificial multiferroic material. This would potentially allow the control of the magnetic properties of the film by applying a voltage to the substrate, i.e. switching between a ferromagnetic and an antiferromagnetic state may become feasible. As this would require the use of another substrate than STO which was used in this thesis, the deposition conditions would have to be adjusted, because of a difference in sticking coefficient and strain for different substrates.

As these proposed fields of investigation are based on the magnetic properties of the samples it would be extremely interesting to study them with neutron scat-

tering, particularly for samples with a strained film. This would allow for the depth resolved investigation of the influence of strain on the magnetic properties, potentially revealing a magnetic gradient. Or if the whole film changes its properties, in case of a sample which was grown on a piezoelectric substrate, the switching between the two states could be investigated.

Chapter 8

Summary

In this work the preparation conditions for the growth of stoichiometric $\text{Sr}_1\text{Co}_1\text{O}_x$ by oxide molecular beam epitaxy were determined by growing and analysing samples prepared at different deposition rates, temperatures and cooling rates.

Various sample series at four constant Co frequency changes, i.e. the growth rate, with varying Sr frequency changes were grown and the correct frequency change ratio for stoichiometric samples was determined. The correlation between stoichiometry and Co/Sr frequency change ratios revealed, that for the desired stoichiometry the Sr frequency change has to be about three times as high as the Co frequency change. The stoichiometry was determined by Rutherford backscattering spectroscopy.

The samples were analysed regarding their crystallinity by low energy electron diffraction, reflection high energy electron diffraction, and X-ray diffraction. A CoO crystal structure was revealed for samples with a Co/Sr ratio higher than 2. For a Co/Sr ratio between 2 and 1, both CoO and BM-SrCoO_x structures coexist. The stoichiometric $\text{Sr}_1\text{Co}_1\text{O}_x$ samples revealed only a BM-SrCoO_x structure. Samples with a small Sr excess showed only weak signs of crystallinity.

The surface topography measurements by atomic force microscopy revealed a terrace structure for samples that are stoichiometric or have a moderate Co excess. The sample roughness of the stoichiometric samples is about 25 Å and needs further improvement, possibly by additional adjustments to the growth temperature.

In conclusion, the growth conditions for stoichiometric $\text{Sr}_1\text{Co}_1\text{O}_x$ samples with brownmillerite crystal structure were successfully determined.

Acknowledgements

I would like to thank a number of people, without which this work would not have been possible:

Dr. habil. Joachim Wuttke for the supervision of this thesis and for giving me the opportunity to work at the JCNS and MLZ.

Prof. Dr. Florian Klappenberger for the second revision of this thesis and his lecture on scanning probe microscopy.

Sabine Pütter for the outstanding support throughout this thesis. I especially want to thank you for the trust and patience, as well as the scientific advice and discussions about thin film growth, sample characterisation and analysis, and science in general that were essential for this thesis.

Prof. Dr. Thomas Brückel for the possibility to work in this institute and for letting me participate in the JCNS neutron scattering labcourse.

Jürgen Schubert, Willi Zander (PGI-9, Forschungszentrum Jülich) and René Heller (IBC, Helmholtz-Zentrum Dresden-Rossendorf) for the RBS measurements and data fitting and Jürgen Schubert for the discussions about RBS.

Peter Link and Senay Öztürk (Neutron optics, Heinz Maier-Leibnitz Zentrum) for allowing me to use their X-ray reflectometer.

Amin Kriele (Helmholtz-Zentrum Geestacht, Heinz Maier-Leibnitz Zentrum) for giving me the possibility to do XRD measurements.

Paul Zakalek and Marks Waschk (JCNS, Forschungszentrum Jülich) for the XRD measurements and the discussions about the MBE and thin film growth.

Amir Syed Mohd for the discussions about the MBE and scattering techniques, and for letting me accompany you to your beamtime at MARIA and allowing me to experience a neutron scattering experiment, as well as being a great colleague.

Emmanuel Kentzinger and Sonja Schröder (JCNS, Forschungszentrum Jülich) for the discussions about thin films and for letting me participate in the beamtime at TREFF and KWS-3.

Alfred Richter, Bernhard Großmann, Marco Gödel, Harald Kusche, Vladimir Ossovyi, and Simon Starringer for their technical support.

Franziska Michel for the administrative support.

Alexandra Steffen, Xiao Wang, Rui Wang, Stefan Holler, Manuchar Gvaramia, Viviane Pecanha Antonio, Erxi Feng, Eva Steinberger, and all my colleagues of the JCNS for the great time working here.

And my family for the unwavering support and love.

Bibliography

- [1] M. K. Wu, J. R. Ashburn, C. J. Torng, P. H. Hor, R. L. Meng, L. Gao, Z. J. Huang, Y. Q. Wang, and C. W. Chu, "Superconductivity at 93 K in a new mixed-phase Y-Ba-Cu-O compound system at ambient pressure," *Phys. Rev. Lett.*, vol. 58, pp. 908–910, Mar 1987.
- [2] C. Lu, W. Hu, Y. Tian, and T. Wu, "Multiferroic oxide thin films and heterostructures," *Applied Physics Reviews*, vol. 2, no. 2, p. 021304, 2015.
- [3] H. Jeen, W. S. Choi, J. W. Freeland, H. Ohta, C. U. Jung, and H. N. Lee, "Topotactic phase transformation of the brownmillerite $\text{SrCoO}_{2.5}$ to the perovskite $\text{SrCoO}_{3-\delta}$," *Advanced Materials*, vol. 25, pp. 3651–3656, 2013.
- [4] H. Jeen, W. S. Choi, M. D. Biegalski, C. M. Folkman, I.-C. Tung, D. D. Fong, J. Freeland, D. Shin, H. Ohta, M. F. Chisholm, and H. N. Lee, "Reversible redox reactions in an epitaxially stabilized SrCoO_x oxygen sponge," *nature materials*, vol. 12, November 2013.
- [5] A. Nemudry, P. Rudolf, and R. Schöllhorn, "Topotactic electrochemical redox reactions of the defect perovskite $\text{SrCoO}_{2.5+x}$," *Chem. Mater.*, vol. 8, pp. 2232–2238, Jan. 1996.
- [6] S. Hu, Y. Wang, C. Cazorla, and J. Seidel, "Strain-enhanced oxygen dynamics and redox reversibility in topotactic $\text{SrCoO}_{3-\delta}$," *Chem. Mater.*, vol. 29, pp. 708–717, Jan. 2017.
- [7] J. H. Lee and K. M. Rabe, "Coupled magnetic-ferroelectric metal-insulator transition in epitaxially strained SrCoO_3 from first principles," *Phys. Rev. Lett.*, vol. 107, p. 067601, Aug 2011.
- [8] S. J. Callori, S. Hu, J. Bertinshaw, Z. J. Yue, S. Danilkin, X. L. Wang, V. Nagarajan, F. Klose, J. Seidel, and C. Ulrich, "Strain-induced magnetic phase transition in $\text{SrCoO}_{3-\delta}$ thin films," *Physical Review B*, vol. 91, April 2015.
- [9] P. Bezdicka, A. Wattiaux, J. C. Grenier, M. Pouchard, and P. Hagenmuller, "Preparation and characterization of fully stoichiometric SrCoO_3 by electrochemical oxidation," *Zeitschrift für anorganische und allgemeine Chemie*, vol. 619, no. 1, pp. 7–12, 1993.
- [10] Y. Long, Y. Kaneko, S. Ishiwata, Y. Taguchi, and Y. Tokura, "Synthesis of

- cubic SrCoO₃ single crystal and its anisotropic magnetic and transport properties,” *Journal of Physics: Condensed Matter*, vol. 23, no. 24, 2011.
- [11] H. Watanabe, “Magnetic properties of perovskites containing strontium,” *J. Phys. Soc. Jpn.*, vol. 12, pp. 515–522, May 1957.
- [12] A. Munoz, C. de la Calle, J. A. Alonso, P. M. Botta, V. Pardo, D. Baldomir, and J. Rivas, “Crystallographic and magnetic structure of SrCoO brownmillerite: Neutron study coupled with band-structure calculations,” *Phys. Rev. B*, vol. 78, Aug. 2008.
- [13] T. Takeda, Y. Yamaguchi, and H. Watanabe, “Magnetic structure of SrCoO_{2.5},” *Journal of the Physical Society of Japan*, vol. 33, no. 4, pp. 970–972, 1972.
- [14] W. S. Choi, H. Jeon, J. H. Lee, S. S. A. Seo, V. R. Cooper, K. M. Rabe, and H. N. Lee, “Reversal of the lattice structure in SrCoO_x epitaxial thin films studied by real-time optical spectroscopy and first-principles calculations,” *Phys. Rev. Lett.*, vol. 111, Aug. 2013.
- [15] J. R. Petrie, C. Mitra, H. Jeon, W. S. Choi, T. L. Meyer, F. A. Reboredo, J. W. Freeland, G. Eres, and H. N. Lee, “Strain control of oxygen vacancies in epitaxial strontium cobaltite films,” *Advanced Functional Materials*, vol. 26, no. 10, pp. 1564–1570, 2016.
- [16] K. Momma and F. Izumi, “Vesta 3 for three-dimensional visualization of crystal, volumetric and morphology data,” *Journal of Applied Crystallography*, vol. 44, no. 6, pp. 1272–1276, 2011.
- [17] T. Brückel, D. Richter, G. Roth, A. Wischnewski, and R. Zorn, *Laboratory Course Neutron Scattering*. Forschungszentrum Jülich GmbH, 2015.
- [18] M. Angst, T. Brückel, D. Richter, and R. Zorn, eds., *Scattering Methods for Condensed Matter Research: Towards Novel Application at Future Sources*. Forschungszentrum Jülich GmbH, 2012.
- [19] T. Brückel, *Laboratory Course Neutron Scattering: A neutron primer: Elastic scattering and properties of the neutron*, ch. 2. Forschungszentrum Jülich GmbH, 2015.
- [20] E. Kentzinger, *Laboratory Course Neutron Scattering: Neutron Reflectometry*, ch. 9. Forschungszentrum Jülich GmbH, 2015.
- [21] G. Roth, *Laboratory Course Neutron Scattering: Diffraction*, ch. 4. Forschungszentrum Jülich GmbH, 2015.
- [22] L. Névoit and P. Croce, “Caractérisation des surfaces par réflexion rasante de rayons x. application à l’étude du polissage de quelques verres silicates,” *Rev. Phys. Appl. (Paris)*, 1980.

- [23] W.-K. Chu, J. W. Mayer, and M.-A. Nicolet, *Backscattering Spectrometry*. Academic Press, 1978.
- [24] J. Reichow, “DCA MBE M600 technical system description,” 2010.
- [25] F. J. Giessibl, “Advances in atomic force microscopy,” *Rev. Mod. Phys.*, vol. 75, pp. 949–983, Jul 2003.
- [26] D. Nečas and P. Klapetek, “Gwyddion: an open-source software for SPM data analysis,” *Central European Journal of Physics*, vol. 10, pp. 181–188, 2012.
- [27] G. Sauerbrey, “Verwendung von Schwingquarzen zur Wägung dünner Schichten und zur Mikrowägung,” *Zeitschrift für Physik*, vol. 155, pp. 206–222, 1959.
- [28] L. Doolittle, M. Thompson, and R. Cochran, “<http://www.genplot.com/doc/rump.htm>.”
- [29] A. Glavic, “<https://sourceforge.net/projects/plotpy>.”
- [30] C. Wang, K.-J. Jin, Z.-T. Xu, L. Wang, C. Ge, H.-B. Lu, H.-Z. Guo, M. He, and G.-Z. Yang, “Switchable diode effect and ferroelectric resistive switching in epitaxial BiFeO₃ thin films,” *Applied Physics Letters*, vol. 98, no. 19, p. 192901, 2011.
- [31] E. Y. Tsymbal and H. Kohlstedt, “Tunneling across a ferroelectric,” *Science*, vol. 313, no. 5784, pp. 181–183, 2006.
- [32] C. H. Ahn, J.-M. Triscone, and J. Mannhart, “Electric field effect in correlated oxide systems,” *Nature*, vol. 424, pp. 1015–1018, Aug. 2003.

List of Figures

2.1	Perovskite and brownmillerite structure	8
2.2	BM-SrCoO on STO	9
2.3	Rocksalt structure of MgO, CoO, and SrO	9
2.4	Scattering geometry for the differential cross section. Taken from [19].	11
2.5	Phase difference between two waves, scattered at different point inside a sample. Taken from [19].	13
2.6	Transmission and specular reflection from a film and a substrate. Taken from [20].	14
2.7	Ewald construction for the scattering condition in reciprocal space . .	16
3.1	Schematic of the DCA M600 molecular beam epitaxy setup. Modified from [24].	19
3.2	Lennard-Jones potential.	21
3.3	LEED geometry with Ewald sphere.	23
3.4	Ewald construction for RHEED geometry.	24
4.1	Auger electron spectrum after substrate treatment	27
4.2	QCM frequency change setting	28
4.3	Overview of the applied Sr and Co frequency changes for all samples .	29
5.1	Auger electron spectrum of sample 473 after deposition	35
5.2	RBS simulation	37
5.3	RBS measurements for stoichiometric samples 545-A, -B, and 546-A, -B	38
5.4	Relation of the Co/Sr frequency ratio set by the quartz crystal microbalance and the Co/Sr stoichiometry measured by Rutherford backscattering spectroscopy. An enlarged part can be found in fig. 5.5.	39
5.5	Relation of the Co/Sr ratio of the quartz crystal microbalance and measured by Rutherford Backscattering Spectroscopy for samples near the correct stoichiometry	39
5.6	XRR measurements for samples 473, 484, 545-A, and 546-A	41
5.7	AFM topography for samples 465, 467, 486, and 493, with height profiles for 465 and 467	43
5.8	AFM topography for samples 472, and 473	44
5.9	AFM topography for samples 470, 471, 484, and 485	45
5.10	AFM topography for samples 494, 495, and 496	46
5.11	AFM topography for samples 530, 534, 542, and 543	47
5.12	AFM topography for samples 541 and 535 with height profiles	49
5.13	AFM topography for sample 546-A with height profiles	50

5.14	Crystal structure of BM-SrCoO _x with terraces of half a unit cell in height as a possible origin of the terraces observed for samples 530 - 546-A	51
5.15	AFM topography for samples 549, 550-A, 559, and 560	52
5.16	Comparison of the roughness measured by AFM and XRR	54
5.17	LEED images of an STO substrate and samples 471, 510, and 530	57
5.18	LEED images of samples 534, 535, 541, 542, 543, and 560	58
5.19	LEED images of samples 467, 472, and 547-A	59
5.20	Overview of the Co/Sr ratio of samples prepared on a STO substrate with visible LEED patterns	60
5.21	RHEED patterns of an STO substrate and samples 471 and 510	61
5.22	RHEED patterns of an MgO substrate and sample 529	62
5.23	RHEED patterns of samples 545-AB and 546-AB	63
5.24	RHEED pattern of sample 560	64
5.25	XRD measurement of sample 546-A	66
5.26	XRD measurement of samples 467, 472, 471, 535, 534, and 541	68
5.27	XRD measurement of samples 543, 510, 542, and 530	69
5.28	XRD measurement of samples 545-A, 546-A, 547-A, and 550-A	70
6.1	Overview of the Co/Sr ratio of samples prepared on a STO substrate with visible LEED patterns and corresponding XRD film peaks	73

List of Tables

2.1	Structures and lattice constants of materials appearing in this thesis .	10
4.1	Overview of sample preparation parameter	32
4.2	Overview of RBS, XRR, and AFM measurements	33
5.1	Lattice constants calculated from LEED images	56
5.2	X-ray Wavelengths	65
5.3	Theoretical Q values for STO, CoO, SrO, SrO ₂ , and BM-SrCoO _x peaks	65

List of Publications

1. Presentation and poster at the internal JCNS student day, "Preparation and characterisation of thin SrCoO_x films", Jülich, November 2016
2. Poster at the workshop on science of the program 'From Matter to Materials and Life' within the Helmholtz research field 'Matter', "Requirements for stoichiometric $\text{SrCoO}_{3-\delta}$ thin films", Hamburg, December 2016
3. Poster at the 2017 Deutsche Physikalische Gesellschaft spring meeting of the condensed matter section, "Relation of sample stoichiometry and growth conditions in $\text{SrCoO}_{3-\delta}$ thin films", Dresden, March 2017